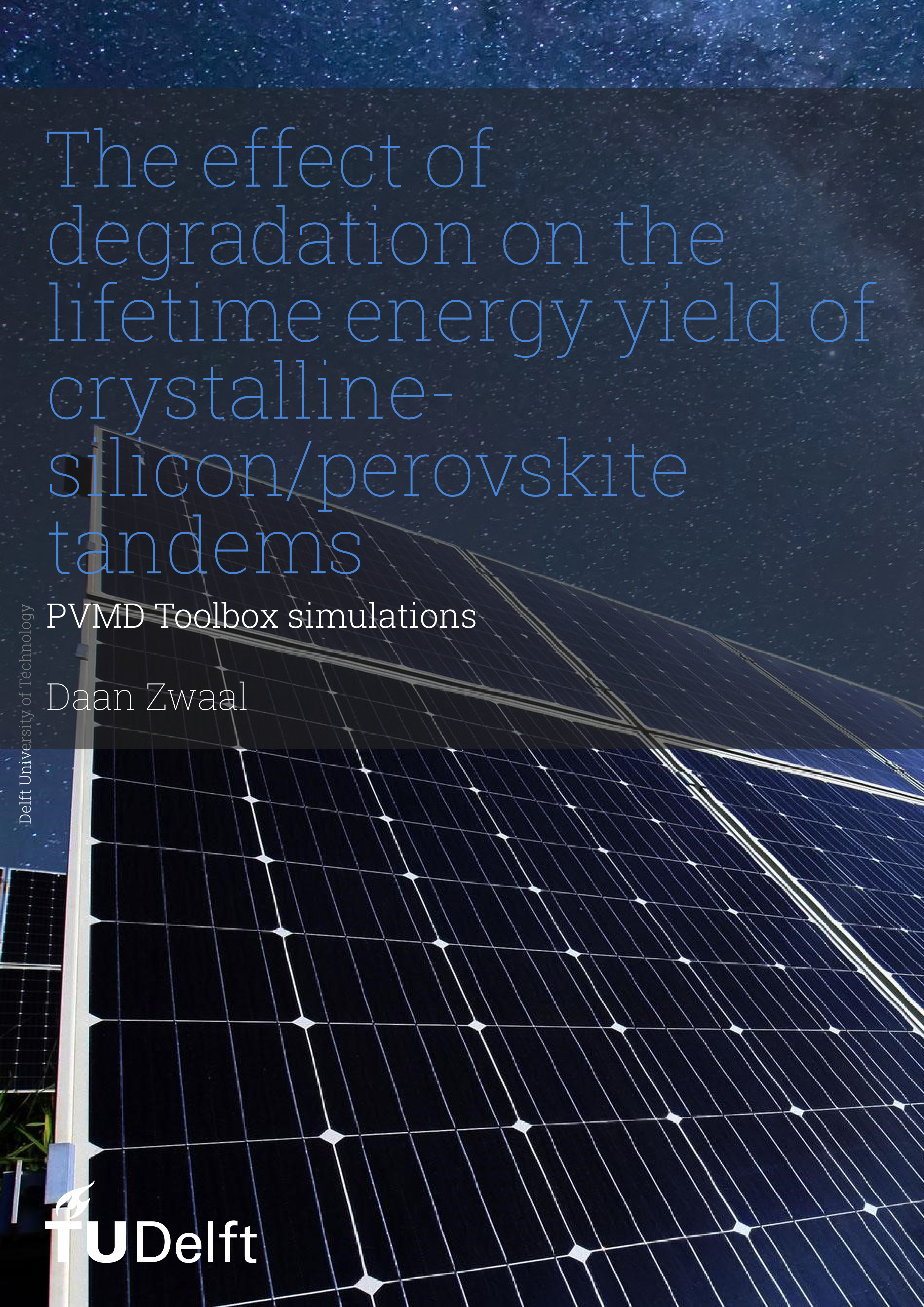

The effect of degradation on the lifetime energy yield of crystalline-silicon/perovskite tandems

PVMD Toolbox simulations

Daan Zwaal

Delft University of Technology

The effect of degradation on the lifetime energy yield of crystalline-silicon/perovskite tandems

PVMD Toolbox simulations

by

Daan Zwaal

to obtain the degree of Master of Science
at the Delft University of Technology,

Project duration:	November 2023 – July 2024	
Thesis committee:	Dr.ir. R. Santbergen,	TU Delft (PVMD), Supervisor
	Prof.dr.ir. A.H.M. Smets	TU Delft (PVMD)
	Dr.ir. D. van der Born	TU Delft (High Voltage)
	Ir. Y. Blom	TU Delft (PVMD), Daily supervisor

TU Delft

Preface

This thesis report is written for the last part of my Master of Science in Sustainable Energy Technology at the Delft University of Technology. For the last nine months I have worked in the Photovoltaic Material and Devices (PVMD) group and I have made a model to estimate the degradation rate of perovskite in crystalline-silicon/perovskite tandem modules. During these nine months I got time to enhance my knowledge about photovoltaic technology, which finally resulted in this project.

First I would like to thank and show my gratitude to Youri Blom for being my daily thesis supervisor and helping me during this project. He helped me doing this thesis step by step and was always available for help. He provided me with feedback and his knowledge helped me improving my research every week. Next, I would also like to thank Dr.ir. Rudi Santbergen for his guidance, insights and feedback during this project as my supervisor. I want to thank Prof.dr.ir. Arno Smets and Dr.ir Dennis van der Born for joining the thesis committee. Finally, I want to thank my friends and family who supported me in these two years of my Master's degree, they helped my through this last part of my education at the Delft University of Technology.

Daan Zwaal
Delft, July 2024

Summary

Throughout the development of crystalline-silicon/perovskite tandem solar cells, the degradation rate of the perovskite top cells has become a limiting parameter. Currently, perovskite faces stability issues, mainly caused by corrosion and the light-soaking effect. This work investigates the degradation rate of the perovskite top cell, where a model is created to determine the parameters from the single diode model that change the IV-curve of a solar cell and lifetime energy yield simulations were performed to find the maximum tolerable degradation rate of perovskite in a tandem module to obtain a higher energy yield compared to a single-junction module

Using experimental data from the King Abdullah University of Science and Technology (KAUST), where the external parameters from the measurements were provided, the changes over time in the ideality factor, saturation current, shunt resistance, and series resistance were estimated, using a numerical model. Linear trend lines through the fitting parameters over time were used and lifetime energy yield simulations were performed. For these simulations, a crystalline-silicon/perovskite tandem cell with an efficiency of 31.1% was compared to to a single-junction cell with an efficiency of 23.9%, where the single-junction cell's optics are the same as the tandem cell's bottom cell. To perform lifetime energy yield simulations, the PVMD toolbox is used.

Simulating the lifetime energy yield over 10 years, a perovskite degradation rate of 27.5%/year was found using the electrical parameters under STC, where the power output decreased from 4.95W to 0.24W per cell. Comparing 2T and 4T configurations, where the cell optics were kept the same, degradation rates of 21.2%/year and 9.5%/year were found for 2T and 4T, respectively. Looking at different geographical locations, degradation rates of 19%, 20%, 20.6% and 21.2% per year were found for Delft, Lagos, Lisbon and Shanghai, respectively. These differences were caused by current mismatch between the top and bottom cell, where the highest mismatch of 0.55 mA/cm^2 was found in Shanghai.

To determine the maximum tolerable degradation rate of the perovskite top cell resulting in a higher lifetime energy yield for a tandem module compared to a single-junction module over 25 years, various degradation rates were analyzed. The perovskite degradation rate must be lower than 1.5%/year and 3.1%/year for 2T and 4T configurations, respectively, assuming no degradation in the silicon single-junction cell and the tandem cell's bottom cell.

Contents

Nomenclature

Abbreviations

Abbreviation	Definition
ASA	Advanced semiconductor analysis
c-Si	Crystalline silicon
CB	Conduction band
IEC	International electrotechnical commission
LSE	Light soaking effect
OC	Open-circuit
PV	Photovoltaic
pvk	Perovskite
SC	Short-circuit
SHJ	Single hetero junction
VB	Valence band
2T	Two-terminal
3T	Three-terminal
4T	Four-terminal

Symbols

Symbol	Definition	Unit
C	Constant determining tolerable degradation rate	
c	Speed of light	[m/s^2]
DHI	Direct horizontal irradiation	[W/m^2]
DNI	Direct normal irradiation	[W/m^2]
E	Energy	[eV]
E_G	Bandgap energy	[eV]
FF	Fill factor	[%]
h	Planck's constant	[m^2/kg/s]
I	Current	[A]
I_{MPP}	Maximum power current	[A]
I_{nor}	Normalized irradiance	
I_{SC}	Short-circuit current	[A]
I	Irradiance	[W/m^2]
J_0	Saturation current density	[A/m^2]
J_{ph}	Photogenerated current density	[A/m^2]
J_{SC}	Short-circuit current density	[A/m^2]
N	Sample number	
n	Ideality factor	
P	Power	[W]
P_{max}	Maximum power	[W]
P_{min}	Minimum power	[W]
P_{MPP}	Maximum power point power	[W]
RH	Relative humidity	[%]
R_s	Series resistance	[Ω]
R_{sh}	Shunt resistance	[Ω]

Symbol	Definition	Unit
T	Temperature	[°C]
T_a	Ambient temperature	[°C]
T_g	Ground temperature	[°C]
T_M	Module temperature	[°C]
T_{sky}	Sky temperature	[°C]
V	Voltage	[V]
V_{MPP}	Maximum power point voltage	[V]
V_{OC}	Open-circuit voltage	[V]
σ	Standard deviation	

1
Introduction

To keep the global temperature rise below 2 °C with respect to pre-industrial times, and reach the goals of the Paris Agreement [1], a shift towards a more sustainable energy society is needed. To decrease CO_2 emissions, energy resources like solar and wind, which has zero emissions once installed, can be used to produce electricity. One of the most abundant renewable energy sources is solar energy. The total added installed PV power has grown from 18 GW in 2010 to 183 GW in 2021 [2] and the total installed capacity is already above 1 TWp.

The energy yield of a solar module is dependent on the efficiency and the lifetime of one. The efficiency of crystalline-silicon technology, which is the most dominant PV technology in the market with a market share of 95% in 2020 [3], is currently near its theoretical limit, which is primarily determined by the Shockley-Queisser limit. This is a theoretical thermodynamic limit of the conversion efficiency of a semiconductor solar cell. The Shockley-Queisser limit of a single-junction solar cell is approximately 30% [4]. Because of the approaching theoretical efficiency, a step towards a new type of solar cell is needed to increase the energy yield during its lifetime. This could be accomplished by using tandem cells and the Shockley-Queisser limit of a tandem cell is approximately 45.1% [5]. Therefore crystalline-silicon/perovskite tandem cells, later referred to as c-Si/pvk, can reach higher efficiencies, but currently this type is mostly made on lab scale and it is not exactly known what the degradation rate of perovskite is outdoor and this degradation rate of perovskite has a major influence on the energy yield during its lifetime. The PV module's specifications are determined under standard test conditions (STC), but when installed, the circumstances are different at the site location, because of uncontrollable environmental conditions like humidity and light. These conditions have large influence on the module's performance outside and therefore PV system manufacturers must guarantee at least 80% of the power output after 25 years with respect to year 0. This corresponds to a maximum degradation rate of 0.8% per year for single-junction modules. Because tandem cells are relatively new and are only for research at this moment, it is unclear how the degradation will affect the energy yield of a tandem module, since it has major stability issues. [6]

In this chapter, the most important topics from the literature study are discussed. First in Section 1.1, an explanation about photovoltaic technology is given. Then in Section 1.2, the theory behind tandem cells is explained. Hereafter in Section 1.3, degradation in solar cells is discussed in more detail, followed by an explanation of the PVMD Toolbox in Section 1.4. In Section 1.5, different degradation models are discussed. Finally in Section 1.6, the knowledge gap and the thesis objective are presented together with the outline of this report.

1.1. Photovoltaic Technology

In solar cells, light from the sun is used to produce electricity. This light is absorbed and can generate electricity. In this section, the basic principles of PV technology are discussed.

1.1.1. Working principle of a solar cell

The sun's energy can be transformed into electricity using a solar cell. The sunlight comprises photons, and the energy of an individual photon can be determined using the following equation:

$$E = \frac{h \cdot c}{\lambda} \tag{1.1}$$

In this formula, h is Plank's constant, c is the speed of light and λ is the wavelength of a photon. The spectral irradiance can be characterized as a function of wavelength and this can be visualized with the AM1.5 spectrum defined by IEC. This spectrum is based on the irradiance on the earth's surface on a cloudless day. In Figure 1.1 the AM1.5 spectrum is shown.

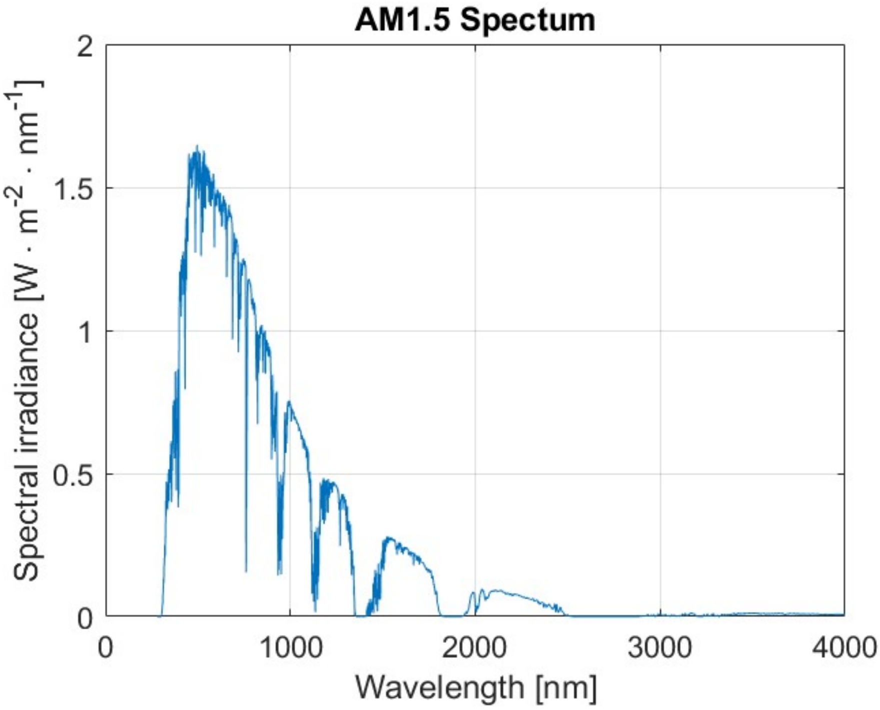

Figure 1.1: The AM1.5 spectrum described by IEC. The total radiation in mW/cm$_2$/nm for every wavelength ranging from 0 to 4000 nm [7]

A solar cell can partially capture photons emitted by the sun and to achieve this, a semiconductor material is used. This material has two energy bands where electrons can be located, and the energy difference between these two bands is known as the bandgap energy (E_g). In Figure 1.2, the bands of a semiconductor material are shown. The two bands are the conduction and valance band indicated as CB and VB, respectively. The energy of a photons can be transferred to an electron in the VB and the electron can move to the CB. When photons have a larger energy than the bandgap energy, the solar cell is able to produce electricity, because an electron-hole pair can be formed. The difference between the bandgap energy and photon energy cannot be used in single-junction solar cells and are called thermalization losses. All the photon energies that are below the bandgap are called below bandgap losses. As mentioned before, the theoretical efficiency is determined by the Shockley-Quiesser limit and is determined by the thermalization losses, below bandgap losses and radiative recombination and the theoretical maximum is 29.4% if crystalline-silicon is used as semiconductor [8]. Compared to other materials, the dominant intrinsic carrier recombination process in c-Si cells is auger recombination. [9] Auger recombination involves the energy from the formation of an electron-hole pair being transferred to other electrons or holes within the same energy band that are in a higher energy state. [10]

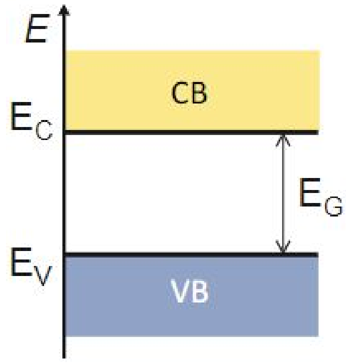

Figure 1.2: A semiconductor material with the corresponding bands

1.1.2. IV-curve of a solar cell

A key characteristic of a solar cell is the IV-curve, where the voltage and current are plotted against each other. In Figure 1.3 an example of an IV-curve is shown, together with a PV-curve.

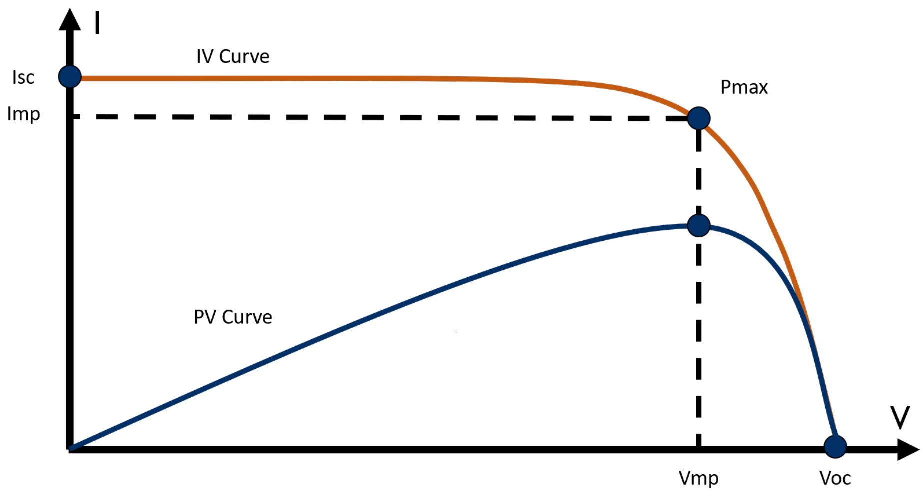

Figure 1.3: IV&PV-curve of a solar cell. [11] The important parameters in the solar cell like current, voltage and power are labelled.

In this figure the following parameters are denoted:

- **Short circuit current (I_{SC}):** When there is no voltage over the solar cell, a short circuit is created and this is denoted as the short circuit current.
- **Open circuit voltage (V_{OC}):** The open circuit voltage refers to the voltage when no current is flowing through the cell.
- **Maximum power point (P_{MPP}):** The maximum power point is the point where the power output is maximized. The blue curve in Figure 1.3 indicates the PV curve, where the maximum power output is denoted as P_{max}.
- **Voltage maximum power point (V_{MPP}):** The voltage maximum power point is the voltage where the power output is maximized.
- **Current maximum power point (I_{MPP}):** The current maximum power point is the current where the power output is maximized.
- **Fill factor(FF):** The fill factor is the ratio between the power at the maximum power point and the product of V_{OC} and I_{SC}. The fill factor is also described as the squareness of an IV-curve. The closer this value is to 1, the better. It can be described as the following equation:

$$FF = \frac{I_{MPP} \cdot V_{MPP}}{I_{SC} \cdot V_{OC}} \tag{1.2}$$

1.1.3. Five-parameter model

In the single diode model, also referred to as the five-parameter (5P) model, the electric behaviour of a solar call can be described. In Figure 1.4, the 5-Parameter model is shown.

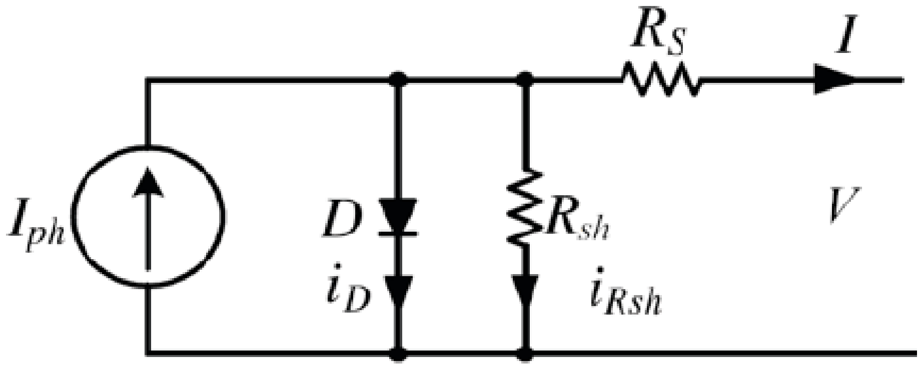

Figure 1.4: Five-parameter model, which describes the electric behaviour of a solar cell. It consists of two resistances, one diode and a current source. [12]

The 5-Parameter model consists of five parameters:

- **Shunt resistance (R_{sh}):** The shunt resistance represents the ohmic losses, which are caused by leakage currents. [13] For an ideal solar cell this value is ∞.
- **Series resistance (R_s):** The series resistance represents the ohmic losses in the solar cell's contacts and the bulk. [14] For an ideal solar cell this value is 0.
- **Photogenerated current (I_{ph}):** The photon current is the value of the current source. It is the number of the generated electron-hole pairs in the cell. [15]
- **Saturation current (I_0):** The saturation current represents the recombination losses in the solar cell and it is a diode characteristic.
- **Ideality factor (n):** The ideality factor indicates which recombination mechanism is most dominant and is also a diode characteristic.

The output can be written as Equation 1.3.

$$I = I_{PH} - I_0\left(e^{(\frac{V+I\cdot R_S}{n\cdot V_{th}})} - 1\right) - \frac{V + I \cdot R_S}{R_{SH}} \tag{1.3}$$

1.2. Tandem solar cells

As described before, tandem solar cells can reach higher efficiencies compared to single-junction solar cells. In this section, the basic principles and challenges of tandem solar cells are explained. First the working principles of tandem cells are explained and then the different connections between the sub cells are discussed. Finally, the tandem cell of interest, c-Si/pvk, is discussed.

1.2.1. Working principle of tandem solar cells

The most limiting factors of solar cells are thermalization losses and below band gap losses. To reduce these losses, a second material can be added to a solar cell to make a tandem cell. In Figure 1.5, the difference between the two different technologies is shown. Because of two separate bandgap energies, the total energy that can be produced is higher for a tandem. The material that has the highest bandgap is placed on top, so that the short wave lengths are absorbed and the long wavelengths are transmitted and are partially absorbed by the lower bandgap material. A short wavelength corresponds to a photon with a high energy, which is evident from Equation 1.1

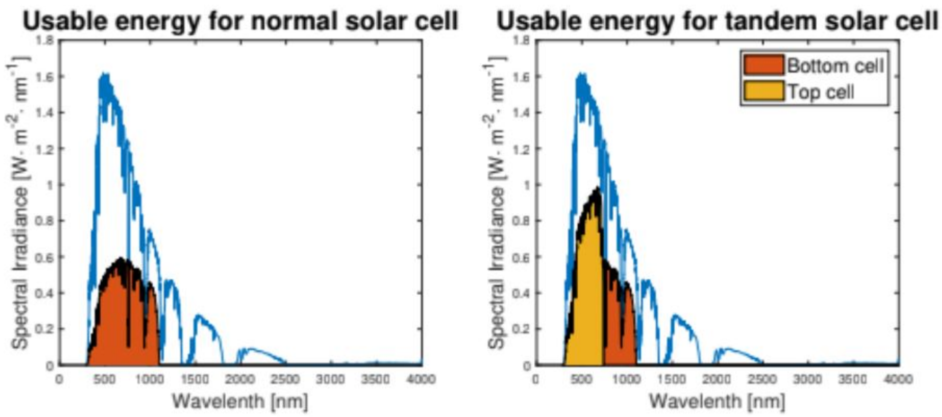

Figure 1.5: Difference in energy that can be used for a single solar cell compared to a tandem solar cell [16]

1.2.2. Different tandem cell connections

There are different electrical configurations for tandem cells: two, three and four terminal (2T), (3T) and (4T). These configurations represent innovative designs that aim to enhance the efficiency and performance of solar cells. In figure 1.6, the difference between 2T, 3T 4T is shown. In 2T connections, the current through the solar cells must be the same for both layers, and thus needs to be matched. These sub cells are connected in series and by changing the layer thicknesses, the currents can be matched.

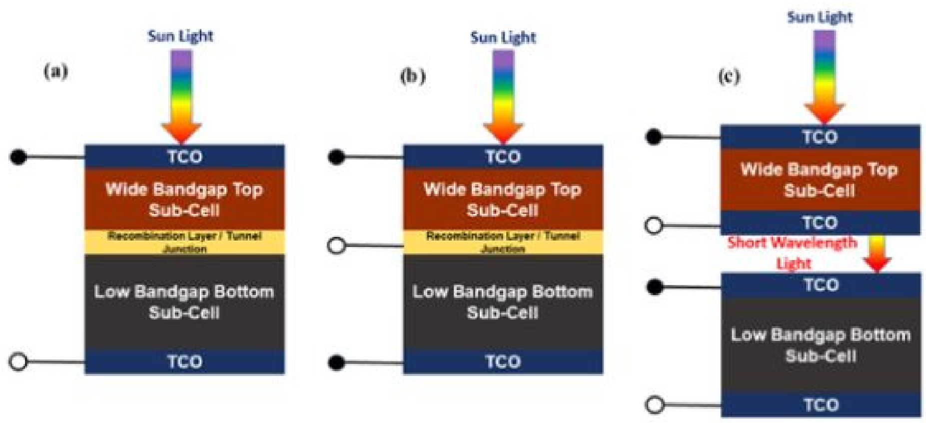

Figure 1.6: Two, three and four terminal connection in a tandem cell [17]

The thickness of the top layer determines the absorption in the material and so the transmitted photons and these transmitted photons will reach the bottom cell. [17]

In 4T tandem cells, the current does not needs to be matched. As can be seen in figure 1.6, both the top cell and bottom cell are connected separately. In this design, no current and voltage matching is needed, overcoming limitations posed by traditional 2T structures. The disadvantages of 4T are that this type of configuration is harder to make and the parasitic absorption is higher. [17]

A newer connection, 3T configuration, uses a contact that is shared by both sub-cells [18], providing independent control over the voltage and current of each layer. This design enhances the flexibility in material choices and allows for more precise matching of sub cell characteristics and combines the advantages of 2T and 4T. [19]

1.2.3. C-Si/pvk tandem solar cells

Two materials that can be used together in a tandem cell are crystalline-silicon and perovskite. This combination is a promising structure since perovskite has low costs, it has a tunable bandgap, a large absorption coefficient and the fabrication process is relatively easy [20, 21].

Crystalline-silicon is the most used material in PV solar cells with a market share of 95% [3]. This material has a bandgap of 1.12 eV at room temperature. This material is used due to a combination of its long-term stability, abundance/availability, and suitability for large-scale production. This together with the advantages of perovskite makes this tandem cell configuration an interesting one. [22, 23]

In Figure 1.7 a c-Si/pvk configuration is shown. On the left side 4T and 2T configurations are shown and on the right side a n-i-p and p-i-n configuration are shown. Currently, efficiencies above 31% are measured for tandem cells [24], which is higher than the theoretical efficiency of single-junction solar cells. Therefore, perovskite shows promise for tandem solar cells, yet it faces challenges. As mentioned previously, the stability of perovskite is not ideal and the degradation rate is high because of factors such as moisture and high light intensity.

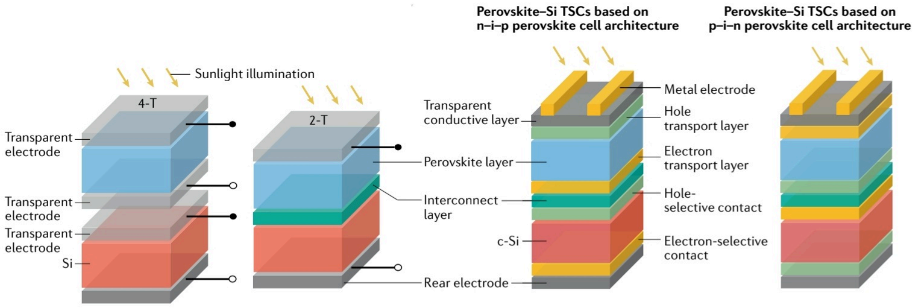

Figure 1.7: Crystalline silicon-perovskite tandem cell configuration[25]

1.3. Degradation in PV modules

As mentioned before, the degradation in solar cells are an important aspect for PV module manufacturers, because they must guarantee at least 80% of the power output after 25 years with respect to year 0. In tandem cells, the degradation of both sub cells affecting the total degradation rate of one. In this section, degradation is discussed and this is done by distinguishing between two different degradation types: reversible and irreversible degradation. Hereafter, degradation in perovskite solar cells is discussed.

1.3.1. Reversible degradation

Reversible degradation in solar cells refers to temporary performance declines that can be mitigated or reversed under specific conditions. This phenomenon is crucial to understand as it affects the overall reliability of the solar cell. Reversible degradation mechanisms recovers overnight and several factors contribute to reversible degradation: the effects of light, temperature and electric field. [26]

1.3.2. Irreversible degradation

Irreversible degradation refers to losses in the solar cell that cannot recover overnight and permanently impact the performance of the PV solar cell. These losses can be caused by factors such as corrosion and humidity. Addressing irreversible degradation is crucial for improving the long-term reliability of solar cell technologies. Strategies such as improved encapsulation techniques and advanced materials are continually being explored to enhance the durability and efficiency of solar cells in real-world applications. [26]

1.3.3. Degradation in perovskite solar cells

In this subsection the most import degradation mechanisms in perovskite solar cells are explained. The two most important degradation mechanisms in perovskite solar cells are discussed, which are: the light-soaking effect, corrosion in solar cells and moisture&humidity.

Light-soaking effect (LSE)

The light-soaking effect is one of the major instability issues in perovskite solar cells. This means that the solar cell's performance changes with time under illumination. The current and open circuit voltage are increased during the first minutes of the light-soaking effect together with the power. Mosconi et at. [27] found that, in these first minutes, the amount of defects decreased and therefore an increase in efficiency is found. However, after these first minutes of light-soaking, the degradation starts and can cause the efficiency to drop by 10-30% during operation after several hours. This power drop can recover overnight and therefore the light-soaking effect is a reversible degradation mechanism. In a recent study by Remec et al., the light-soaking effect was extensively investigated, revealing its significant susceptibility to daily conditions. The light-soaking effect is further influenced by daily cumulative irradiance and operating temperature, with losses varying considerably based on geographical location and climatic conditions [28].

Corrosion in perovskite solar cells

Corrosive elements like salt or airborne pollutants can cause the metal contacts and other components within a solar cell to corrode. Corrosion can affect electrical connections and reduce the overall efficiency of the cell. To reduce the effect of corrosion on degradation, anti-corrosion strategies such as passivation, surface coating and machining can be used. [29]

Moisture&humidity in perovskite solar cells

Humidity is referred to as the concentration of water vapor in the air and moisture is the amount of water that has been diffused into a material. Moisture can cause instability in the perovskite material and can lead to irreversible degradation. Water molecules can cause the degradation of the perovskite crystal structure, affecting the performance of the solar cell. Encapsulation and protective layers are employed to shield perovskite solar cells from moisture, allowing for recovery when the cells are kept in a dry environment, so that the water molecules can escape. [30, 31]

1.4. PVMD Toolbox

The PVMD Toolbox is a simulation tool that can calculate the energy yield of a PV system using the material properties in the device and using self-consistent models. [32] This toolbox operates without any measurement in a PV device and it combines wave and ray optics and a semiconductor simulation to model the optoelectronic PV properties which results in an IV-curve. Ray tracing is used to obtain an irradiance distribution from the system surroundings and through the fluid dynamics-based model for the cell temperatures. For every hour of the year an IV-curve is made and with an inverter, the AC energy yield is calculated. In this section, all seven parts indicated in Figure 1.8 are explained.

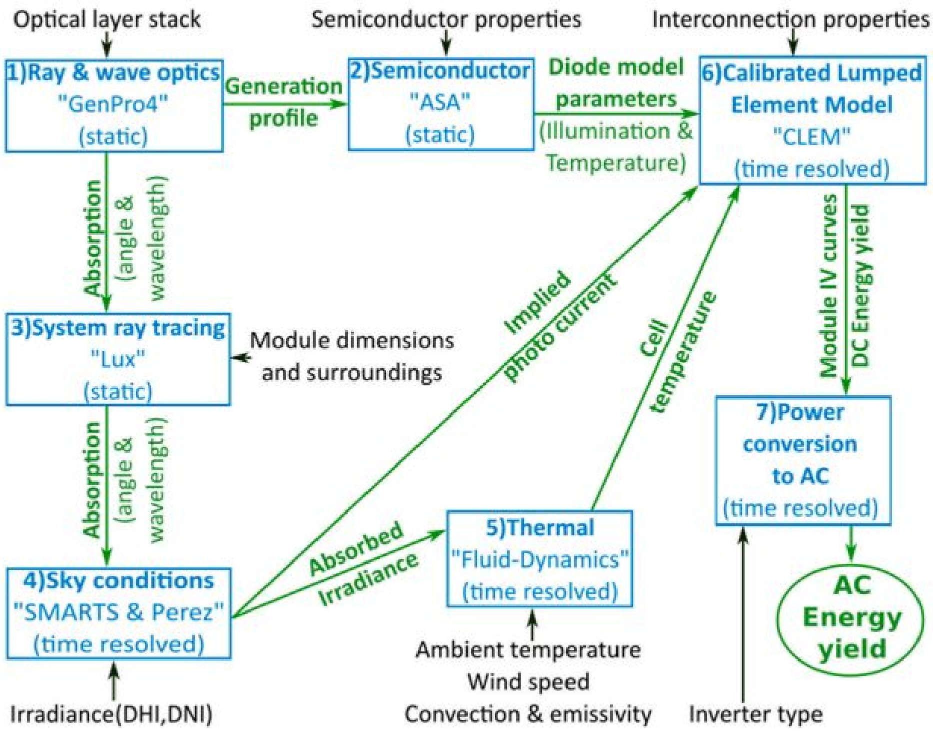

Figure 1.8: PVMD Toolbox flowchart for the simulation. The input data, the main models and the results are given in black, blue and green, respectively. [32]

1.4.1. Ray & wave optics

To calculate the PV module's optical properties, GenPro4 software [33] is used. With this program the absorption, transmission and reflection are calculated for each layer with the given layer thickness and refractive indexes $(n(\lambda) + i \cdot k(\lambda))$. By using the net radiation method [34], the different outputs can be calculated by the GenPro4 software. [35]

1.4.2. Semiconductor

In figure 1.8 it can be seen that the main used model for the semiconductor is the Advanced Semiconductor Analysis (ASA) model [36], where the Poisson equation and continuity equations for holes and electrons are solved in 1D for different conditions. As illustrated in Figure 1.8, the input is the semiconductor properties, which are the layer's properties, such as electron-hole concentrations and electric potential. With the ASA model, IV-curves can be made for different cell temperatures and irradiances.

1.4.3. System Ray Tracing

The system ray tracing uses the LUX software [37] as main model, as can be seen in figure 1.8, where the software uses the Monte-Carlo ray tracing method, where albedo effects and shading are used. The absorption, coming from the ray&wave optics part, is used in this particular modelling part.

1.4.4. Sky conditions

For the sky conditions, the main models that are used are: SMARTS [38] & Perez's [39] model. Perez' model is used to model the sky luminance pattern. SMARTS is used to obtain the irradiance's or photon flux' spectral composition. The input parameters for this modelling part are the irradiances DHI and DNI. In the current version of the toolbox, SBDART [40] can be used as well, where the difference between diffused and direct light can be modelled. In this part of the toolbox, either SBDART or SMARTS can be used to model the sky luminance pattern.

1.4.5. Thermal model

For the thermal model, the fluid-Dynamic model is used. In this modelling part, the absorbed irradiance from the sky conditions are used, as well as other input parameters, which are: ambient temperature, wind speed, convection and emissivity. All these different heat flows result in one equation for the module temperature. This can be written as the following [15]:

$$T_M = \frac{\alpha G + h_c T_a + h_{r,sky} T_{sky} + h_{r,gr} T_g}{h_c + h_{r,sky} + h_{r,gr}} \tag{1.4}$$

The temperature of the module is an important parameter for other parameters like the FF and V_{OC}.

1.4.6. Calibrated Lumped Element Model

In this modelling part, a calibrated lumped element model (CLEM) is made. From the 5-Parameter model, which is discussed in subsection 1.1.3, this model is created and is used to make IV-curves with parameters that are dependent on temperature and irradiance.

1.4.7. Power conversion to AC

The last step is the power conversion from DC to AC. From the module's IV-curves, and the number of modules in parallel and series, the DC energy yield is determined and with the chosen inverter type this is converted to the total AC energy yield.

1.5. Degradation models

Currently, the Kaaya model [41] is utilized in the PVMD toolbox to model degradation. However, this model cannot be applied to simulate degradation in tandem solar cells. In this section the Kaaya model and a possible degradation model for tandems are discussed.

1.5.1. The Kaaya model

In a previous thesis from Abishek Velpuru [42], a model is made based on a paper referred to as the Kaaya model and currently, the PVMD toolbox uses the Kaaya model. In this thesis, three major degradation mechanisms are modelled: hydrolysis, photo-degradation and thermo-mechanical degradation. In this model, the module's mean temperature, relative humidity (RH) and UV are taken into account However, this model is not usable for tandems, because it only provides information about the power performance over time, but nothing about the voltage/current drop and this model is calibrated for c-Si modules. Next to that, the Kaaya model cannot be used for 2T solar cells, because it is based on measured data. Since 2T tandem cells must have the same values for current and voltage, it is important to know how the degradation relates to these values.

1.5.2. The Qian model

Qian et al. [43] looked into the impact on the lifetime energy yield in perovskite solar tandem cells. In this report, two- and four-terminal tandem cells were modelled using different device parameters. For 2T&4T tandem cells, the resulting power degradation is simulated using electrical and optical degradation mechanisms. The current and voltage are simulated with the single diode model and these are solved explicitly where the Lambert W function is used. Three module degradation components are considered: The encapsulation material, the perovskite cell and the silicon cell. In this paper, the mechanical damage caused by thermal expansion is not taken into account.

1.6. Knowledge gap & thesis objective

As mentioned in section 1.4, the PVMD group at the Delft University of Technology, developed the PVMD Toolbox to calculate the energy yield of a PV system [32]. Currently, a proper degradation rate of perovskite in tandem cells has not been implemented in the toolbox yet and therefore a detailed model of the degradation in c-Si/pvk tandem cells will be made. The main goal of this thesis is:

"Compare the energy yield of a crystalline-silicon/perovskite tandem with degradation included to conventional silicon modules"

This will be done not only for the first year of operation, but during their entire lifetime in various climate conditions and with different tandem cell configurations. This will be done by making a numerical model to find the parameters from the 5-Parameter model which influences degradation and use this for numerical simulations of the lifetime energy yield to find the desired perovskite degradation rate. In this thesis both 2T and 4T will be used (3T is beyond the scope of this thesis). To achieve the main goal of this thesis, three sub-goals are defined:

Sub-goal 1: "Determine electrical parameters from single diode equation"
The first goal is to make a model to find the parameters from the single diode equation to estimate the degradation in a perovskite cell. This will be done by making a model to determine these electrical parameters using experimental data from outdoor measurements .

Sub-goal 2: "Perform lifetime energy yield simulations when degradation is included"
The goal of the second step is to perform lifetime energy yield simulations in the PVMD Toolbox applying different degradation scenarios and compare these to a single-junction module when degradation is included.

Sub-goal 3: "Find maximum tolerable perovskite degradation rate"
The final step is to use different degradation rates to determine what degradation rate of perovskite is tolerable in order to have a higher lifetime energy yield after 25 years for a tandem module compared to a single-junction module, where different degradation rates will be used.

1.7. Thesis outline

This thesis is divided into 5 main Chapters. In Chapter 2, the goal is to determine the electrical parameters from the single diode equation. This is done by using the 5-Parameter model together with experimental data of a degraded perovskite cell. In Chapter 3, the goal is to perform lifetime energy yield simulations when degradation is included. These lifetime energy yield simulations are based on the degraded parameters obtained in Chapter 2, where 2T and 4T tandem modules are compared to single-junction modules. In the same Chapter, the energy yield is compared across four different locations. Then, in Chapter 4, the goal is to find the maximum tolerable perovskite degradation rate. To find this maximum tolerable degradation, a tandem module is compared to a single-junction module in order to have a higher lifetime energy yield after 25 years, where different degradation rates are used. Lastly, in Chapter 5, this thesis is concluded together with the recommendations of this research.

2

Determination of electrical parameters of a degraded perovskite solar cell: Methodology and analysis

The first sub-goal of this thesis, described in Section 1.6, is to determine the electrical parameters from the single diode equation. In this chapter, the methodology and analysis for the determination of the electrical model parameters are explained and discussed. The understanding of these parameters is essential, because these parameters are used to estimate the degradation rate in a perovskite cell.

First in Section 2.1, the physical meaning of the parameters of the 5-Parameter model is explained together with the method. Secondly in Section 2.2, information about the used data sets is provided. Then in Section 2.3, the extraction of the parameters out of the data set is discussed. Hereafter in Section 2.4, the results are validated. In Section 2.5, IV-curve comparisons are shown and finally in Section 2.6, this chapter is concluded.

2.1. Electrical model behavior and method determining parameters

In Section 1.1.3, the 5-Parameter model was briefly explained and in this section, these parameters are provided by exploring the physical significance of each. First, the saturation current and ideality factor are explained and hereafter, the shunt and series resistances are explained and finally, the photocurrent is explained. Hereafter, the method of extracting the parameters from available data is explained. Later, these parameters will be used to simulate the degradation in the perovskite top cell.

2.1.1. Equivalent circuit parameters

In this subsection, the five parameters from the equivalent circuit are explained, which are used to generate IV-curves.

The saturation current

The saturation current, denoted as I_0, and the saturation current density, denoted as J_0, are also referred to as the dark saturation current (density). This current flows through the solar cell in absence of light and is mainly influenced by the recombination of charge carriers within the cell. A lower saturation current indicates a higher quality solar cell, as it suggests fewer recombination losses. [44]

In Subfigure 2.1a, the effect of varying the saturation current is depicted. It is evident that reducing the saturation current enhances the maximum power output, demonstrating its beneficial impact on the cell's performance.

The ideality factor

The ideality factor quantifies the degree of non-ideality in diode behavior, where it also is an important variable to determine the dominant recombination mechanism within the solar cell. In an ideal diode model, n assumes a value of 1, which indicates a perfect diode behavior consistent with theoretical expectations. However, real diodes exhibit deviations from ideal behavior due to various physical phenomena occurring within the device structure. A higher ideality factor accounts for increased deviations from ideal behavior, indicating the presence of additional non-idealities within the diode and a lower ideality factor suggests closer alignment with ideal diode characteristics. [45]

In Subfigure 2.1b, the influence of changing the ideality factor is shown and the other parameters are kept constant. It is shown that a higher ideality factor accounts for a shift in IV-curve to the right. While the physical meaning of the ideality factor stated that a lower ideality factor is beneficial, this plot does not make sense. By increasing the ideality factor, the V_{oc} increases, but at the same time, the FF decreases and the internal losses increases. Only an increase in the ideality factor is unrealistic and this usually goes along with an increase in the saturation current.

The shunt resistance

Shunt resistance, denoted as R_{sh}, represents the resistance parallel to the diode's junction and it is used to model leakage current paths across the p-n junction, typically due to defects or contamination in the cell. High shunt resistance indicates minimal leakage currents, which is desirable for efficient solar cell operation. Higher shunt resistance reduces leakage currents and improves diode performance. [46]

In Subfigure 2.1c, the influence of changing the shunt resistance is illustrated. It is illustrated that a lower shunt resistance increases the slope of the line through the current axis and this results in a lower FF and maximum power output.

The series resistance

Series resistance, denoted as R_s, represents the resistance encountered by the flow of current through the semiconductor material and metal contacts of the diode and therefore indicates the resistive losses in the solar cell. Lower series resistance is preferable as it allows more of the generated current to reach the load, thereby increasing the cell's output power and efficiency. [47] In Subfigure 2.1d, the influence of changing the series resistance is illustrated. It can be seen that a higher series resistance decreases the slope of the line through the voltage axis and this results in a lower FF and maximum power output.

The photocurrent

When a solar cell is exposed to sunlight, their energy can excite electrons from the valence band to the conduction band and this creates electron-hole pairs. The amount of electron-hole pairs generated in a solar cell is the photocurrent, which is denoted as I_{ph}. This variable is essential in determining the efficiency and performance of a solar cell. [48]

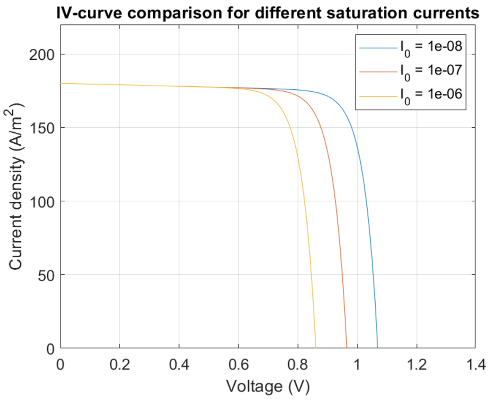

(a) IV-curve comparison for different saturation currents

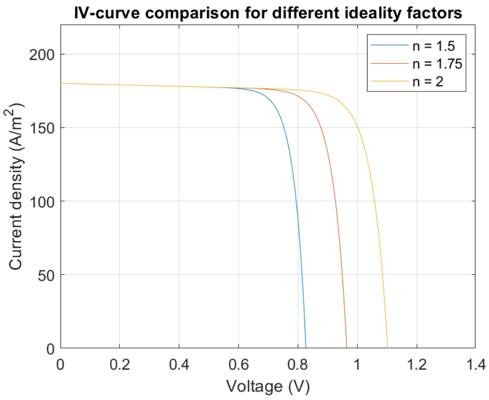

(b) IV-curve comparison for different ideality factors

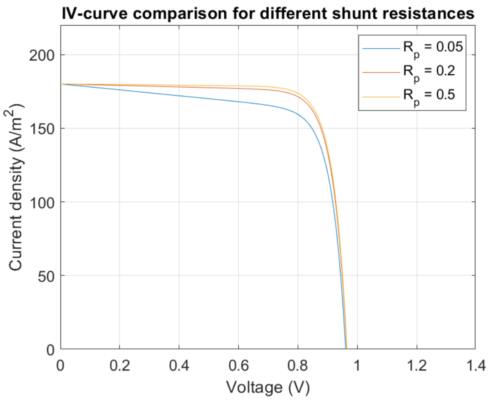

(c) IV-curve comparison for different shunt resistances

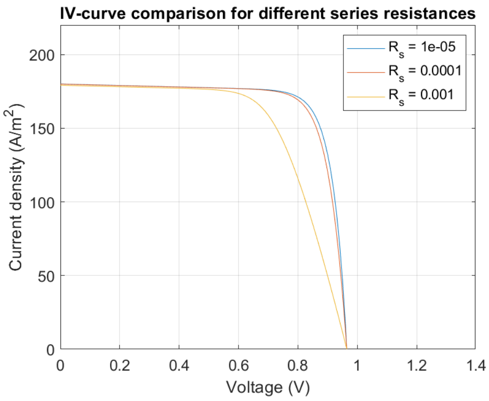

(d) IV-curve comparison for different series resistances

Figure 2.1: IV-curve comparison for different saturation currents, ideality factors, shunt resistances and series resistances

2.1.2. Reconstructing IV-curves

IV-curves can be reconstructed with five electrical parameters, outlined in Section 1.1.3. These parameters are essential for long-term analysis of the electrical model for a perovskite solar cell. In Figure 2.2, an IV-curve is shown with corresponding information on series and shunt resistance, as well as the maximum power point.

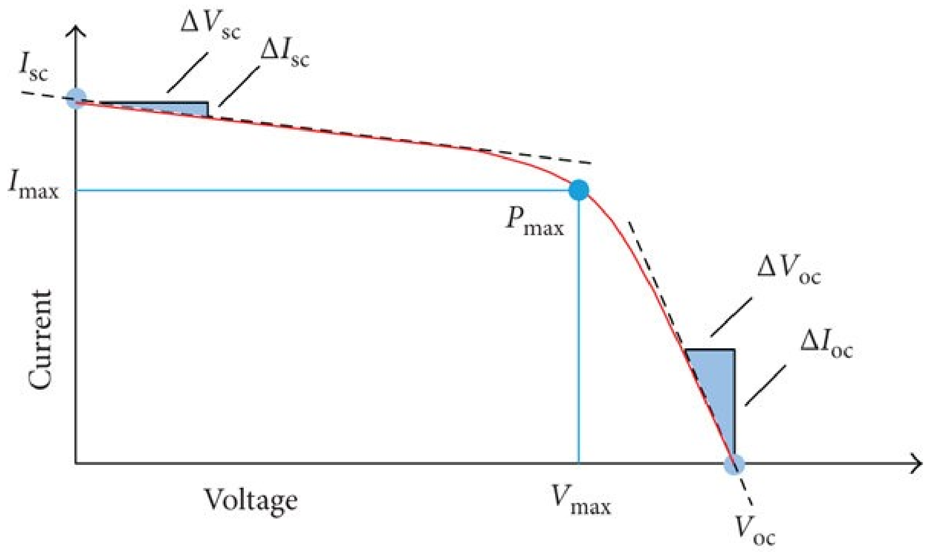

Figure 2.2: IV-curve with corresponding information to determine the shunt and series resistance. [49]

The shunt and series resistances can be determined by using the following equations:

$$R_{sh} = -\frac{\Delta V_{sc}}{\Delta I_{sc}} \tag{2.1}$$

$$R_s = -\frac{\Delta V_{oc}}{\Delta I_{oc}} \tag{2.2}$$

From these equations can be concluded that a higher shunt resistance and a lower series resistance are more beneficial for power generation, which was also explained in Section 2.1. A higher R_{sh} will lead to a lower slope, which will result in a more horizontal line towards the intersection at I_{sc}. A lower R_s will lead to a higher slope, which will result in a more vertical line towards the intersection at V_{oc}. The combination of the ideality factor, saturation current and the resistances determine the shape of the IV-curve. The photocurrent, which is approximately equal to the short circuit current, determines the intersection point with the current axis. The total equation to reconstruct IV-curves can be written as:

$$I = I_{\text{ph}} - I_0 \left(e^{\frac{V + I \cdot R_s}{n V_{\text{th}}}} - 1 \right) - \frac{V + I \cdot R_s}{R_{\text{sh}}} \tag{2.3}$$

2.1.3. Method of determining parameters form 5P model to simulate degradation

Since the current in equation 2.3 also depends on the current, an alternative way is needed to calculate the current. This can be done by using a Lambert W function, which is shown equation 2.4 and this equation can be used to calculate the current output which is shown in equation 2.5.

$$z = \frac{R_s \cdot I_0}{n \cdot V_{\text{th}} \cdot (1 + \frac{R_s}{R_{sh}})} \cdot \exp\left(\frac{R_s \cdot (I_{\text{sc}} + I_0) + V}{n \cdot V_{\text{th}} \cdot (1 + \frac{R_s}{R_{sh}})} \right) \tag{2.4}$$

$$I = \frac{(I_{\text{sc}} + I_0 - \frac{V}{R_s h})}{1 + \frac{R_s}{R_{sh}}} - \text{LambertW}(z) \cdot \frac{n \cdot V_{\text{th}}}{R_s} \tag{2.5}$$

Now I_{MPP} and V_{MPP} are estimated and the desired values of FF, V_{oc} and P_{MPP} are estimated by minimizing the error, where the error can be formulated as the following equation:

$$\text{error} = |FF - FF_{\text{data}}| + |P_{\text{mpp}} - P_{\text{mpp,data}}| + |V_{\text{oc}} - V_{\text{oc,data}}| \tag{2.6}$$

In equation 2.6, FF_{data}, $P_{\text{MPP,data}}$, and $V_{\text{OC\_data}}$ represent the values obtained during measurements, which are the desired values. The following equations are used to determine the desired values of FF, P_{mpp} and V_{oc}:

$$FF = \frac{P_{\text{mpp}}}{V_{\text{oc}} \cdot I_{\text{sc}}} \tag{2.7}$$

$$P_{\text{mpp}} = \max(I \cdot V) \tag{2.8}$$

$$V_{\text{oc}} = V(I = 0) \tag{2.9}$$

Equation 2.9 represents the calculation of the open circuit voltage using the voltage at zero current, where V is an array in steps of 0.001 V and the current is the output of equation 2.5. The maximum power point is calculated by using equation 2.8, where the maximum is the product between the voltage and the current.

2.2. Measurements external cell parameters during degradation

In this section, two available data sets are discussed. First, an outdoor testing of a perovskite solar cell in Slovenia is discussed. Then, the outdoor testing of a tandem cell in Saudi Arabia is discussed.

2.2.1. Outdoor testing perovskite solar cell in Slovenia

In 2019, researchers at the University of Ljubljana [50] conducted outdoor testing of perovskite solar cells over several months, measuring current and voltage at different times throughout the day. Although irradiance data was not recorded, the IV-curves obtained from these measurements were used to derive the electrical parameters from the 5-Parameter model, which was explained in Section 2.1. During this study, several perovskite cells were tested and the maximum power output decreased and the degradation rate increased. Unfortunately, these small perovskite cells were not very stable and the degradation rate at the end of testing was high.

To estimate reasonable values for n, J_0, R_{sh} and R_s from real IV-curve measurements obtained during outdoor testing in Slovenia [50], Matlab is used. In Figure 2.3, two measurements that have been done in the first two weeks of testing, are shown with the corresponding fit that has been determined. Both measurements were done at 10:03, but on different dates. The fits demonstrate a close alignment with the measured data, and similar fitting processes were applied to all IV-curves collected during the study.

In Table 2.1, the parameters that determines the fitting curve are shown. This data was only relevant to get an idea of what the approximate values for the degraded solar cells should be to get an estimate of the initial guesses for the numerical method, which was discussed in Subsection 2.1.3.

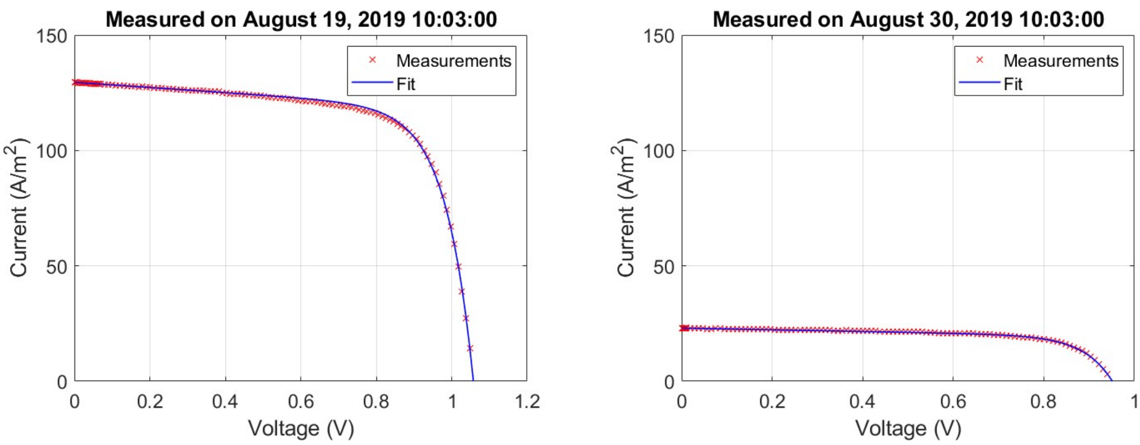

(a) IV-Curve measurement data and fit in Ljubljana at August 19 **(b)** IV-Curve measurement data and fit in Ljubljana at August 30

Figure 2.3: IV-Curve measurement data and fit in Ljubljana at different dates

Table 2.1: Parameters from the fit

	J_{sc} $[A/m^2]$	V_{oc} $[V]$	R_p $[\Omega \cdot m^2]$	R_s $[\Omega \cdot m^2]$	J_0 $[A/m^2]$	n [-]
August 19, 2019	129.5	1.065	0.0899	5.273e-6	6.130e-06	2.7080
August 31, 2019	23.04	0.9598	0.270	1.330e-5	5.650e-07	2.341

2.2.2. Outdoor testing pvk/c-Si solar cell in Saudi Arabia

In 2022, researchers at King Abdullah University of Science and Technology (KAUST) [51] have tested a crystalline-silicon/perovskite solar cell for one year. From these measurement, the short circuit current, open circuit voltage, the fill factor and the power at the maximum power point has been made available. This data is used to determine the values of the 5-Parameter model by using a numerical model. During the testing of this tandem cell, more than 24,000 measurement have been done in one year and with this many data points, a reasonable estimation of the parameters over time can be made.

In Figure 2.4a, the short circuit current density is plotted against the normalized irradiance range (I_{nor}). The observed linear trend aligns with expectations, as J_{sc} is directly proportional to I_{nor}. In Figure 2.4b, the open-circuit voltage is plotted against the short-circuit current density, where the observed trend is logarithmic, which aligns with the expectations. In Figure A.1 in Appendix A the available data points are shown over time.

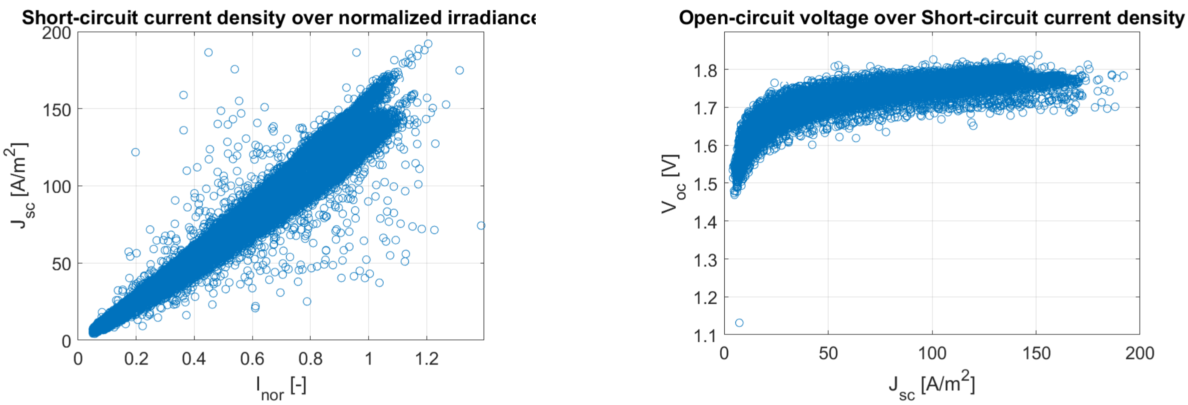

(a) Short-circuit current density over normalized irradiance

(b) Open-circuit voltage over short-circuit current density

Figure 2.4: Correlations of short-circuit current density with irradiance and open-circuit voltage

2.3. Estimating electrical parameters from experimental data

In this section, the extraction of the parameters from the KAUST data set is discussed. Using the method explained in Section 2.1, the parameters from the 5-Parameter model are estimated by using a numerical model. First, the data filtering is discussed and then the saturation current density, ideality factor, shunt resistance and series resistance are shown and this is done by showing the trend lines over time for all these parameters.

Looking at Equation 2.5, there are still 4 unknown values which are not determined by the measurements and these values are estimated by minimizing the error, which is given in equation 2.6. The initial guesses used for the numerical method can be found in Table 2.2 and these values are based on the extracted parameters from the perovskite solar cell tested in Slovenia shown in Table 2.1 .

Table 2.2: Initial guesses for minimizing the function error to calculate J_o, n, R_p, and R_s

	J_0 [A/m^2]	n	R_{sh} $[\Omega \cdot m^2]$	R_s $[\Omega \cdot m^2]$
Initial guess	1e-6	2	0.1	1e-6

2.3.1. Data filtering

Because there are many data points, the estimated values are divided into five different groups, where these groups are based on the measured normalized irradiance. The normalized irradiance ranges are: 0.65-0.75, 0.75-0.85, 0.85-0.95, 0.95-1.05 & 1.05-1.2666, where 1.2666 is the maximum of the measured data. Since the data provided pertains to a tandem cell, the voltage corresponding to the crystalline-silicon bottom cell, which is 0.7V [51], was deducted from the total measured V_{oc}. After calculating all the parameters, outliers for each variable are removed, retaining approximately 95% of the data. This is accomplished by excluding data points that lie outside the range defined by the mean value $\pm 2\sigma$. [52]

2.3.2. Saturation current density

As described in section 2.3, the change in electrical parameters over time are wanted to observe the change in degradation. To achieve this, the parameters are evaluated over time. First of all, the saturation current density (J_0) is evaluated. In Figure 2.5, a semi logarithmic plot is shown for all the ranges discussed in section 2.3.1.

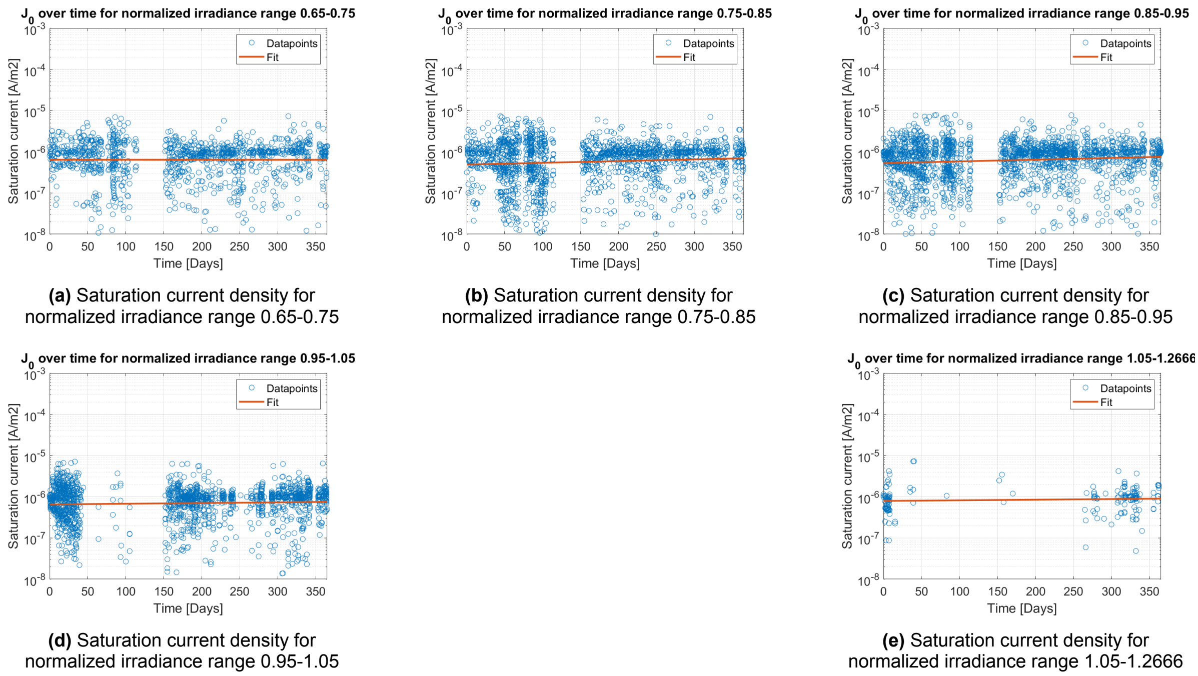

(a) Saturation current density for normalized irradiance range 0.65-0.75

(b) Saturation current density for normalized irradiance range 0.75-0.85

(c) Saturation current density for normalized irradiance range 0.85-0.95

(d) Saturation current density for normalized irradiance range 0.95-1.05

(e) Saturation current density for normalized irradiance range 1.05-1.2666

Figure 2.5: Semi logarithmic saturation current density plots for different normalized irradiance ranges

For all the ranges, a trend line is plotted next to the data points and the formula of each trend line is shown in Table 2.3 and a plot of these trend lines is shown in Figure 2.6. This trend line is linear in this semi logarithmic plot, so the actual increase is 10 to the power of this trend line, which is shown in Table 2.3. From this table it can be seen that most of the lines are increasing over time, which makes sense, since the higher the saturation current density, there are more recombination losses as described in Subsection 2.1.1.

Table 2.3: Saturation current trend lines for normalized irradiance ranges

	Trend line J_0 $[A/m^2]$
I_{nor}0.65-0.75	$J_0 = 10$^$(1.088e - 5 \cdot t - 6.194)$
I_{nor}0.75-0.85	$J_0 = 10$^$(4.081e - 4 \cdot t - 6.310)$
I_{nor}0.85-0.95	$J_0 = 10$^$(4.143e - 4 \cdot t - 6.275)$
I_{nor}0.95-1.05	$J_0 = 10$^$(1.718e - 4 \cdot t - 6.185)$
I_{nor}1.05-1.27	$J_0 = 10$^$(1.888e - 4 \cdot t - 6.120)$

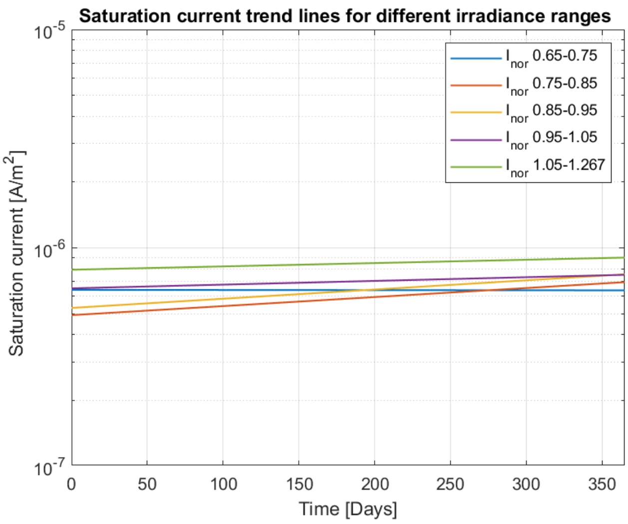

Figure 2.6: Saturation current density trend line comparison for each irradiance range

2.3.3. Ideality factor

For the ideality factor, plots are made for the same normalized irradiance ranges and these are shown in Figure 2.7. From Table 2.4 it is evident that three out of five trend lines are decreasing, which is not what was expected and a plot of these trend lines are shown in Figure 2.6. It is shown that the trend lines for the irradiance ranges are approximately the same value, which implies that the ideality factor is more or less constant over time. In subsection 2.1.1, the physical meaning of the ideality factor was explained and it is expected that the ideality increases over time, because the solar cell becomes less ideal and therefore the recombination increases. The increase over time is not much and therefore the change can be neglected, because of a wide range in data points.

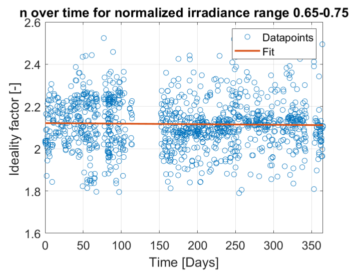

(a) Ideality factor for normalized irradiance range 0.65-0.75

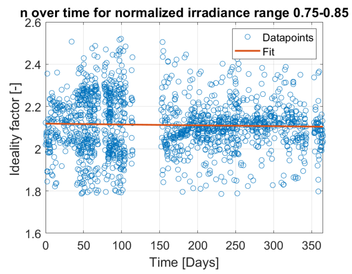

(b) Ideality factor for normalized irradiance range 0.75-0.85

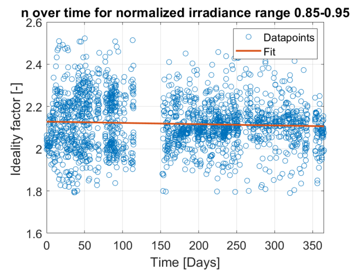

(c) Ideality factor for normalized irradiance range 0.85-0.95

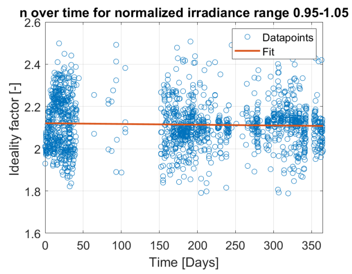

(d) Ideality factor for normalized irradiance range 0.95-1.05

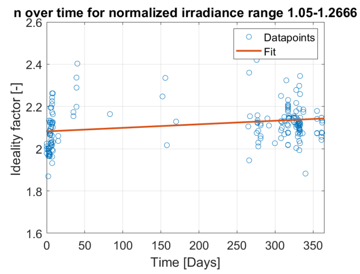

(e) Ideality factor for normalized irradiance range 01.05-1.2666

Figure 2.7: Ideality factor plots for different normalized irradiance ranges

Table 2.4: Ideality factor trend lines for normalized irradiance ranges

	Trend line n $[A/m^2]$
I_{nor}0.65-0.75	$n = -3.169e - 5 \cdot t + 2.122$
I_{nor}0.75-0.85	$n = -4.054e - 5 \cdot t + 2.120$
I_{nor}0.85-0.95	$n = -6.129e - 5 \cdot t + 2.129$
I_{nor}0.95-1.05	$n = -2.901e - 5 \cdot t + 2.120$
I_{nor}1.05-1.27	$n = 1.082e - 5 \cdot t + 2.101$

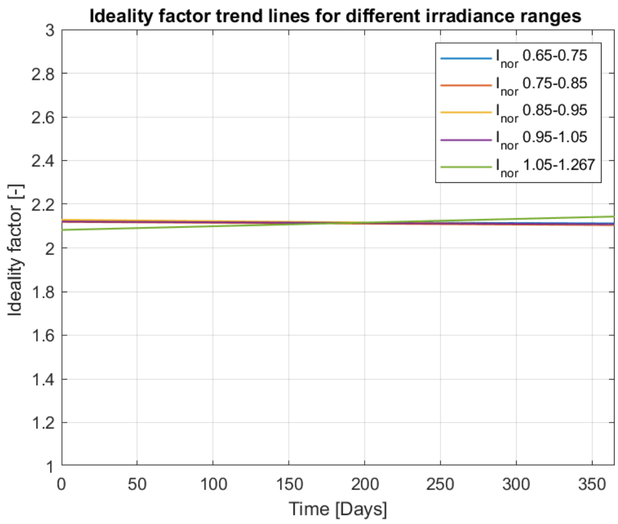

Figure 2.8: Ideality factor trend line comparison for each irradiance range

2.3.4. Shunt resistance

For the shunt resistance, plots are made for the same normalized irradiance ranges and these are shown in Figure 2.9. From Table 2.5 and Figure 2.10 it is shown that the shunt resistance is decreasing over time and in Subsection 2.1.1, this parameter was explained and it makes sense that this parameter is decreasing over time. Since there should be degradation after one year, the leakage current due to defects should increase and therefore a decrease in shunt resistance is expected. The higher the R_{sh}, the lower the leakage current, which is desirable for the efficiency of the solar cell. In Figure 2.9, a clear slope in the trend lines can be seen

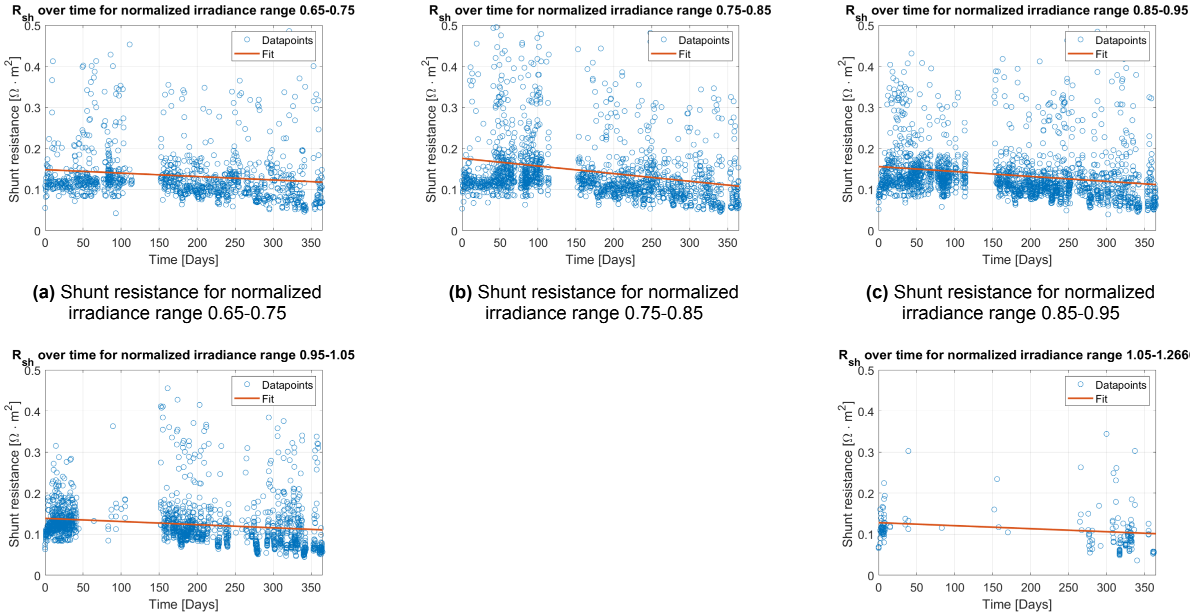

(a) Shunt resistance for normalized irradiance range 0.65-0.75

(b) Shunt resistance for normalized irradiance range 0.75-0.85

(c) Shunt resistance for normalized irradiance range 0.85-0.95

(d) Shunt resistance for normalized irradiance range 0.95-1.05

(e) Shunt resistance for normalized irradiance range 1.05-1.2666

Figure 2.9: Shunt resistance plots for different normalized irradiance ranges

Table 2.5: Shunt resistance trend lines for normalized irradiance ranges

	Trend line R_{sh} $[\Omega \cdot m^2]$
I_{nor}0.65-0.75	$R_{sh} = -8.478e - 5 \cdot t + 0.148$
I_{nor}0.75-0.85	$R_{sh} = -1.811e - 4 \cdot t + 0.177$
I_{nor}0.85-0.95	$R_{sh} = -1.193e - 4 \cdot t + 0.156$
I_{nor}0.95-1.05	$R_{sh} = -7.504 - 5 \cdot t + 0.138$
I_{nor}1.05-1.27	$R_{sh} = -7.012e - 5 \cdot t + 0.128$

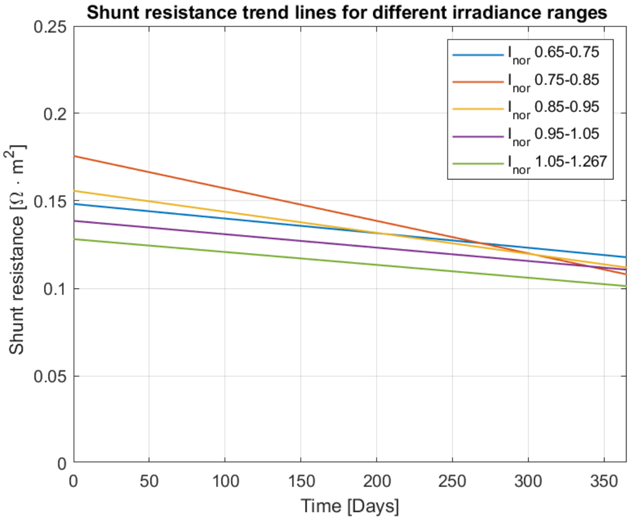

Figure 2.10: Shunt resistance trend line comparison for each irradiance range

2.3.5. Series resistance

For the series resistance, plots are made for the same normalized irradiance ranges and these are shown in Figure 2.11. From Table 2.6 and Figure 2.12 it is evident that the shunt resistance is decreasing over time. In subsection 2.1.1, this parameter was explained and in an ideal case, this resistance is 0, but this will not be the case and a low as possible value is desired. The series resistance is determined by the material en the interconnection and in Table 2.6 it is evident that the R_s increases/decreases slightly over time, which is also shown in Figure 2.11.

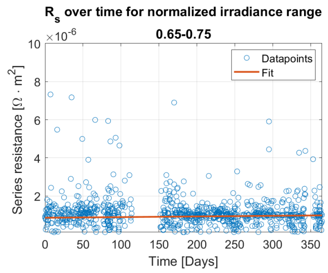

(a) Series resistance for normalized irradiance range 0.65-0.75

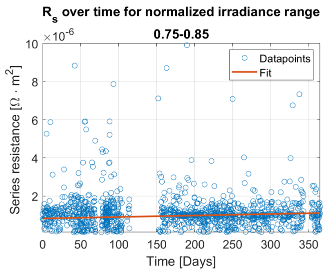

(b) Series resistance for normalized irradiance range 0.75-0.85

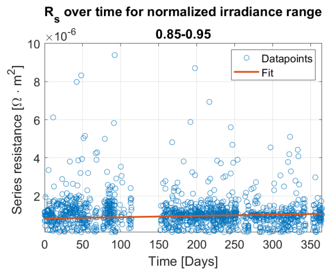

(c) Series resistance for normalized irradiance range 0.85-0.95

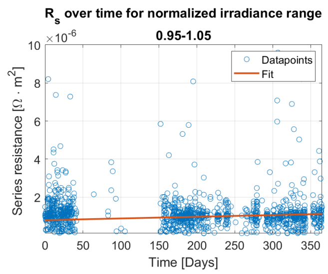

(d) Series resistance for normalized irradiance range 0.95-1.05

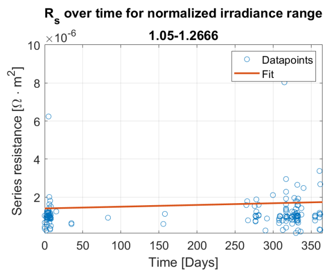

(e) Series resistance for normalized irradiance range 1.05-1.2666

Figure 2.11: Series resistance plots for different normalized irradiance ranges

Table 2.6: Series resistance trend lines for normalized irradiance ranges

	Trend line R_s $[\Omega \cdot m^2]$
I_{nor}0.65-0.75	$R_s = 3.345e - 10 \cdot t + 8.593e - 7$
I_{nor}0.75-0.85	$R_s = 5.917e - 10 \cdot t + 8.598e - 7$
I_{nor}0.85-0.95	$R_s = 6.799e - 10 \cdot t + 8.196e - 7$
I_{nor}0.95-1.05	$R_s = 8.716e - 10 \cdot t + 7.932e - 7$
I_{nor}1.05-1.27	$R_s = 9.439e - 10 \cdot t + 1.367e - 6$

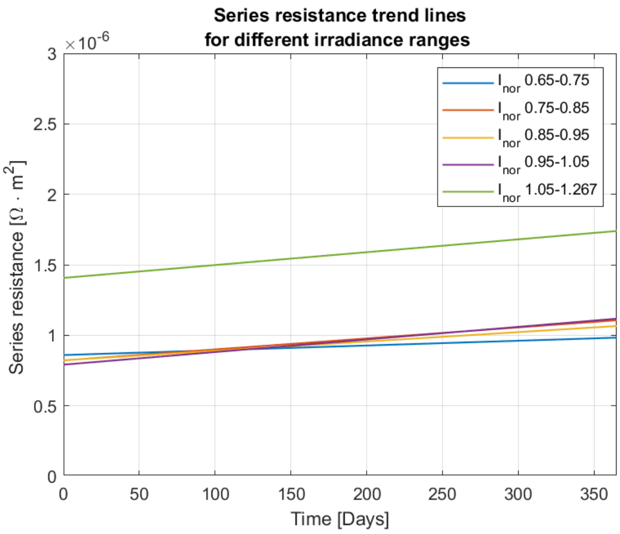

Figure 2.12: Series resistance trend line comparison for each irradiance range

2.4. Validation of method

In this section, the validation of the method is discussed and this is done in three steps and in Figure 2.13, these steps are shown in a schematic overview. First, the validation between the measured data and the fitting parameters is discussed. Then, the validation between the fitting parameters and the trend line through these fitting parameters is shown and lastly, the validation between the measured data and the trend line is shown. For all these steps, the percentage difference is shown in a box plot diagram together with four plots to demonstrate the difference in IV-curve together with the values of the P_{MPP}, FF and V_{oc}. At four dates IV-curves are plotted.

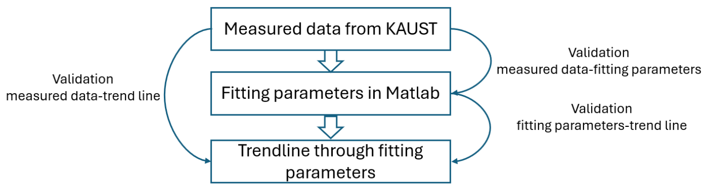

Figure 2.13: Validation scheme of the taken validation steps

2.4.1. Validation between measured data and fitting parameters

In the first part of the validation of the method, the measured data provided by KAUST is compared to the parameter fitting that has been done using a numerical method, which was explained in Subsection 2.1.3.

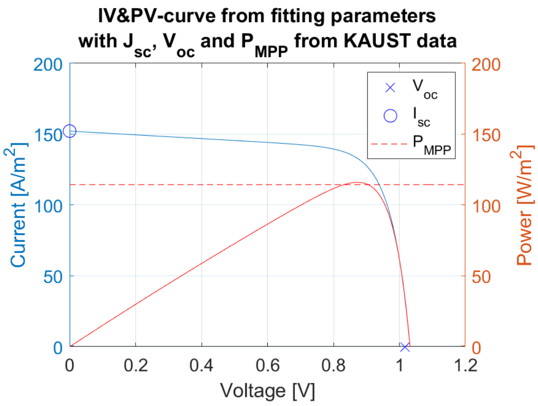

(a) IV & PV-curve from fitting parameters and J_{sc} V_{oc} & P_{MPP} from KAUST data for data point number 1

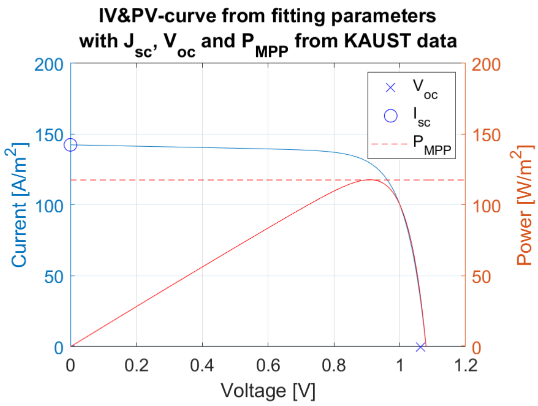

(b) IV & PV-curve from fitting parameters and J_{sc} V_{oc} & P_{MPP} from KAUST data for data point number 3001

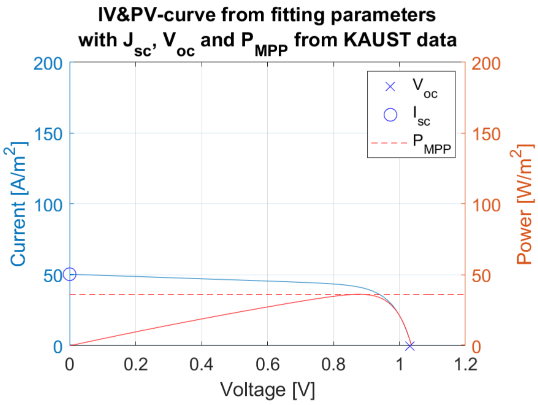

(c) IV & PV-curve from fitting parameters and J_{sc} V_{oc} & P_{MPP} from KAUST data for data point number 6001

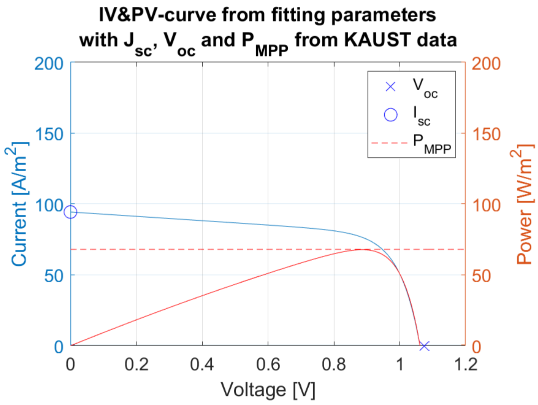

(d) IV & PV-curve from fitting parameters and J_{sc} V_{oc} & P_{MPP} from KAUST data for data point number 9001

Figure 2.14: IV & PV-curve from fitting parameters and J_{sc} V_{oc} & P_{MPP} from KAUST data at 4 different dates

In Figure 2.17a, four plots are shown at various dates and in Table 2.7, the values for the FF, P_{MPP} and V_{oc} are shown and in Equation 2.6, the formulated error was dependent on these variables. These values, which depend on n, J_0, R_{sh}, R_s and J_{ph}, closely match the provided data values.

Table 2.7: Comparison of the fitting parameters and the given data points from KAUST

	$FF_{\text{fit}}[-]$	$FF_{\text{data}}[-]$	$P_{\text{fit}}[W/m^2]$	$P_{\text{data}}[W/m^2]$	$V_{\text{fit}}[V]$	$V_{\text{data}}[V]$
15-Apr-2021	0.739	0.740	116.032	114.374	1.032	1.016
10-Jul-2021	0.766	0.777	117.884	117.687	1.080	1.062
26-Nov-2021	0.694	0.695	36.310	36.160	1.037	1.031
16-Mar-2022	0.677	0.670	67.792	68.007	1.062	1.075

To make an analysis of all the data points, a box plot was made to see what the spread is of the percentage difference between the IV-curve determined by the fitting parameters and the one from the provided KAUST data. In Figure 2.15 this box plot is shown and it can be seen that the normalized maximum power output values are all around one, which means that these values for the fitting and the data are almost equal. The V_{oc} and FF are a bit more of for some of the calculations. If the V_{oc} is overestimated, it makes sense that the FF decreases according to the following equation:

$$FF = \frac{V_{MPP} \cdot I_{MPP}}{V_{oc} \cdot I_{sc}} \tag{2.10}$$

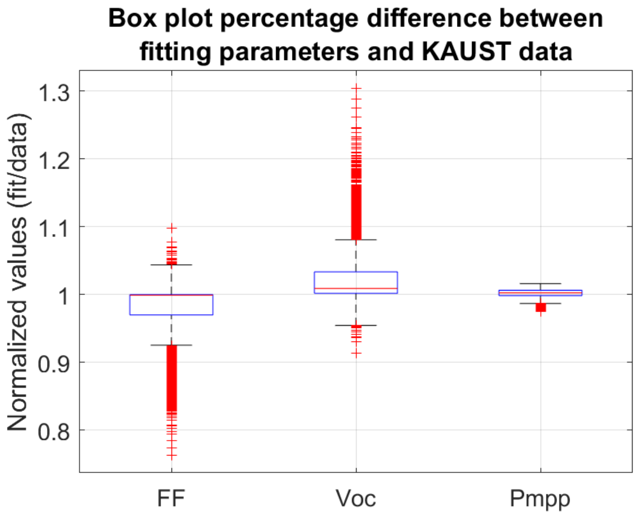

Figure 2.15: Box plot for normalized FF, V_{oc} and P_{MPP} fit/data values

In Appendix B.1, more details on the spread is shown.

2.4.2. Validation between fitting parameters and trend line

In the second part of the validation of the method, the parameter fitting is compared to the trend line that has been plotted through the parameter fitting. For every point, the time with respect to the start of the measurements is taken and this value is used to determine the value for n, J_0, R_sh and R_s, so every value of each electrical parameter is based on the trend lines, obtained in Section 2.3.

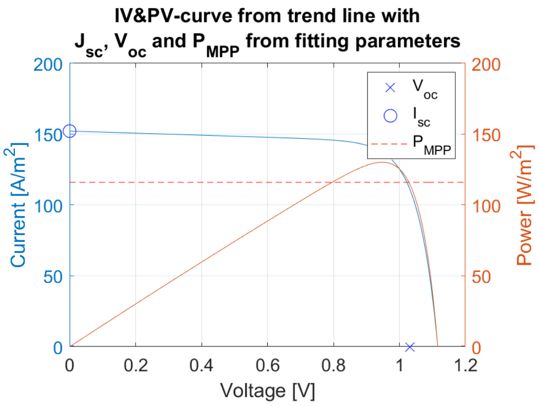

(a) IV & PV-curve from trend line and J_{sc} V_{oc} & P_{MPP} from fitting parameters at point number 1

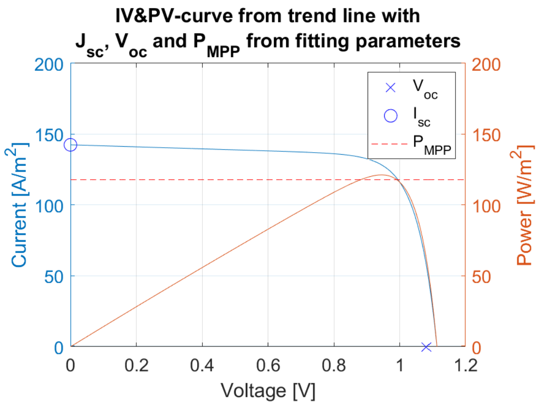

(b) IV & PV-curve from trend line and J_{sc} V_{oc} & P_{MPP} from fitting parameters at point number 3001

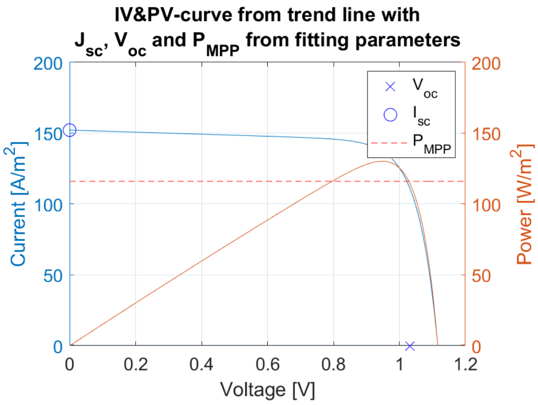

(c) IV & PV-curve from trend line and J_{sc} V_{oc} & P_{MPP} from fitting parameters at point number 6001

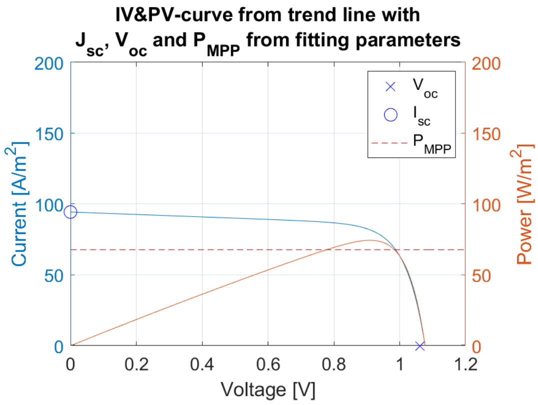

(d) IV & PV-curve from trend line and J_{sc} V_{oc} & P_{MPP} from fitting parameters at point number 9001

Figure 2.16: IV & PV-curve from trend lines and J_{sc} V_{oc} & P_{MPP} from fitting parameters at four different dates

In Figure 2.16, four plots are shown at various dates and in Table 2.7, the values for the FF, P_{MPP} and V_{oc} are shown and in Equation 2.6. The calculated values, which are dependent on n, J_0, R_{sh}, R_s and J_{ph}, are less close compared to the first validation step, but this makes sense, since the trend line through the parameter fitting is used to determine IV-curves.

Table 2.8: Comparison of the trend line and the fitting parameters

	$FF_{\text{trend line}}[-]$	$FF_{\text{fit}}[-]$	$P_{\text{trend line}}[W/m^2]$	$P_{\text{fit}}[W/m^2]$	$V_{\text{trend line}}[V]$	$V_{\text{fit}}[V]$
15-Apr-2021	0.766	0.739	130.194	116.032	1.116	1.032
10-Jul-2021	0.765	0.766	121.256	117.884	1.113	1.080
26-Nov-2021	0.687	0.694	36.203	36.310	1.044	1.037
16-Mar-2022	0.732	0.677	74.424	67.792	1.077	1.062

In Figure 2.19, an IV-curve comparison is presented. It is evident from Figure 2.17a that the IV-curve is less accurate compared to Figure 2.17c. This discrepancy is expected because the trend line is assumed to be linear, leading to inherent deviations from the fitting parameters.

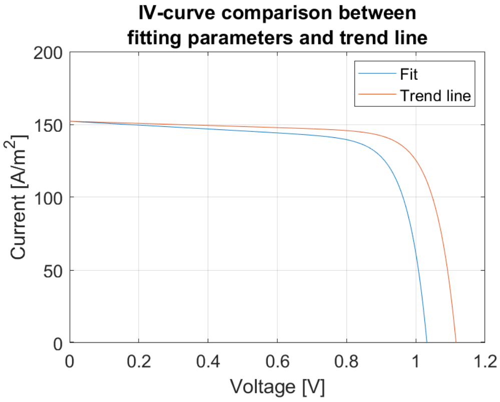

(a) IV-curve based on the parameter fitting and the trend line comparison for data point number 1

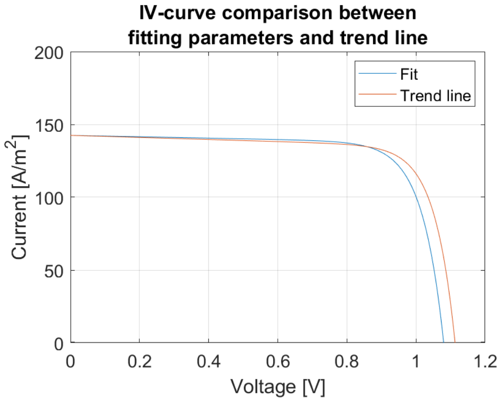

(b) IV-curve based on the parameter fitting and the trend line comparison for data point number 3001

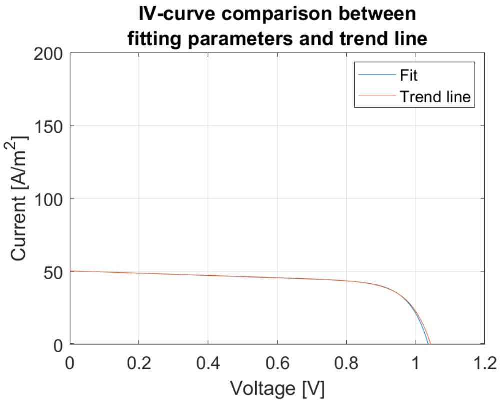

(c) IV-curve based on the parameter fitting and the trend line comparison for data point number 6001

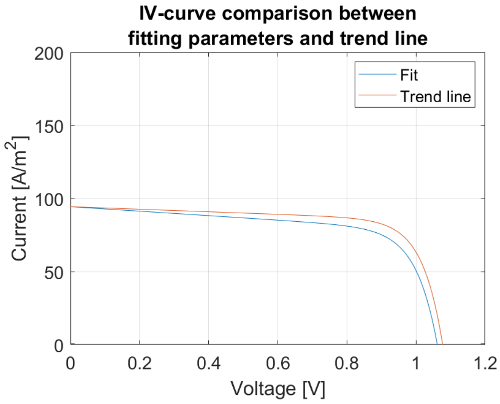

(d) IV-curve based on the parameter fitting and the trend line comparison for data point number 9001

Figure 2.17: IV-curve based on the parameter fitting and the trend line comparison at 4 different dates

To better understand the variations in the FF, V_{oc}, and P_{MPP}, a box plot has been constructed. In Figure 2.18 the box plot is shown, displaying normalized values where each value represents the ratio of the FF, V_{oc}, and P_{MPP} trend line values to their respective fitting parameters. The plot reveals that the normalized fill factor (FF) typically falls within a range of 0.8 to 1.2, indicating a reasonable accuracy. However, the deviations are larger for the open-circuit voltage (V_{oc}) and the maximum power point (P_{MPP}). Outliers for V_{oc} and P_{MPP} are 471 and 602, respectively, comprising roughly 5% of the data points. Additional details about the box plot are provided in Table B.2 in Appendix B. Figure B.2 illustrates the normalized values used to generate the box plot.

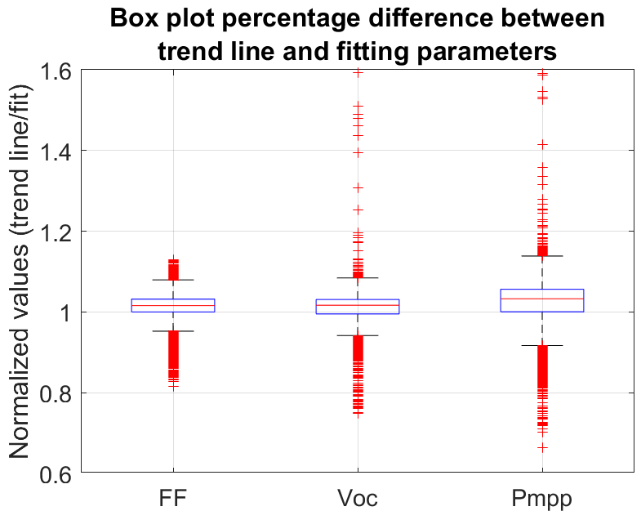

Figure 2.18: Box plot for normalized FF, V_{oc} and P_{MPP} trend line/fit values

2.4.3. Validation between measured data and trend line

In the last part of the validation of the method, the measured data provided by KAUST is compared to the trend line that has been plotted through the parameter fitting. This step of the validation is the combination of step one and step two, which were explained in Subsection 2.4.1 and 2.4.2

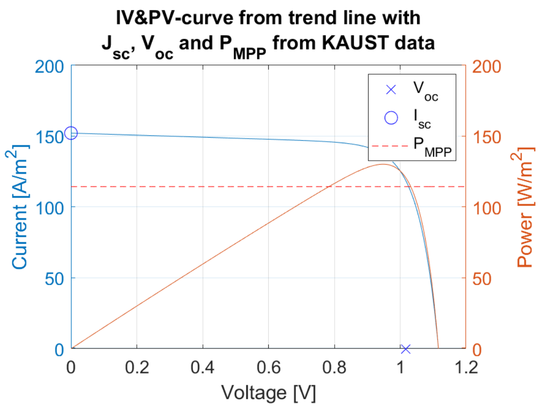

(a) IV & PV-curve from fitting parameters and J_{sc} V_{oc} & P_{MPP} from KAUST data for data point number 1

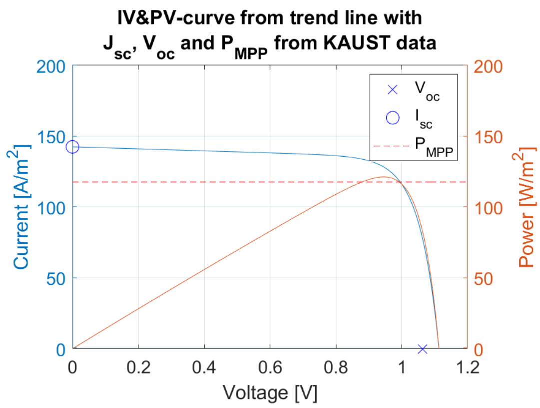

(b) IV & PV-curve from fitting parameters and J_{sc} V_{oc} & P_{MPP} from KAUST data for data point number 3001

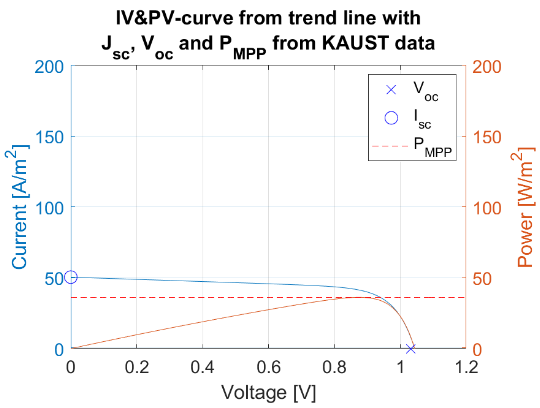

(c) IV & PV-curve from fitting parameters and J_{sc} V_{oc} & P_{MPP} from KAUST data for data point number 6001

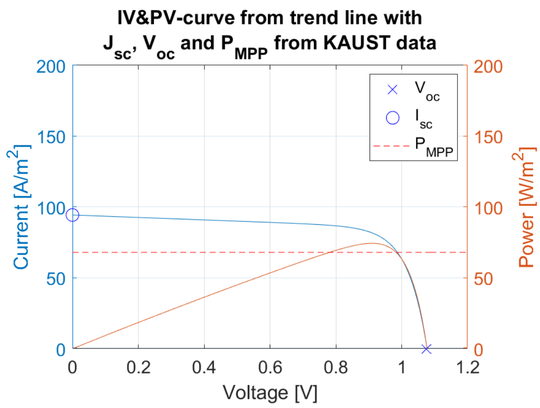

(d) IV & PV-curve from fitting parameters and J_{sc} V_{oc} & P_{MPP} from KAUST data for data point number 9001

Figure 2.19: IV & PV-curve from fitting parameters and J_{sc} V_{oc} & P_{MPP} from KAUST data at 4 different dates

In Figure 2.19, 4 plots are shown at various dates and in Table 2.9, the values for the FF, P_{MPP} and V_{oc} are shown and in Equation 2.6. The calculated values, which are dependent on n, J_0, R_{sh}, R_s and J_{ph}, are less close compared to the first validation step, but this makes sense, since the trend line is less accurate compared to the data, because the trend line is assumed to be linear and therefore causes more deviations.

Table 2.9: Comparison of the trend line and the KAUST data

	$FF_{\text{trend line}}[-]$	$FF_{\text{data}}[-]$	$P_{\text{trend line}}[W/m^2]$	$P_{\text{data}}[W/m^2]$	$V_{\text{trend line}}[V]$	$V_{\text{data}}[V]$
15-Apr-2021	0.766	0.740	130.194	114.374	1.116	1.016
10-Jul-2021	0.765	0.777	121.256	117.687	1.113	1.062
26-Nov-2021	0.687	0.695	36.203	36.160	1.044	1.031
16-Mar-2022	0.732	0.670	74.424	68.007	1.077	1.075

To better understand the variations in the FF, V_{oc}, and P_{MPP}, a box plot has been constructed. In Figure 2.18 the box plot is shown, displaying normalized values where each value represents the ratio of the FF, V_{oc}, and P_{MPP} trend line values to their respective data provied by KAUST. The plot reveals that the fill factor (FF) typically falls within a range of 0.7 to 1.2, indicating a reasonable accuracy. However, the deviations are larger for the maximum power point (P_{MPP}). There are 472 outliers for P_{MPP}, comprising roughly 5% of the data points. Additional details about the box plot are provided in Table B.3 in Appendix B. Figure B.3 illustrates the normalized values used to generate the box plot.

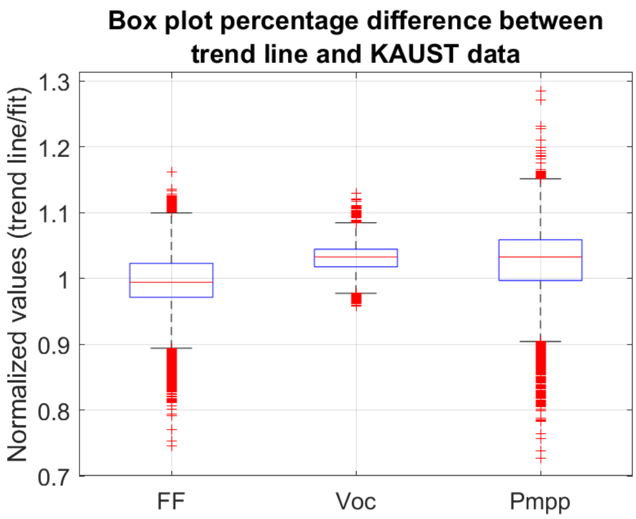

Figure 2.20: Box plot of percentage difference between trend lina and KAUST data

2.5. IV-curve comparison after one year for perovskite top cell

In Figure 2.21, IV-curves are plotted with all the values from the 5-Parameter model based on the linear trend lines. This has been done by taking the value of each parameter at day 1 and the value at day 365. The IV-curves becomes less ideal and the power output decreases over time. To get an idea of the power output decrease, P_{MPP} is given in Table 2.10. This power output is only for the perovskite top cell and the crystalline-silicon bottom cell is not included in this IV-curve. At day 1 and day 365, all lines start at 182 and 168 mA/cm^2, respectively. These values are based on the values provided by KAUST at the start and at the end of testing.

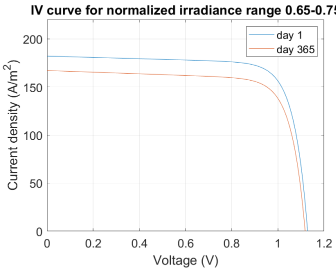

(a) IV-curve at day 1 compared to day 365 for normalized irradiance range 0.65-0.75

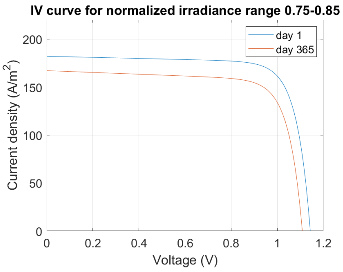

(b) IV-curve at day 1 compared to day 365 for normalized irradiance range 0.75-0.85

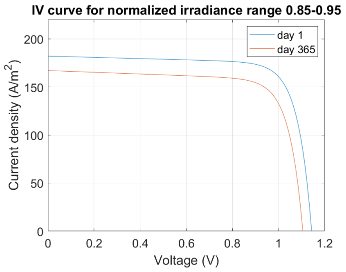

(c) IV-curve at day 1 compared to day 365 for normalized irradiance range 0.85-0.95

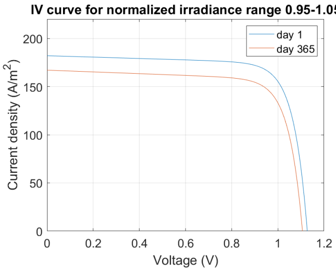

(d) IV-curve at day 1 compared to day 365 for normalized irradiance range 0.95-1.05

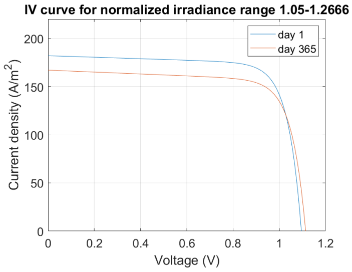

(e) IV-curve at day 1 compared to day 365 for normalized irradiance range 1.05-1.27

Figure 2.21: IV-curve at day 1 compared to day 365 for different normalized irradiance ranges

Table 2.10: Maximum power point at day 1 compared to day 365

	P_{MPP} Day 1 $[W/m^2]$	P_{MPP} Day 365 $[W/m^2]$	Percentage power drop [%]
I_{nor} 0.65-0.75	159.39	143.83	9.87
I_{nor} 0.75-0.85	163.19	140.60	13.84
I_{nor} 0.85-0.95	162.20	140.61	13.31
I_{nor} 0.95-1.05	158.87	140.90	11.31
I_{nor} 1.05-1.267	155.68	141.23	9.28

2.6. Conclusion

In this chapter, the electrical parameters from the single diode equation were determined, fulfilling the first sub-goal described in Section 1.6. For this purpose, measurements of the external parameters were used together with a numerical method discussed in Section 2.1. For every data point, J_0, n, R_{sh} and R_s were determined using this numerical method. Through these fitting parameters, a trend line was fitted to estimate the change in electrical parameters over time. In Section 2.5, this change in electrical parameters over time was used to plot the change in maximum power output of the degraded perovskite top cell. It was shown that the maximum power drops with approximately 10-15% over one year for the cell that has been tested in Saudi Arabia. In Section 2.4, the provided data by KAUST was compared to the values of the fitting parameters and the trend lines. The approximated fill factor, open circuit voltage and maximum power point, compared to the given values, are quite accurate, which was shown in four plots together with the numerical values for each plot.

In this chapter, the electrical parameters of the degraded perovskite solar cell and the degradation rate were found. Now that the change in parameters that determine the IV-curve over time are known, the following step is to perform simulations to find the power output of the degraded perovskite top cell. Therefore, the trend lines through the fitting parameters from this chapter are used.

3 Lifetime energy yield simulations of tandem modules

The second sub-goal of this thesis, described in Section 1.6, is to perform lifetime energy yield simulations with degradation included. For this purpose, a tandem module with different perovskite degradation rates is compared to a single-junction module. The degradation parameters derived from the 5-Parameter model in Chapter 2 are utilized to compare the lifetime energy yield of a tandem module against that of a single-junction module. For this analysis, the PVMD toolbox, previously detailed in Section 1.4, is employed.

In Section 3.1, the methodology for conducting the lifetime energy yield simulations is discussed. Then, in Section 3.2 a comparative analysis of the lifetime energy yields across different degradation rates is presented with values derived from the 5-Parameter model. In Section 3.3, the energy yields of 2T and 4T tandem configurations are compared under identical conditions. In Section 3.4, the comparison of lifetime energy yields at different geographical locations is discussed. Finally, Section 3.5 provides the concluding remarks for this chapter.

3.1. Method and assumptions for life time energy simulations

For the lifetime energy simulations assumptions are made under the same conditions. In this section, these assumptions together with the simulated conditions are discussed.

3.1.1. Method for estimating lifetime energy output

The trend of the parameters obtained from the electrical model in Chapter 2 are employed to estimate the total energy output of a tandem module. This output is then compared to that of a single-junction module, where the tandem cell's bottom cell is the same as the single-junction cell. Both utilize the same design to optimize the conversion of sunlight to electricity, where the design is referred to as 'optics'. The PVMD Toolbox is utilized for these simulations, with parameters adjusted monthly, based on the linear trend lines over time of the parameters of the single diode equation, derived in Chapter 2. Because of a high perovskite degradation rate, these simulations cover a time span of 10 years.

The parameter adjustments are expressed as percentage differences between day 1 and the number of days elapsed in the simulation. Each month, a new simulation is conducted where the variations in parameters n, J_0, R_{sh}, R_s, and J_{sc} are adjusted. These monthly simulations enable a comparative analysis of the energy yields between the tandem and single-junction cells. The percentage differences for each parameter are detailed in the following equations:

$$n_{\text{degraded}} = \left(\frac{\frac{\Delta n}{\Delta t} \cdot t}{n_{\text{trend line}}(0)} + 1 \right) \cdot n_{toolbox} \tag{3.1}$$

$$J_{0,\text{degraded}} = 10 \,\hat{}\left(\left(\frac{\frac{\Delta \log(J_0)}{\Delta t} \cdot t}{\log(J_{0,\text{trend line}}(0))} + 1 \right) \cdot \log(J_{0,toolbox}) \right) \tag{3.2}$$

$$R_{\text{sh,degraded}} = \left(\frac{\frac{\Delta R_{\text{sh}}}{\Delta t} \cdot t}{R_{\text{sh,trend line}}(0)} + 1 \right) \cdot R_{sh,toolbox} \tag{3.3}$$

$$R_{\text{s,degraded}} = \left(\frac{\frac{\Delta R_{s}}{\Delta t} \cdot t}{R_{s,\text{trend line}}(0)} + 1 \right) \cdot R_{s,toolbox} \tag{3.4}$$

$$J_{\text{ph,degraded}} = \left(\frac{\frac{\Delta J_{ph}}{\Delta t} \cdot t}{J_{ph,\text{trend line}}(0)} + 1 \right) \cdot J_{ph,toolbox} \tag{3.5}$$

In all these equations, $\Delta x/\Delta t$ is the slope of the linear trend lines obtained in Section 2.3, where x indicates n, J_0, R_{sh}, R_s or J_{ph}. At t=0, $x_{trendline}(0)$ is determined for parameter x, which is used to determine the percentage change over time. This percentage change is used to adapt the electrical parameters in the PVMD Toolbox, where $x_{toolbox}$ is the initial value in the toolbox. These adjusted parameters are denoted as $x_{degraded}$.

The trend line of the saturation current is linear in a semi-logarithmic plot and to account for that, Equation 3.2 specifies that the change in saturation current is defined by its exponent. For instance, percentage change of 0.5 implies that a saturation current of $10^{-5}\ mA/cm^2$ is applied when the initial value is $10^{-10}\ mA/cm^2$. For other parameters, the adjustment is simply the ratio of the two values multiplied by the toolbox value.

The PVMD toolbox is utilized to carry out the modeling for the cell, module, weather, thermal, and electrical components. In the electrical part the parameters of the 5-Parameter model are determined on a monthly basis, as well as the STC parameters for both the top and bottom cells. These parameters are used to generate an IV-curve at the start of each year, from which the degradation rate is determined.

3.1.2. Tandem module degradation scenarios

This chapter examines five different scenarios, distinguished by the parameter changes identified in Chapter 2 for five normalized irradiance ranges. These scenarios are labeled as scenario 1, 2, 3, 4, and 5, corresponding to the normalized irradiance ranges of 0.65-0.75 for scenario 1, 0.75-0.85 for scenario 2, and so forth. In the previous chapter, Tables 2.3, 2.4, 2.5 and 2.6, provide the trend lines of the electrical parameters for these specific irradiance ranges.

3.1.3. PVMD Toolbox modelling constants

As discussed in Section 1.4, the PVMD toolbox contains various simulation components, each utilizing specific assumptions and constants to ensure accurate modeling. In this section, the constants and assumptions underlying all five modeling components are detailed.

Cell

For the optical modeling of the sub cells, GenPro4 is used. With this program the absorption, transmission and reflection are calculated for each layer with the given layer thicknesses and refractive indexes $(n(\lambda) + i \cdot k(\lambda))$. This software serves as the foundation of the PVMD toolbox. [35]

Module

A module with periodic properties is used, meaning that the module is in an infinite grid where the edge effects are neglected and shading/reflection are simulated as if the module is always surrounded by others. Backward ray tracing is performed to calculate the sensitivity map of the incoming rays. The cell sensitivity is modelled individually, meaning that the incoming rays are calculated separately for each cell. [53] The module has 12 rows and 6 columns of cells. The tilt angle is 31 degrees (Used for Delft, this will be changed in Section 3.4 at different locations). A fixed value of 0.2 is used to represent the reflective properties of the ground.

Weather

In the first simulation, Delft is used as the location and later in Section 3.4 this is changed. The horizon is not included in this simulation and SBdarts [40] is used for weather-related simulations, where the difference between diffused and direct light is modelled.

Thermal

In the thermal part, which is based on Fuentes's model [54], a normal solar cell is used for thermal simulations. The fluid dynamic model is applied to account for the thermal behavior of the cells.

Electrical

The last step is the electrical part, which is based on ASA [36], the following PVMD inputs are used: Each cell is modeled individually and the cells are not reconfigurable. Metalization losses are ignored to simplify the calculations in this part and 3 bypass diodes are used. Initially, a 2T configuration is used, which is changed to a 4T configuration in Section 3.3.

3.1.4. General assumptions for simulations

In Chapter 2, linear trend lines for the electrical parameters n, R_{sh}, R_s, and J_0 were established over time. These trend lines are employed to change the parameters of the perovskite top cell within the PVMD toolbox simulations. Due to the rapid change in shunt resistance over time, it is assumed that its maximum percentage deviation from the initial value is 85%, implying that it can drop to only 15% of its initial value. The rate of change for the other parameters is determined by the linear trends identified in the preceding chapter.

For the single-junction cell and the bottom cell of the tandem it is assumed that there is no degradation included. This assumption leads to a constant annual energy yield for the single-junction module each year. Next to the assumption that there is no degradation included, the weather pattern is kept the same for each year to ensure that variations in energy yield are not influenced by differences in yearly weather conditions.

When comparing the 2T and 4T configurations, the cell structure remains unchanged, and the only difference is that a tandem IV-curve can be plotted for the 2T configuration, but for the 4T configuration this cannot be done, resulting in two separate IV-curves for both top and bottom cell, which is explained in Section 3.3.

Everything in this chapter is based on high degradation rates obtained from KAUST data and this might not be representative for all perovskite solar cells. This chapter is used to analyse the energy yield of an existing model of a tandem cell, already implemented in the PVMD Toolbox, considering this high degradation rate. The simulations can also be performed, using the PVMD Toolbox, by applying other degradation rates obtained from a more recent data set.

3.1.5. Used solar cells for simulations

In this subsection, the solar cell configuration utilized in the PVMD toolbox is discussed. The used tandem cell features a monolithic crystalline-silicon/perovskite structure with an efficiency of 32.5% [55]. This tandem setup consists of a silicon heterojunction bottom cell paired with a perovskite top cell with an 1.68 eV bandgap. In Figure 3.1, the schematic stack of the utilized tandem solar cell is shown.

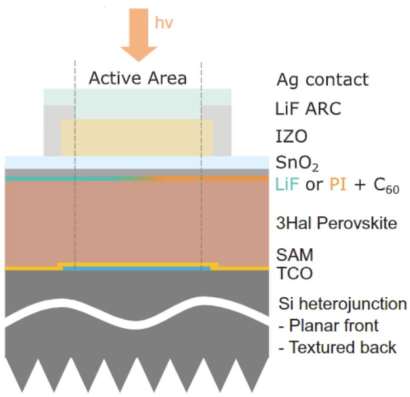

Figure 3.1: Schematic stack of c-Si/pvk tandem solar cell used for the lifetime energy yield simulations [55]

Remarkably, this configuration retained 95% of its initial power conversion efficiency (PCE) after 300 hours of maximum power point tracking in ambient conditions.

In terms of performance, the tandem cell achieved a PCE of 32.5%, accompanied by an open-circuit voltage of 1.98 V, a fill factor of 81.18%, and a short-circuit current density of 20.24 mA/cm^2. [55] For a comparison between the single-junction module and the tandem module, the silicon heterojunction bottom cell of this tandem configuration is utilized.

In Figure 3.2, the IV-curve of a single-junction cell and a tandem cell are illustrated. The tandem configuration exhibits approximately half the current but roughly 2.5 times higher voltage compared to the single cell, resulting in a higher initial power output without degradation, as expected. The initial efficiencies, based on the STC determined in the PVMD Toolbox, for the tandem and single-junction cells are 31.1% and 23.9%, respectively.

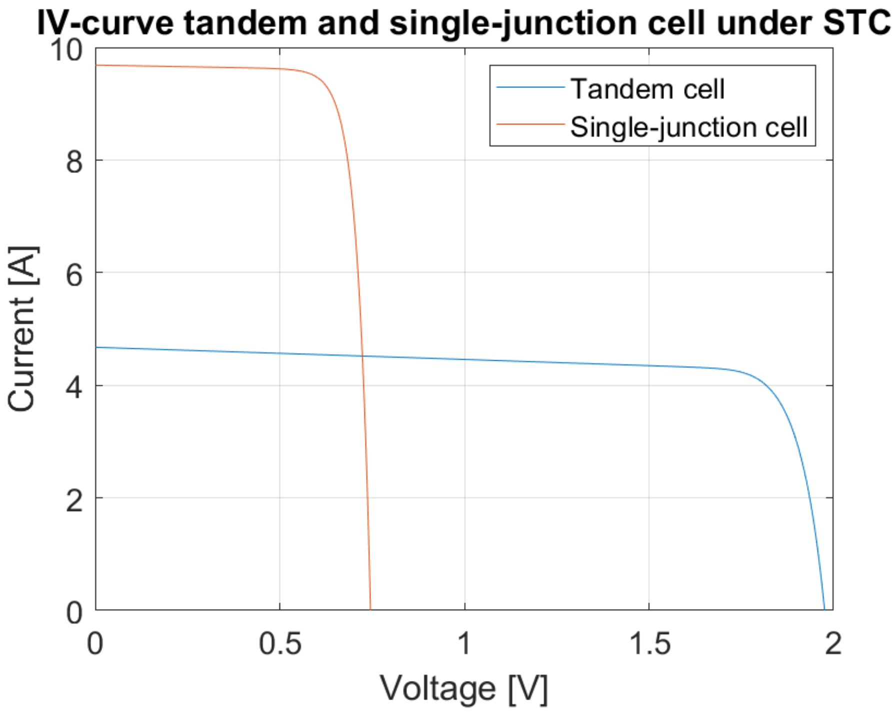

Figure 3.2: IV-curve tandem and single-junction solar cell comparison under STC

3.2. Lifetime energy yield for different degradation scenarios

In this section, the parameters derived from the 5-Parameter model, as discussed in Chapter 2, are used to perform lifetime energy yield simulations. This is done by using five scenarios, which is discussed in Section 3.1.2. For this comparison 10 years are considered, because the total energy yield at the tenth year is significantly reduced and the power output is nearly 0.

In Figure 3.3, six IV-curves are shown and each represents an IV-curve that is made at the start of a year. Here, two individual IV-curves for the sub cells are plotted together with the tandem cell. It is evident that the IV-curve of both the perovskite top cell and the tandem cell contain a large slope towards the y-axis, which is caused by the decreasing shunt resistance, which is ideally infinitely large, as discussed in Subsection 2.1.1. After 10 years, the power at STC for the perovskite top cell decreased from 4.85W to 0.24W, resulting in a low tandem power output. The tandem cell's short circuit current decreased due to the decrease in the perovskite top layer's short circuit current, which is limiting in a 2T configuration.

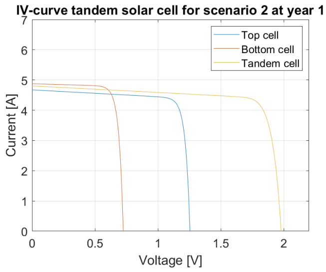

(a) IV-curve at the start of year 1 for scenario 2

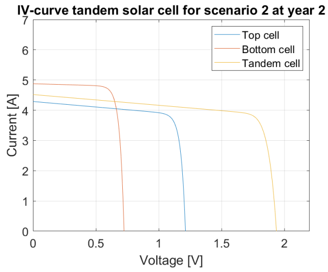

(b) IV-curve at the start of year 2 for scenario 2

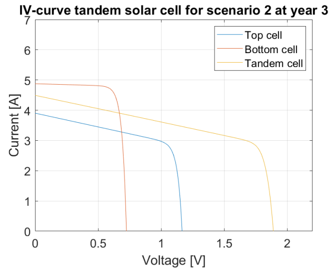

(c) IV-curve at the start of year 3 for scenario 2

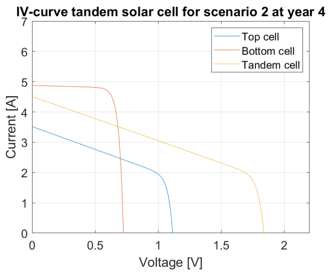

(d) IV-curve at the start of year 4 for scenario 2

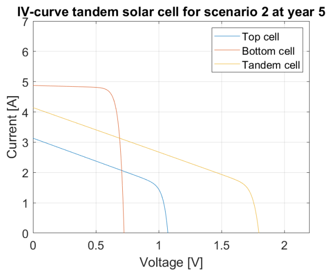

(e) IV-curve at the start of year 5 for scenario 2

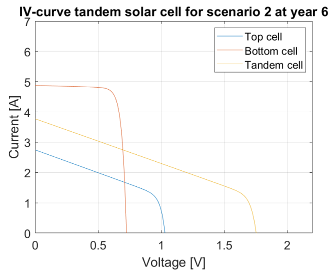

(f) IV-curve at the start of year 6 for scenario 2

Figure 3.3: STC IV-curves for a tandem solar cell together with its top and bottom cell at the start of year 1 up to year 6

In Figure 3.4, , the efficiency over time is shown for the perovskite top cell and the tandem cell. The perovskite top cell's efficiency drops quickly in the first 4 years, but after these 4 years, the efficiency drop becomes more constant over time. The main reason for this quick drop in the beginning is the decreasing shunt resistance, where the maximum value is reached after approximately 4 years, which is discussed in Subsection 3.1.4. The tandem cell and perovskite top cell efficiency decreased to approximately 4% and 1%, respectively, after 10 years.

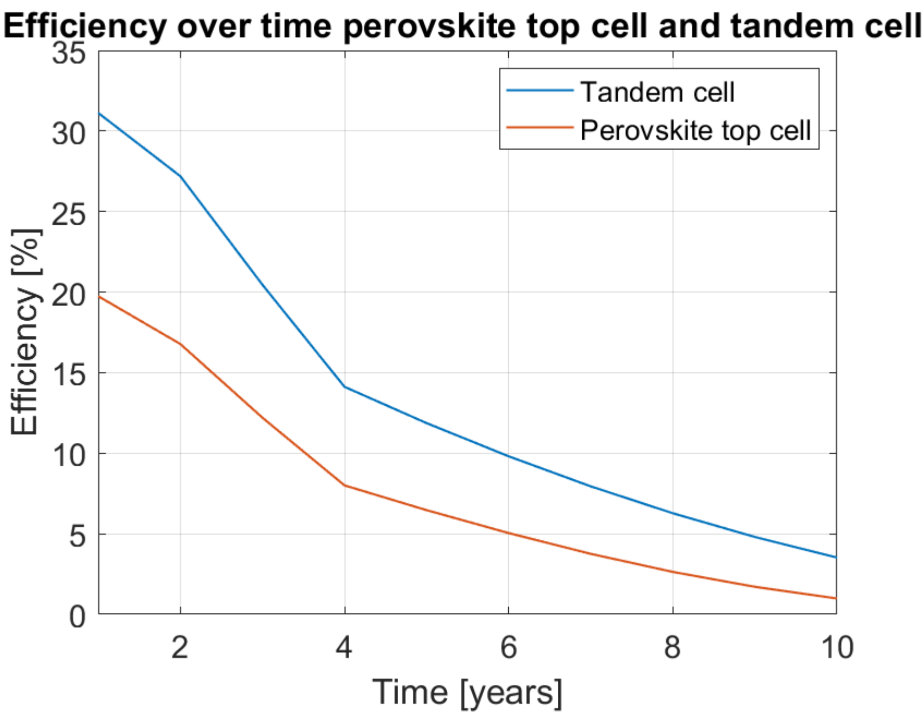

Figure 3.4: Efficiency plot over time for the tandem cell and perovskite top cell in a 2T configuration

In Figure 3.5, the monthly energy yield of the first 5 years of the tandem module is compared to a single-junction module and for all scenarios, where the energy yield of the silicon module is already higher after 2 years applying this degradation rate. By the fourth year, the monthly energy yield becomes the same across all degradation scenarios due to the most limiting factor, which is the shunt resistance. As outlined in Subsection 3.1.4, the shunt resistance is assumed to degrade to a minimum of 15% of its initial value, beyond which the monthly power output stabilizes and remains nearly identical throughout each month.

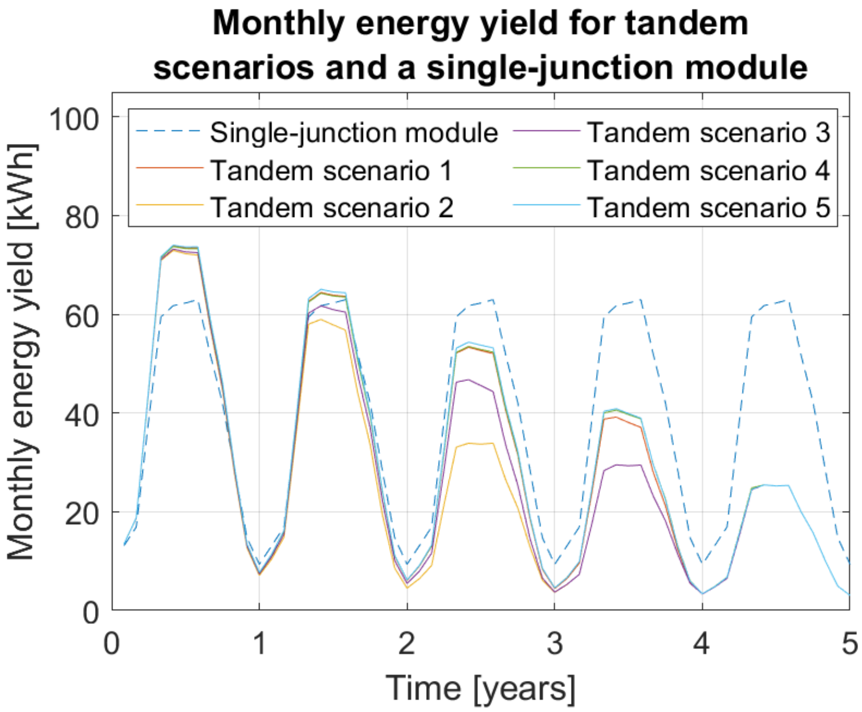

Figure 3.5: Monthly energy output over time for a single-junction module and 2T tandem modules for 5 scenarios

In Figure 3.6, the lifetime energy yield, obtained by integrating the power over time, is depicted for both the degraded tandem module and the single-junction module. It is evident that the single-junction cell surpasses the tandem cell configuration in energy yield after approximately 3 years, given the degradation rate of approximately 27% for the perovskite top cell under STC. Given this degradation rate, even under the assumption that the shunt resistance's decrease is limited to 15% of its initial value, the tandem cell does not come close to achieving the desired energy yield after 25 years. This result is not unexpected because the degradation rate in the first year is approximately 10-15% and these simulations are based on a 10-year extrapolation, where the annual degradation rate increases even more.

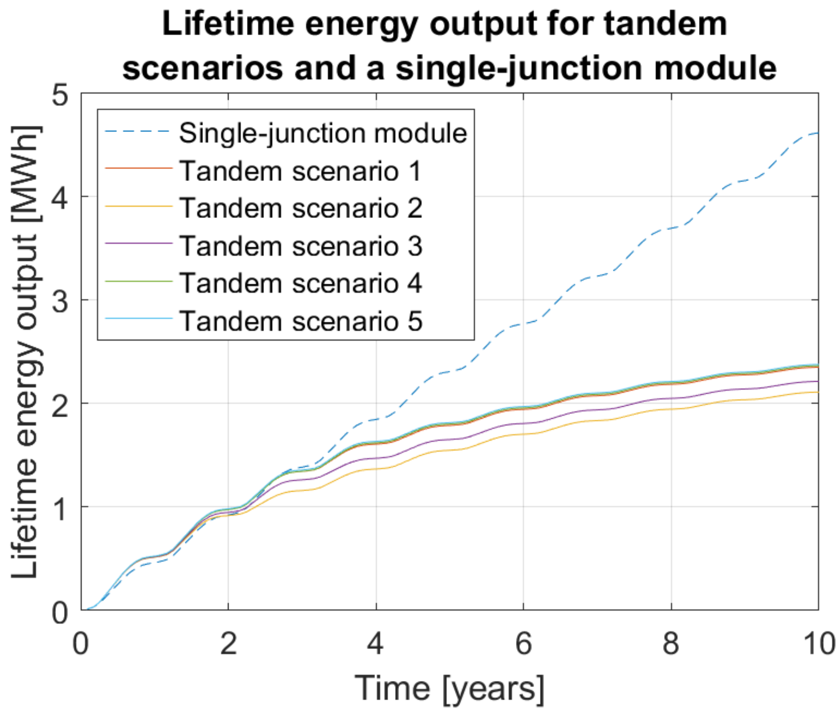

Figure 3.6: Cumulative energy output over time for a 2T tandem and single-junction cell for 5 scenarios

To estimate the degradation rate, an average annual degradation rate is calculated, where this value is based on the power output at STC at the start of each year of the simulation. In Table 3.1, this degradation rate is shown, which is divided into three parts, an average degradation rate for the energy yield of the tandem cell, the average degradation of the perovskite top cell and the average degradation of the perovskite top cell after 4 years. The average degradation rates are closely aligned due to minimal deviations in lifetime energy yield over time, as shown in Figure 3.6 and the monthly energy yield, which is shown in Figure 3.5. The largest degradation rate is used in the second scenario, which is 21.31 %/year and 27.89%/year for the tandem cell and the perovskite top cell after 10 years, respectively. This is remarkably high considering a degradation rate of 0.8%/year for a single-junction module is allowed to maintain a minimum of 80% of the initial power output after 25 years.

The applied average degradation rate of the perovskite top cell in the first 4 years, is lower than the average 10-year degradation rate, primarily due to the impact of the shunt resistance. Initially, the shunt resistance imposes limitations, but subsequently, other factors contribute to a degradation rate exceeding 40% in the final year of the simulation, while the degradation rate in the first year is between 10 and 15%.

Table 3.1: Average degradation rate after 10 years for 5 scenarios for the tandem cell and the individual perovskite top cell

	Average degradation rate for tandem cell [%/year]	Average degradation rate perovskite top cell [%/year]	Average degradation rate perovskite top cell first 4 years [%/year]
Scenario 1	21.07	27.55	21.37
Scenario 2	21.31	27.89	23.98
Scenario 3	21.19	27.76	23.75
Scenario 4	21.19	27.63	19.20
Scenario 5	21.13	27.51	18.67

3.3. Lifetime energy comparison between 2T and 4T configurations

In this section, the lifetime energy yield of a single-junction, a 2T and 4T tandem configuration are compared, using the same optical properties. For this purpose, the obtained parameters from the 5-Parameter model, which was discussed in Chapter 2, are used. The simulations are performed by using the scenarios discussed in Subsection 3.1.2. In Section 3.2, a 2T configuration was used for the lifetime energy simulations over 10 years and in this section, a 4T configuration is compared to the common 2T structure. The main advantage of a 4T structure, compared to a 2T structure, is that the bottom and top cell of a tandem are connected separately, which results in separate power output for both sub cells, where a 2T structure is limited by the lowest short circuit current. Since the perovskite top cell degrades faster and the current mismatch increases over time, a 4T could be beneficial for the lifetime energy yield.

In Figure 3.7, individual IV-curves are shown for both top and bottom cell. In a 4T configuration, these two are connected separately an therefore an IV-curve of a tandem cannot be made. It is evident that the IV-curves deteriorate over time as degradation increases.

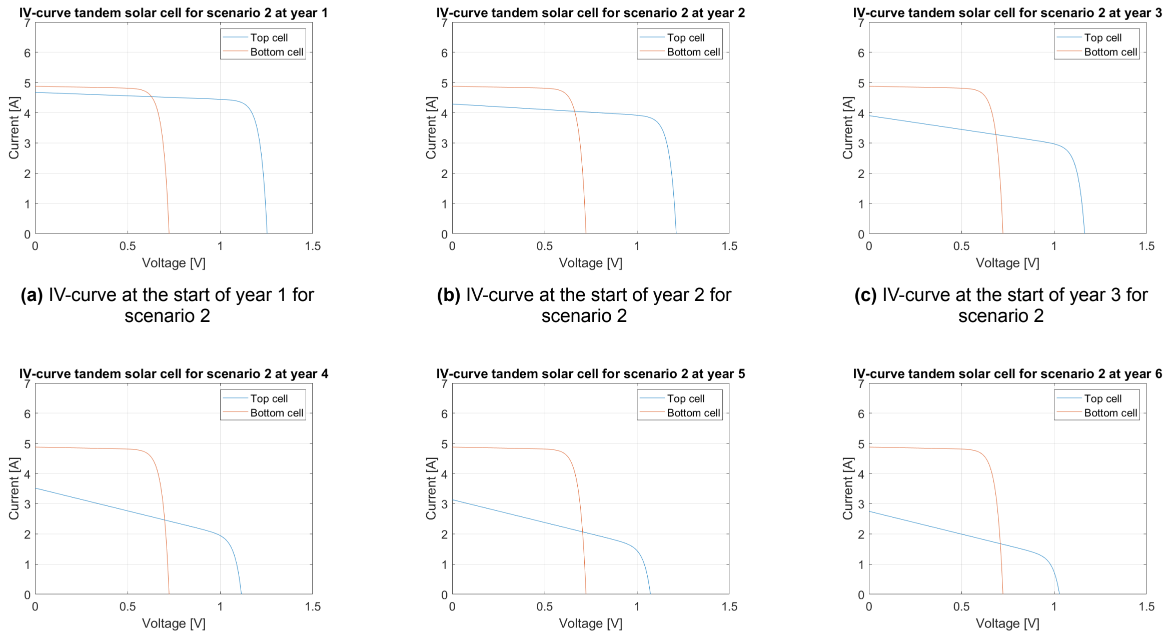

(a) IV-curve at the start of year 1 for scenario 2

(b) IV-curve at the start of year 2 for scenario 2

(c) IV-curve at the start of year 3 for scenario 2

(d) IV-curve at the start of year 4 for scenario 2

(e) IV-curve at the start of year 5 for scenario 2

(f) IV-curve at the start of year 6 for scenario 2

Figure 3.7: STC IV-curves for a 4T tandem solar cell's top and bottom cell at the start of year 1 up to year 6

In Figure 3.8, the efficiency over time is shown for the perovskite top cell together with 2T & 4T tandem cell configurations. The perovskite top cell's efficiency drops quickly in the first 4 years, but after these 4 years, the efficiency drop becomes more constant over time. The main reason for this quick drop in the beginning is the decreasing shunt resistance, where the maximum allowable change is reached after approximately 4 years, which is discussed in Subsection 3.1.4. The 2T tandem cell, 4T tandem cell and perovskite top cell efficiencies drop to approximately 13%, 4% and 1%, respectively, after 10 years. The 4T tandem configuration is less affected by the perovskite degradation rate because of the separate connection in top and bottom cell.

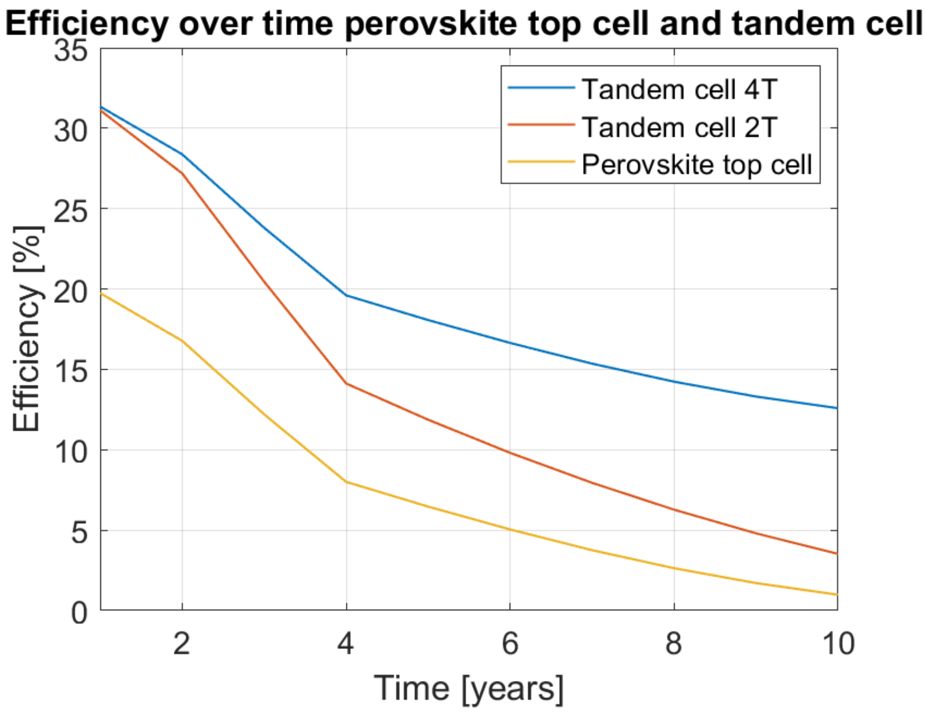

Figure 3.8: Efficiency plot over time for 2T and 4T tandem cell configurations and the perovskite top cell

In Figure 3.9, the monthly energy yield of the 4T tandem module is compared to a single-junction module and for all five scenarios, the energy yield of the silicon cell is already higher after 2 years. In Figure 3.10, a comparison between a single-junction module, a 2T configuration tandem module and a 4T configuration tandem module is shown. As shown in this figure, the monthly energy yield for both tandem modules are almost similar in the first 2 years, but after the degradation increases, the 4T energy yield is higher.

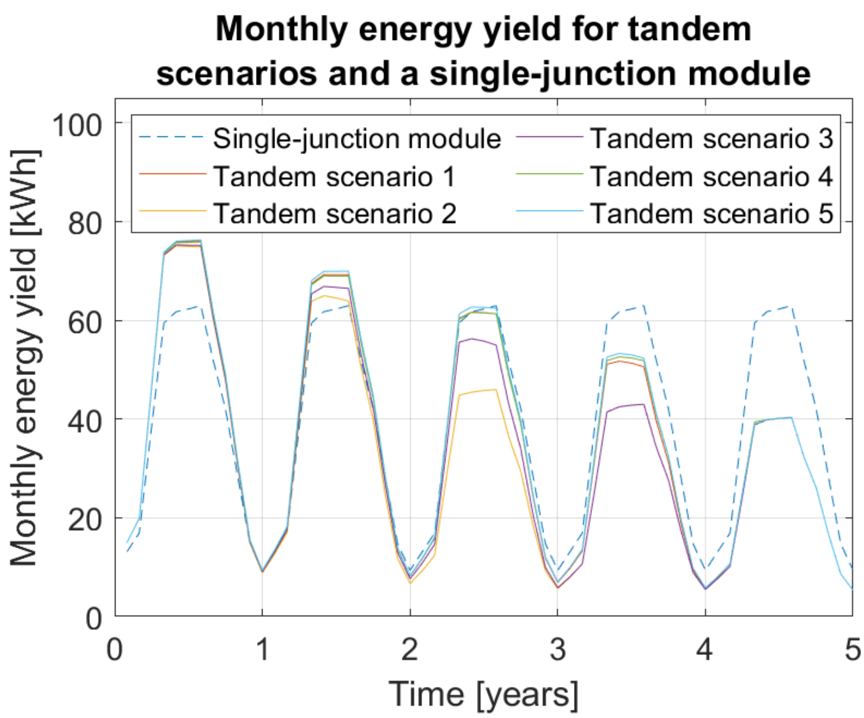

Figure 3.9: Monthly energy output over time for a single-junction module and 4T tandem modules for five scenarios

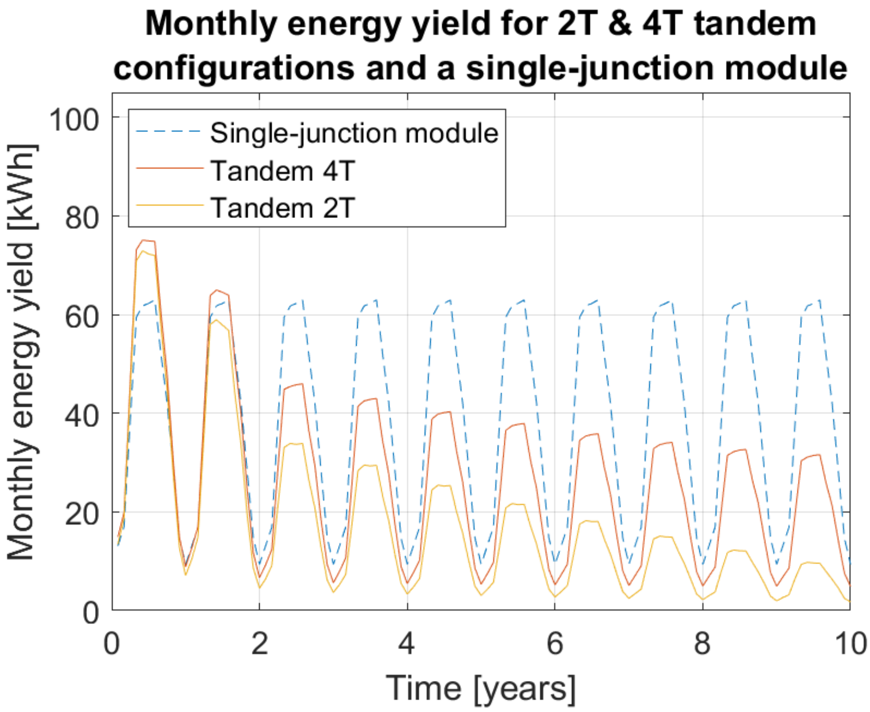

Figure 3.10: Monthly energy output over time for a single-junction module, a 2T tandem module and a 4T tandem modules for scenario two

In Figure 3.11, the lifetime energy yield of the degraded 4T tandem solar cell is illustrated together with the single-junction cell. This figure shows that the single-junction module has a higher energy yield after approximately 4 years compared to the tandem applying this degradation rate, which is approximately 9.5 %/year. Using this degradation rate, the tandem cell is nowhere near the desired energy yield looking at this simulation of 10 years even with the assumption that the shunt resistance's limit is 15% of the initial value.

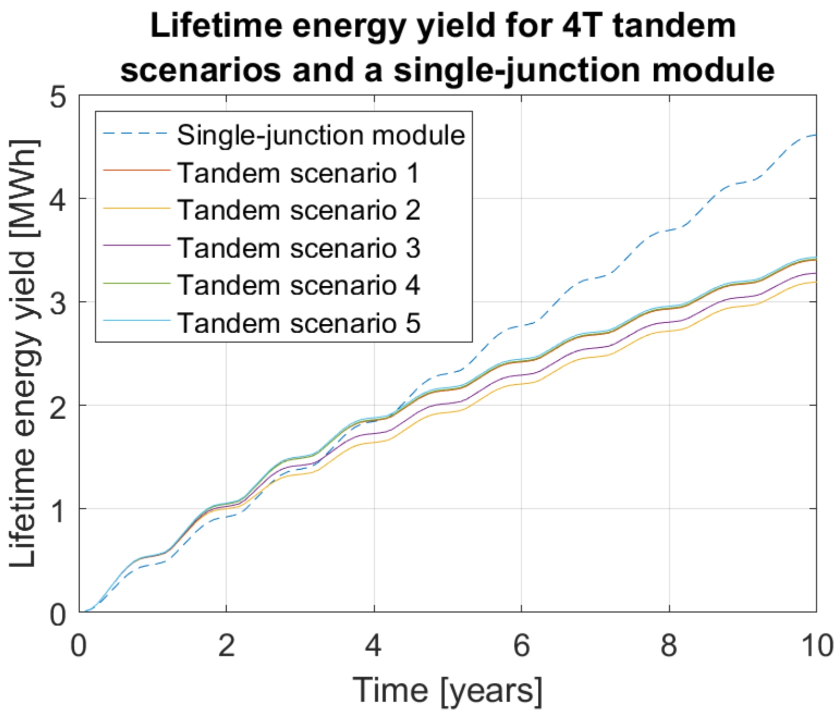

Figure 3.11: Lifetime energy output over time for a single-junction module and 4T tandem modules for 5 scenarios

The comparison of the energy yield between the two different electrical connections, using the degradation rate from the second scenario, is illustrated in Figure 3.12. This figure demonstrates that the lifetime energy yield for the 4T tandem is 44% higher than that of the 2T tandem, indicating a significant increase in energy yield.

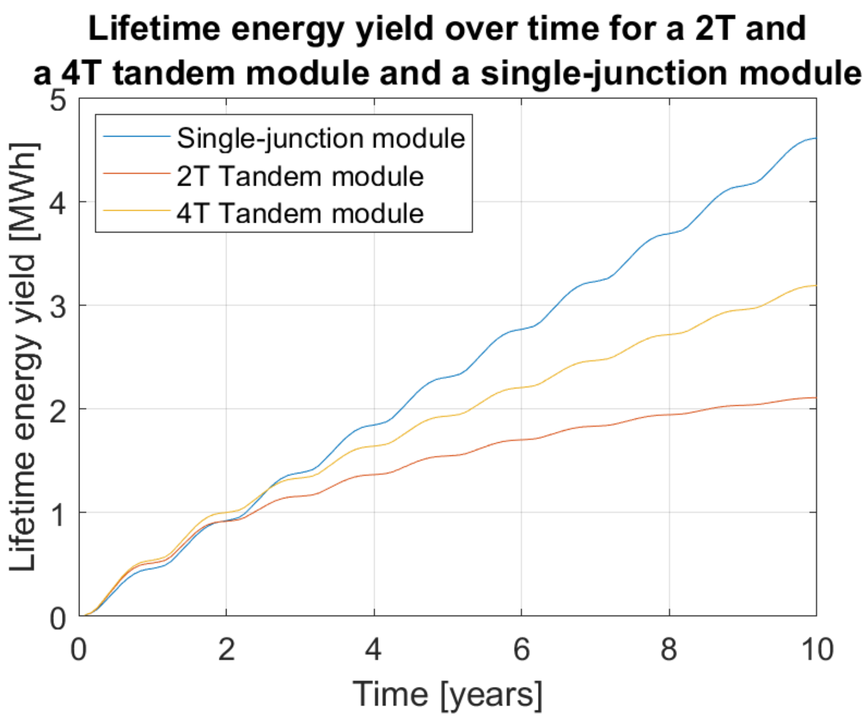

Figure 3.12: Lifetime energy output over time for a single-junction module, a 2T tandem modules and a 4T tandem module scenario 2

To assess the degradation rate, an average annual degradation in energy output is estimated based on the power output at STC at the beginning of each year in the simulation. In Table 3.2, this degradation rate is shown, categorized into three parts: an average degradation rate for the energy output of the 2T tandem cell, the 4T tandem cell and the average degradation of the perovskite top cell. The average degradation rate of the 4T tandem cell is lower compared to the 2T tandem cell, which is not unexpected since the optics of both configurations are identical, and neither sub cell is current limiting. Notably, the 4T configuration allows energy production to continue even when the perovskite cell no longer functions, owing to the separate connection of both sub-cells.

Table 3.2: Average degradation rate after 10 years for 5 scenarios for a 2T and 4T tandem solar module

	Average degradation rate 2T tandem [%/year]	Average degradation rate 4T tandem [%/year]	Average degradation rate perovskite top cell [%/year]
Scenario 1	21.07	9.51	27.55
Scenario 2	21.31	9.55	27.89
Scenario 3	21.19	9.52	27.76
Scenario 4	21.19	9.54	27.63
Scenario 5	21.13	9.53	27.51

3.4. Lifetime energy comparison at different locations

In this section, the lifetime energy is compared at four different locations, which are Delft, Lagos, Lisbon and Shanghai. Each of these locations experiences unique climatic conditions, and the differences in lifetime energy yield are discussed. Since the four locations have different climates, a varying lifetime energy yield is expected. In Table 3.3, the differences in climate are shown, where there are difference between the temperature and irradiation.

	Average Temperature [°C]	Irradiation at optimum tilt [kWh/m^2/year]	Climate
Delft [56, 57]	11	1281	Moderate
Lagos [58, 57]	27	1742	Tropical
Lisbon [59, 57]	17	1979	Warm Mediterranean
Shanghai [60, 57]	17	1407	Humid subtropical

Table 3.3: Climate Data for Delft, Lagos, Lisbon, and Shanghai.

In Table 3.5, the average degradation rate for a 2T and 4T tandem module is shown and this value is determined by the difference in annual energy yield. Notably, the degradation rate for the 2T tandem module is lowest in Delft. This difference may be attributed to the limiting short circuit current of the two sub cells. If the silicon bottom cell limits the current, the perovskite top cell can degrade without significantly affecting power output. However, if the perovskite cell is limiting and it degrades, the energy output differential increases, leading to a higher average degradation rate. Looking at the mismatch between the I_{ph} of the top and bottom cell at each locations, an average current mismatch was calculated using the following equation:

$$\text{Average current mismatch} = \frac{1}{N}\sum_{i=1}^{N}\left(I_{\text{ph,Si}} - I_{\text{ph,pvk}}\right) \tag{3.6}$$

In Table 3.4, the average mismatch of the first 5 years of the simulation is shown. This table shows that the mismatch is the lowest in Delft and the highest in Shanghai.

Table 3.4: Average Iph mismatch

	Average I_{ph} mismatch $[mA/cm^2]$
Delft	0.28
Lagos	0.31
Lisbon	0.42
Shanghai	0.55

Analyzing the average degradation rates in Table 3.5, it is evident that the 2T configuration experiences a higher average degradation rate. This observation aligns with expectations, as a greater average mismatch between sub cells typically leads to increased degradation losses, because the perovskite sub cell is current limiting. In the last column of Table 3.5, the average degradation rate of the perovskite top cell is shown and this value is based on STC, which is determined by the change in electrical parameters, which was discussed in Subsection 3.1.1. Since these values are all based on the second scenario, the average perovskite degradation rate is the same at each location.

Table 3.5: Average degradation rate after 10 years at 4 locations for a 2T tandem solar cell, 4T tandem cell and an individual perovskite top cell

	Average degradation rate for 2T tandem cell [%/year]	Average degradation rate for 4T tandem cell [%/year]	Average degradation rate perovskite top cell [%/year]
Delft	18.95	8.56	27.89
Lagos	19.96	8.98	27.89
Lisbon	20.63	8.95	27.89
Shanghai	21.19	8.75	27.89

In Figure 3.13, the lifetime energy yield over time for a 2T tandem, 4T tandem and single-junction module at different locations is shown. Subfigures 3.13b and 3.13d illustrate that there are minimal yearly fluctuations in the annual energy yield.

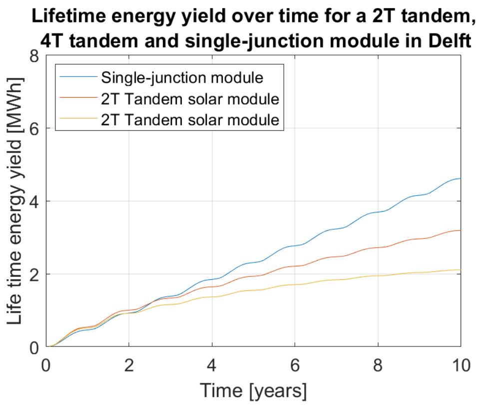

(a) Lifetime energy yield over time for a 2T tandem, 4T tandem module and a single-junction module in Delft

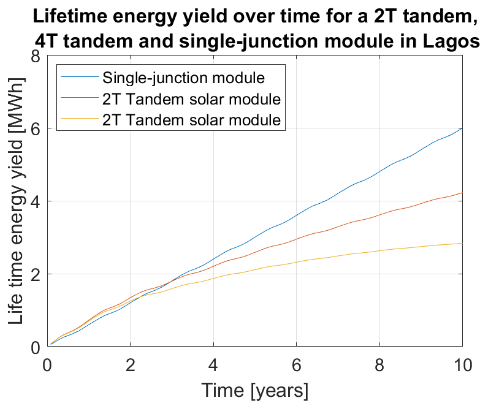

(b) Lifetime energy yield over time for a 2T tandem, 4T tandem module and a single-junction module in Lagos

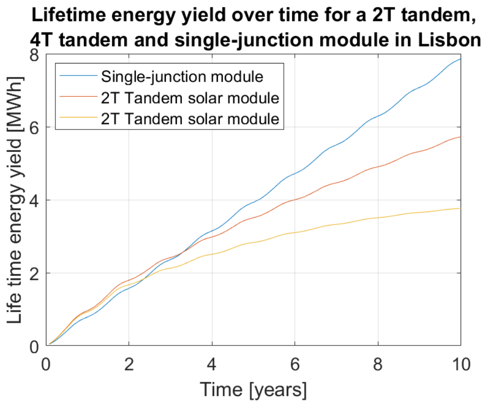

(c) Lifetime energy yield over time for a 2T tandem, 4T tandem module and a single-junction module in Lisbon

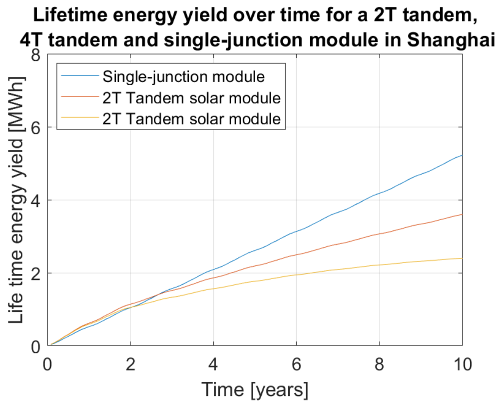

(d) Lifetime energy yield over time for a 2T tandem, 4T tandem and a single-junction module in Shanghai

Figure 3.13: Lifetime energy yield over time for a 2T tandem, 4T tandem and a single-junction module at different locations

3.5. Conclusion

In this chapter, lifetime energy yield simulations when degradation is included were performed, fulfilling the second sub-goal, described in Section 1.6. In this chapter, a conventional single-junction module was compared to a tandem module applying five different degradation rates. These five degradation rates were referred to as scenarios and were based on the irradiance ranges discussed in Chapter 2. In this chapter, the lifetime energy yield after 10 years was shown and even with the assumption that the the R_{sh} has a minimum of 15% of its initial value, the single-junction module produced more energy after approximately three years for each scenario, which is infeasible considering PV module manufacturers must guarantee at least 80% of the initial power output after 25 years. This high degradation rate not unexpected since the energy yield, after one year of testing in Saudi Arabia, decreased with approximately 10-15%, where the electrical parameters were extrapolated over time to perform lifetime energy yield simulations. The average degradation under STC for the tandem cell and the perovskite top cell were shown, which are approximately 21.5%/year and 27.5%/year, respectively. After 10 years, the power output for the perovskite cell decreased from 4.85W to 0.24W, resulting in a low combined tandem power because of the low J_{sc} of the top cell, which is current limiting.

In Section 3.3, the 2T and 4T configurations were compared for five scenarios and the lifetime energy yield was increased with approximately 44% using a 4T tandem cell configuration. Despite a high perovskite degradation rate, the silicon bottom cell was still able to produce power at its own J_{sc} instead of the perovskite top layer to be current limiting, where the power output of the top cell decreased to 0.24W at STC after 10 years.

In Section 3.4, the lifetime energy yield at different locations was compared and average degradation rates were shown. It was shown that the average degradation rates of a 2T tandem cell are in a larger range than the average of a 4T tandem cell. This difference can be caused by the limiting short circuit current, which is the silicon bottom layer more often in Delft and Lagos compared to Lisbon and

Shanghai, where the degradation of the perovskite top cell influences the power output less. Also, the average current mismatch is the highest in Shanghai and the lowest in Delft. The average degradation rate of the 4T tandem cell is closer at all locations, because both sub cells are connected separately.

Although everything in this chapter is based on high degradation rates from KAUST data, which might not be representative for all perovskite solar cells, simulations can be performed using other degradation rates obtained from different data sets, by utilizing the PVMD Toolbox.

It is concluded that the applied degradation rates of all five scenarios are too high for a tandem cell to produce more energy than the compared single-junction cell. The next step is to perform lifetime energy yield simulations with varying degradation rates to find the perovskite degradation rate for which the lifetime energy yield of a tandem is higher compared to a single-junction module.

4

Analyzing lifetime energy yield for different degradation rates

As stated in Section 1.6, the third sub-goal of this thesis is to find the maximum tolerable perovskite degradation rate. In order to have a higher lifetime energy yield after 25 years a tandem module is compared to a single-junction module and different degradation rates are analysed to find the maximum tolerable perovskite degradation rate. The degradation rates applied in Chapter 3 are adjusted and lifetime energy simulations are performed to ascertain the necessary change in degradation rate to achieve a higher lifetime energy output for a tandem module using perovskite compared to a single-junction module. The simulations span 25 years, comparing a monolithic c-Si/pvk module to a single-junction module, which was explained in Section 3.1.5. In this chapter, simulations are performed for both a 2T and 4T configuration.

In Section 4.1, the method and assumptions for estimating the maximum allowed perovskite degradation rate are discussed. In Section 4.2, the lifetime energy yield simulations for 2T and 4T tandem cell configurations are discussed and compared. Finally, in Section 4.3, this chapter is concluded.

4.1. Method and assumptions of lifetime energy yield simulations

In this section, the method for estimating the maximum perovskite degradation rate is discussed. First, in Section 4.1.1, the method for estimating the degradation rate at which the tandem module achieves a higher energy yield compared to a single-junction module is discussed. Additionally, in Section 4.1.2, the assumptions that are made for lifetime energy yield simulations are discussed.

4.1.1. Method for estimating desired perovskite degradation rate

To determine what the maximum allowable degradation rate of the perovskite top cell should be in order to get a higher energy yield, a tandem is compared to a single-junction module. The trend lines of the electrical parameters, discussed in Chapter 2, are used to adapt the electrical parameters in the PVMD Toolbox. In Chapter 2, these parameters were assumed to be linear over time and the slope is adapted with constant C, so that the slope decreases, which is translated to an average degradation rate of the perovskite top cell.

In the following equations the constant C is implemented in the formulas where n, J_0, R_{sh}, R_s and J_{ph} are the values in the PVMD toolbox that are changed according to the percentage difference between the extrapolated trend line at time t and the value of the trend line at t=0. Equation 4.2 differs slightly in that the trend lines of the saturation current density are determined on a logarithmic scale, which is discussed in Section 2.3.2. Consequently, logarithmic values are used to calculate the new value. The following equations are used:

$$n_{\text{degraded}} = \left(\frac{\frac{\Delta n}{\Delta t} \cdot t \cdot C}{n_{\text{trend line}}(0)} + 1 \right) \cdot n_{toolbox} \tag{4.1}$$

$$J_{0,\text{degraded}} = 10 \text{ \^{}}\left(\left(\frac{\frac{\Delta \log(J_0)}{\Delta t} \cdot t \cdot C}{\log(J_{0,\text{trend line}}(0))} + 1\right) \cdot \log(J_{0,toolbox})\right) \tag{4.2}$$

$$R_{\text{sh,degraded}} = \left(\frac{\frac{\Delta R_{\text{sh}}}{\Delta t} \cdot t \cdot C}{R_{\text{sh,trend line}}(0)} + 1\right) \cdot R_{sh,toolbox} \tag{4.3}$$

$$R_{\text{s,degraded}} = \left(\frac{\frac{\Delta R_s}{\Delta t} \cdot t \cdot C}{R_{s,\text{trend line}}(0)} + 1\right) \cdot R_{s,toolbox} \tag{4.4}$$

$$J_{\text{ph,degraded}} = \left(\frac{\frac{\Delta J_{ph}}{\Delta t} \cdot t \cdot C}{J_{ph,\text{trend line}}(0)} + 1\right) \cdot J_{ph,toolbox} \tag{4.5}$$

Using these equations, the electrical parameters are adjusted in the PVMD toolbox to conduct lifetime energy yield simulations. By varying the constant parameter C, which varies from 0 to 0.18 in steps of 0.03, different degradation rates are applied, based on the STC at the start of each year.

In all these equations, $\Delta x / \Delta t$ is the slope of the linear trend lines obtained in Section 2.3, where x indicates n, J_0, R_{sh}, R_s or J_{ph}. At t=0, $x_{trendline}(0)$ is determined for parameter x, which is used to determine the percentage change over time. This percentage change is used to adapt the electrical parameters in the PVMD Toolbox, where $x_{toolbox}$ is the initial value in the toolbox. These adjusted parameters are denoted as $x_{degraded}$.

4.1.2. General assumptions for degradation simulations

First of all, the second degradation scenario is used, which was explained in Subsection 3.1.2. This is the scenario with the highest average perovskite degradation due to the rapidly decreasing shunt resistance. Next to this, the degradation rate is determined by on the perovskite degradation rate under STC and the simulations were performed in Delft. The tandem module and the single-junction module that have been used, were explained in Section 3.1, where the single-junction cell is the bottom cell of the tandem with the same optics. The modeling constants, described in Section 3.1.3, were remained unchanged. Due to the rapid change in shunt resistance over time, it is assumed that its maximum percentage deviation from the initial value is 85%, implying that it can drop to only 15% of its initial value. This minimum value of 15% is only reached when the perovskite degradation rate is higher than 2.5%/year. Additionally, for the single-junction cell and the bottom cell of the tandem it is assumed that there is no degradation included.

4.2. 2T and 4T tandem cell lifetime energy yield simulations

In this section, lifetime energy yield simulations for 2T and 4T configurations under varying degradation rates are conducted. The method outlined in Section 4.1.1 is employed for this purpose. First, the various perovskite degradation rates in the 2T configuration are analyzed. Subsequently, the 4T configuration is examined and finally, the differences between these configurations are compared.

4.2.1. 2T tandem cell configuration degradation rates

In Table 4.1, the constant value C that have been applied to the equations in Section 4.1.1, are shown together with the obtained degradation rates.

Table 4.1: Constant parameter C with corresponding perovskite degradation rate

Constant C	Perovskite degradation rate [%/year]
0	0
0.03	0.5
0.06	1.1
0.09	2.5
0.12	3.6
0.15	4.1
0.18	4.8

In Figure 4.1, the lifetime energy yield over time for different perovskite degradation rates of a 2T configuration is shown. It is observed that a degradation rate of 1.1% per year ensures that the lifetime energy yield of the tandem configuration surpasses that of the single-junction module. This implies that the perovskite power output at the 25 years is approximately 77% of the initial power output at STC.

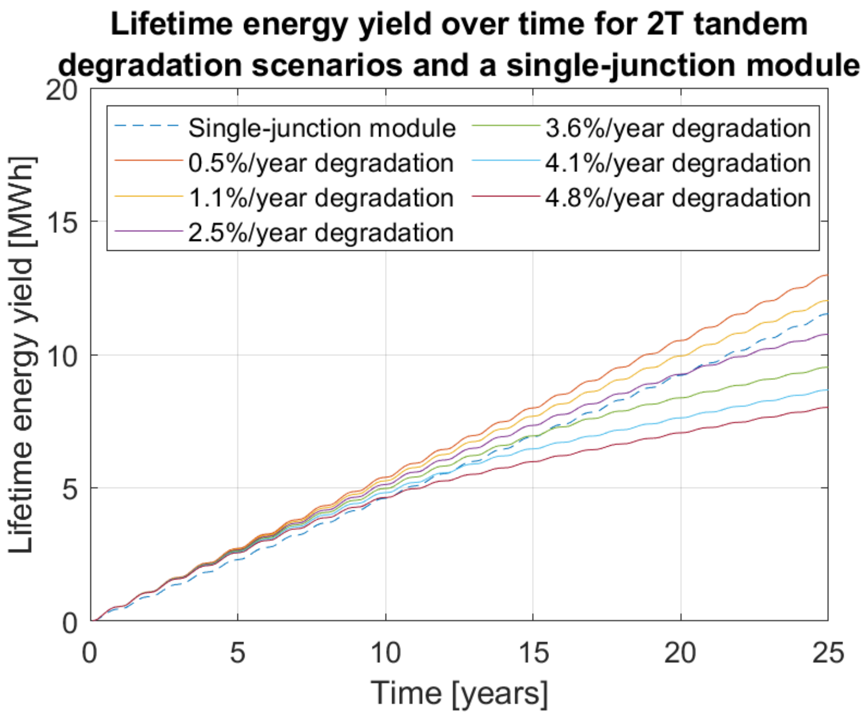

Figure 4.1: Lifetime energy output over time for different degradation rates of 2T tandems and a single-junction module

In Figure 4.2a, the IV-curve of a perovskite top cell with a degradation rate of 1.1% is shown and in Figure 4.2b, the IV-curve of the tandem cell is shown. After 25 years, the perovskite power output retains 77% of its initial value with this degradation rate.

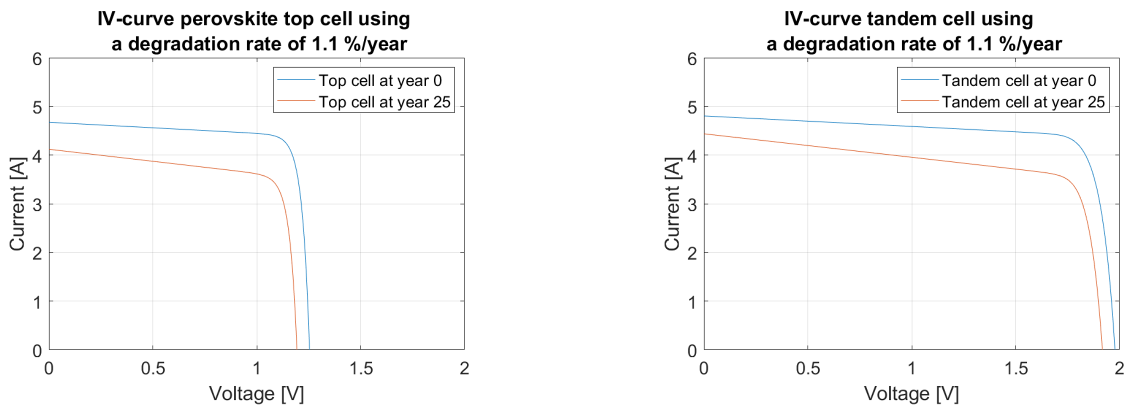

(a) IV-curve perovskite top cell for a degradation rate of 1.1%/

(b) IV-curve tandem cell for a degradation rate of 1.1%/

Figure 4.2: IV-curves perovskite top cell and tandem cell for a degradation rate of 1.1%/

In Figure 4.3, the efficiency drop over time is shown, using different perovskite degradation rates. In Subfigure 4.3a, the efficiency of the perovskite top cell is shown. The efficiency plot for degradation rates higher than 3.6%/year looks different because of the assumption that the maximum percentage change in shunt resistance, discussed in Subsection 3.1.4, cannot be higher than 85%. Therefore, the slope of the curve becomes linear after this value is reached, resulting in a decreasing slope. In Subfigure 4.3a, the efficiency of a 2T tandem cell configuration is shown, where the perovskite top cell affects the 2T tandem configuration efficiency, because the perovskite top cell is current limiting, resulting in a faster decrease in efficiency.

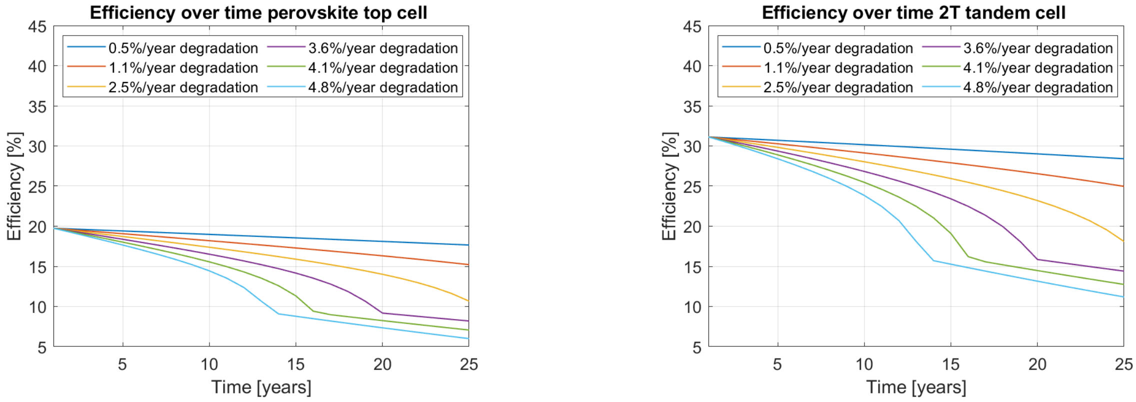

(a) Efficiency over time perovskite top cell for various degradation rates

(b) Efficiency over time 2T tandem cell configuration for various degradation rates

Figure 4.3: Efficiency over time for the perovskite top cell and 2T tandem cell using various degradation rate

4.2.2. 4T tandem cell configuration degradation rates

In Figure 4.1, the lifetime energy yield over time for different perovskite degradation rates for a 4T configuration is shown. It is observed that a degradation rate of 3.1% per year ensures that the lifetime energy yield of the tandem configuration surpasses that of the single-junction module. This implies that the top cell's power output at 25 years is approximately 44% compared to the power output at the beginning of the simulations, using STC.

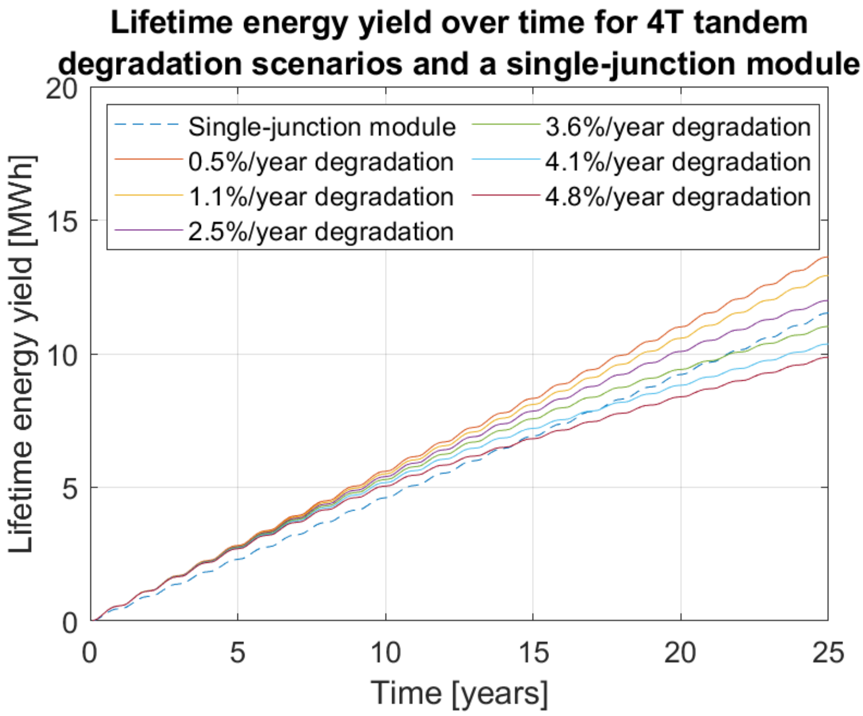

Figure 4.4: Lifetime energy output over time for different degradation rates of 4T tandems and a single-junction module

In Figure 4.5, the IV-curve of the perovskite top cell with a degradation rate of 2.5% is shown. The FF of this individual curve decreases and the power output at 25 years is approximately 44% compared to the power output at STC at the beginning of the simulations.

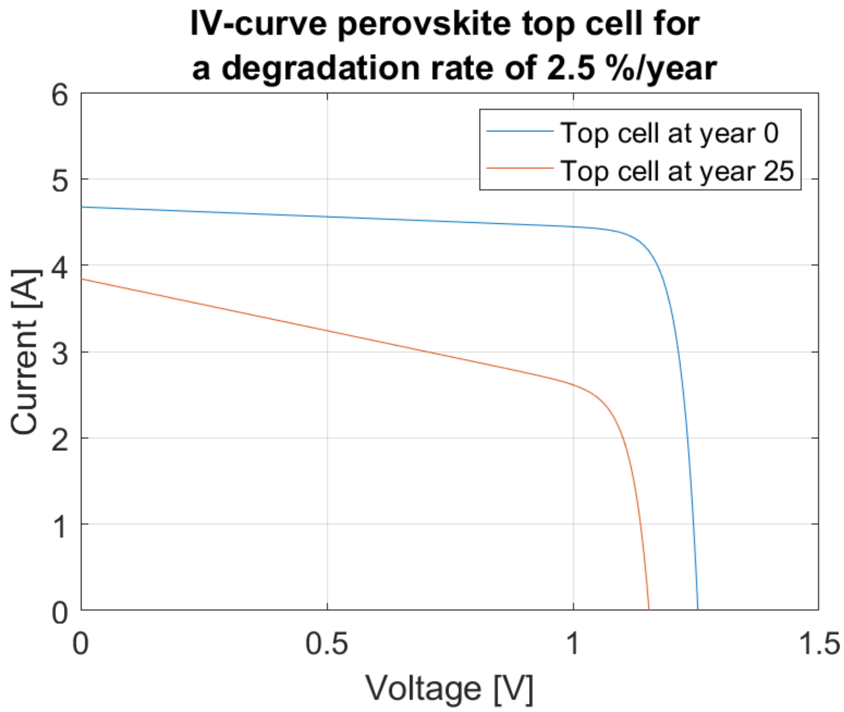

Figure 4.5: IV-curve perovskite top cell for a degradation rate of 3.1%/

In Figure 4.6, the efficiency drop over time is shown, using different perovskite degradation rates. In Subfigure 4.6a, the efficiency of the perovskite top cell is shown. The efficiency plot for degradation rates higher than 3.6%/year looks different because of the assumption that the maximum percentage change in shunt resistance, discussed in Subsection 3.1.4, cannot be higher than 85%. Therefore, the slope of the curve becomes linear after this value is reached, resulting in a decreasing slope. In Subfigure 4.6b, the efficiency of a 4T tandem cell configuration is shown, where the efficiency is less affected by the low perovskite efficiency, because of the separate connection between the top and bottom cell.

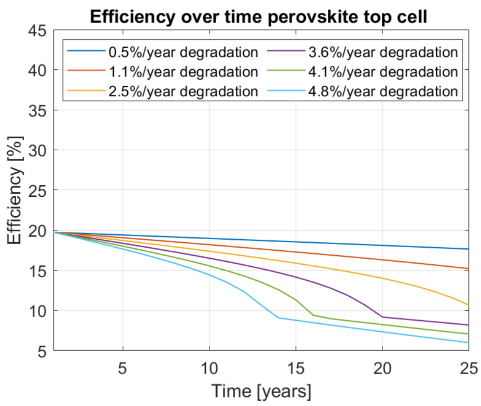

(a) Efficiency over time perovskite top cell for various degradation rates

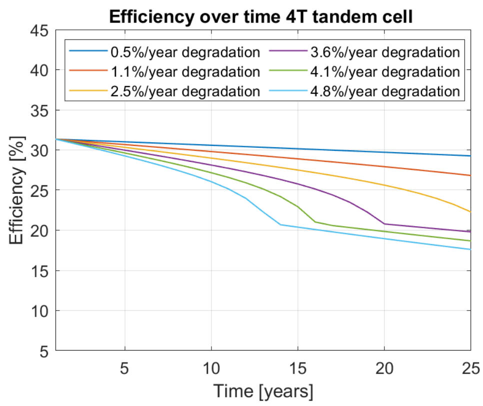

(b) Efficiency over time 4T tandem cell configuration for various degradation rates

Figure 4.6: Efficiency over time for the perovskite top cell and 4T tandem cell using various degradation rate

4.2.3. 2T and 4T degradation rate comparison

In Figure 4.7, the lifetime energy yield after 25 years over the average degradation rate is displayed, alongside the energy yield of the single heterojunction (SHJ). It is evident that the 4T configuration consistently achieves a higher energy yield than the single-junction module, irrespective of the average perovskite degradation rate. This outcome is expected due to identical optics are assumed for both

2T and 4T, coupled with the inherently higher initial power output of the 4T setup at the start of simulations. Looking at the 2T configuration, the lifetime energy yield exceeds the single-junction module energy yield for degradation rates below approximately 1.5%/year. For the 4T configuration, this is approximately 3.1%/year.

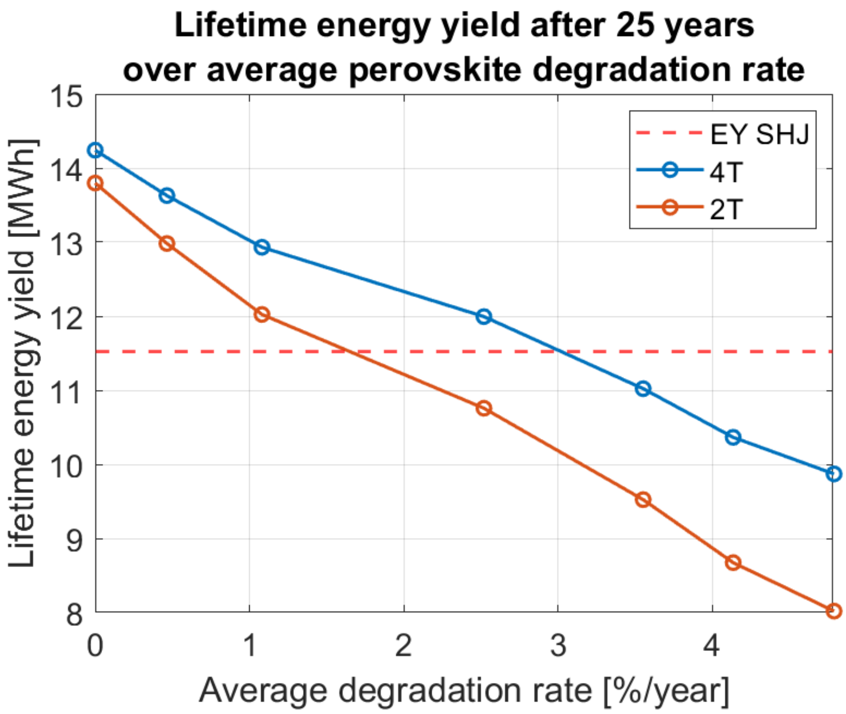

Figure 4.7: Lifetime energy yield after 25 years over average perovskite degradation rate

4.3. Conclusion

In this chapter, the maximum tolerable perovskite degradation was found, fulfilling the third sub-goal of this thesis described in Section 1.6. In order to have a higher lifetime energy yield after 25 years a tandem module was compared to a single-junction module and different degradation rates were analysed to find the maximum tolerable perovskite degradation rate. To achieve this, the degradation rates obtained in Chapter 3 were adjusted and lifetime energy simulations were performed to ascertain the necessary change in degradation rate to achieve a higher lifetime energy output for a tandem module using perovskite compared to a single-junction module. This was done by multiplying the values of the 5-Parameter model in the PVMD toolbox with the percentage difference between the extrapolated electrical parameters trend line at time t and the value of the electrical parameters trend line at t=0. These trend lines were obtained in Chapter 2, where these were assumed to be linear over time. The simulations were performed for 25 years and for both 2T and 4T configurations. One of the assumptions that was made for the comparison, was that the single-junction cell was the bottom cell of the tandem solar cell configuration with the same optics. For these simulations, the maximum permissible perovskite degradation rate was approximately 1.5% per year for the 2T configuration and 3.1% per year for the 4T configuration. Additionally, for these simulations, it was assumed that the percentage difference in shunt resistance was at least 15% of the initial value, due to rapid changes.

To produce more energy after 25 years, the perovskite degradation rate must be lower than 1.5%/year and 3.1%/year for a 2T and 4T configuration, respectively. This rate was based on the assumption that the single-junction module and the tandem cell's bottom cell have no degradation included.

5 Conclusion and recommendations

In this last chapter, this thesis is concluded and the recommendations for a future study are provided. First, in Section 5.1 the conclusion is presented and the most important results are discussed. Finally, in Section 5.2 the recommendations for a future study are presented.

5.1. Conclusion

As described in Section 1.6, the main goal of this thesis was to compare the energy yield of a crystalline-silicon/perovskite tandem with degradation included to conventional silicon modules. This goal was divided into three sub-goals, where each sub-goal builds on the outcomes of the preceding sub-goals.

As described in Section 1.6, the first sub-goal of this thesis was to determine the electrical parameters from the single diode equation. To achieve this, a model was developed to find the change in electrical parameters over time to estimate the degradation rate in a perovskite solar cell, using the 5-Parameter model. In Chapter 2, the electrical parameters of the degraded perovskite solar cell and the degradation rate were found. This analysis is based on experimental data obtained from KAUST. Using this data, the parameters of the single diode model were fitted and categorized by normalized irradiance range. Through these fitting parameters, a linear trend line was plotted over time and the electrical parameters over time were obtained. From these trend lines, the values of the FF, V_{oc} and P_{MPP} are calculated at time t and these values were compared to the values provided by KAUST. In the first year, a degradation rate of 10 to 15% was found for the perovskite top cell. In Chapter 2, the electrical parameters of the degraded perovskite solar cell and the degradation rates were found.

As stated in Section 1.6, the second sub-goal of this thesis was to perform lifetime energy yield simulations when degradation was included. In Chapter 3, the obtained change in electrical parameters over time, determined in Chapter 2, were used to adjust the parameters of the 5-Parameter model in the PVMD Toolbox. In this chapter, a conventional single-junction module was compared to a tandem module with five different degradation rates. These five degradation rates were referred to as scenarios and were based on the irradiance ranges discussed in Chapter 2. An average perovskite degradation rate of approximately 27.5%/year was found after 10 years, which is high, but not unexpected since the electrical parameters of the pvk/c-Si cell were extrapolated over 10 years and the degradation rate in the first year was found to be 10 to 15%. After 10 years, the power output for the perovskite top cell decreased from 4.85W to 0.24W, resulting in a low combined tandem power because of the limiting J_{sc} of the top cell. The top cell's current was limiting because a 2T configuration was used, where the currents needs to be matched.

In Section 3.3, the 2T and 4T configurations were compared for five scenarios and the lifetime energy was increased with approximately 44% when using a 4T tandem cell configuration compared to a 2T. Despite a high perovskite degradation rate, the silicon bottom cell was still able to produce power at its own J_{sc} instead of the perovskite top layer to be limiting in a 2T configuration, where the power output of the top cell went to 0.24W at STC after 10 years.

In Section 3.4, the lifetime energy yield at different locations was compared and the average degradation rates were shown. It was shown that the average degradation rates for a 2T tandem cell are more different, ranging from 19 to 21%, than the average for a 4T tandem cell (approximately 9%), which was caused by the limiting short circuit current, which was the silicon bottom layer more often in Delft and Lagos compared to Lisbon and Shanghai, where the degradation of the perovskite top cell influences the power output less. Also, the average current mismatch was the highest in Shanghai and the lowest in Delft. The average degradation rate for the 4T tandem cell was more close for all locations, because both sub cells are connected separately and no cell was current limiting. For all five scenarios the degradation rate was too high for 2T and 4T tandem cell configurations to produce more energy than the compared single-junction solar cell.

Although everything in Chapter 3 was based on high degradation rates from KAUST data, which might not be representative for all perovskite solar cells, simulations can be performed using other degradation rates obtained from different data sets, by utilizing the PVMD Toolbox.

As specified in Section 1.6, the third sub-goal of this thesis was to find the maximum tolerable perovskite degradation rate. This maximum degradation rate was used to obtain a higher lifetime energy yield for a tandem module compared to a single-junction module. To achieve this, the degradation rates applied in Chapter 3 were adjusted and lifetime energy simulations were performed to ascertain the necessary change in degradation rate to achieve a higher lifetime energy output for a tandem module using perovskite compared to a single-junction module. This was done by multiplying the values of the 5-Parameter model in the PVMD toolbox with the percentage difference between the extrapolated trend line at time t and the value of the trend line at t=0. It was found that the maximum allowable perovskite degradation rates are 1.5%/year and 3.1%/year for a 2T and 4T configuration, respectively.

5.2. Recommendations

In this section, the most important recommendations of this thesis are discussed. First, the recommendations of the data filtering are discussed. Then, the recommendations for the lifetime energy yield simulations are discussed, which is followed by the recommendations for the 2T and 4T configurations and the degradation modelling at different geographical locations. Then, the recommendations for the perovskite top cell are addressed. Finally, the recommendations for recent outside testing data of perovskite cells are mentioned.

5.2.1. Recommendations data filtering

For the data filtering, the values of the 5-Parameter model, which were determined with the numerical method discussed in Section 2.1, were filtered by excluding data points that lie outside the range defined by the mean value $\pm 2\sigma$. Next to this, only the normalized irradiance values above 0.65 were considered and the near 0 values of V_{oc} and J_{sc} were removed. It was expected that the degradation rate of the highest normalized irradiance range was the highest because of the light-soaking effect, but this was not the case. It is recommended to use more irradiance ranges and to filter the data more precisely, because there is a whole range of values in the ideality factor, saturation current, shunt resistance and series resistance and the degradation rate is not increasing with normalized irradiance.

5.2.2. Recommendations for the simulations

In this thesis, the change in parameters of the 5-Parameter model, was determined by multiplying the values of the electrical parameters in the PVMD toolbox with the percentage difference between the extrapolated trend line at time t and the value of the trend line at t=0. These trend lines were obtained in Chapter 2, where this was assumed to be linear over time. One of the assumptions was made for the shunt resistance, where the maximum allowed drop was 85% with respect to the initial value and this value was reached after approximately 3 to 4 years. This parameter was found to be the most limiting one for the lifetime energy yield simulations and it is recommended to find a more accurate way of modelling the change in parameters over time. In Chapter 4, this assumption was still used, although the maximum 85% was reached at later years, depending on the applied constant C, discussed in Section 4.1.1.

For the comparison between the crystalline-silicon/perovskite tandem module and the single-junction module, the assumption was made that there was no degradation in the single-junction cell and the tandem cell's bottom cell. It is recommended to include this degradation rate to perform more realistic simulations.

Reversible degradation on a daily base was not taken into account in this study and an average degradation rate was used. It is recommended to look into these daily fluctuations and to perform lifetime energy yield simulations were these are considered.

In Chapter 3, five degradation scenarios were used to perform lifetime energy yield simulations. In these simulations the monthly energy yield was different in the first 4 years, but after these years, the monthly energy yield remained constant. It is recommended to use more varying degradation scenarios, for instance by using two tandem scenarios, where the maximum and minimum values of the electrical parameters are used.

5.2.3. Recommendations 2T and 4T configurations

One of the assumptions in this thesis was that the optics of the tandem cell were the same for both 2T and 4T configurations and only the connection between the two sub cells was changed. In reality, the 4T structure is harder to make and therefore the optics cannot be modelled the same. It is recommended to compare the degradation rates of 2T and 4T configurations, ensuring that the optical characteristics are appropriately defined for each configuration to enhance the realism of the comparison.

5.2.4. Recommendations for degradation modelling at different locations

For the determination of the degradation rate at different geographical locations, the degradation under STC were the same and the degradation rates were determined by the decreasing energy yield over time. In this analysis, stress factors were not taken into account and to make the a more accurate estimation of the degradation rate a varying locations, it is recommended to develop a model that incorporates stress factors such as relative humidity and UV exposure. Next to this it is recommended to do experiments at different locations to analyse the difference in degradation rates in outdoor conditions.

5.2.5. Recommendations for perovskite top cell

One of the recommendations for the optimisation of the perovskite top cell, is to model the optics of the top cell such that the band gap increases and the crystalline-silicon bottom cell to become current limiting. This can be used to observe what happens to the degradation rate, when the bottom cell is current limiting. Additionally, it is recommended for further analysis, to use different perovskite cell configurations, each with distinct optical properties.

5.2.6. Recommendations data outside testing perovskite cell

Currently, a lot of research is done on perovskite solar cells, but there are just a few researches that have tested a perovskite cell outdoor, which is a key to understand the behaviour of perovskite cells in operating conditions. In this thesis, everything is based on degradation rates obtained from KAUST data, but this high degradation rate might not representative for all perovskite solar cells. In this part of the recommendations, three new researches are recommended for a future study.

Remec et at., looked into the energy yield in perovskite solar cells considering light-soaking recovery, where the annual energy yield decreased with approximately 5% for single-junction devices and approximately 3% for tandem devices, depending on the geographical location. [61]

A study by Silverman et al., looked into the daily performance changes in perovskite modules. [62] This work showed that there are changes up to 30% between morning and afternoon caused by reversible degradation. This work can be used in a future study to include the daily fluctuations in the current caused by reversible degradation, which recovers overnight.

Khenkin et al., looked into the outdoor behaviour of perovskite solar cells. [63] This study looked into the long-term stability of a perovskite solar cell and have been tested for 9 months. The data can be used to find the change in electrical parameters over time.

References

[1] *Paris Agreement*. Tech. rep. United Nations, Dec. 2015.

[2] S Enkhardt. *BloombergNEF says global solar will cross 200 GW mark for first time this year, expects lower panel prices*. Jan. 2022.

[3] Christophe Ballif et al. “Status and perspectives of crystalline silicon photovoltaics in research and industry”. In: *Nature Reviews Materials* 7.8 (Mar. 2022), pp. 597–616. ISSN: 2058-8437. DOI: 10.1038/s41578-022-00423-2.

[4] William Shockley and Hans J. Queisser. “Detailed Balance Limit of Efficiency of <i>p-n</i> Junction Solar Cells”. In: *Journal of Applied Physics* 32.3 (Mar. 1961), pp. 510–519. ISSN: 0021-8979. DOI: 10.1063/1.1736034.

[5] M. H. Futscher and Bruno Ehrler. “Efficiency Limit of Perovskite/Si Tandem Solar Cells”. In: *ACS Energy Letters* 1.4 (Oct. 2016), pp. 863–868. ISSN: 2380-8195. DOI: 10.1021/acsenergylett.6b00405.

[6] Dian Wang et al. “Stability of perovskite solar cells”. In: *Solar Energy Materials and Solar Cells* 147 (Apr. 2016), pp. 255–275. ISSN: 09270248. DOI: 10.1016/j.solmat.2015.12.025.

[7] J. J. Imas. *Photochemistry: where light meets chemistry*. Feb. 2023.

[8] Armin Richter, Martin Hermle, and Stefan W. Glunz. “Reassessment of the Limiting Efficiency for Crystalline Silicon Solar Cells”. In: *IEEE Journal of Photovoltaics* 3.4 (Oct. 2013), pp. 1184–1191. ISSN: 2156-3381. DOI: 10.1109/JPHOTOV.2013.2270351.

[9] Lachlan E. Black and Daniel H. Macdonald. “Improved Auger recombination models: Consequences for c-Si solar cells”. In: *Solar Energy Materials and Solar Cells* 246 (Oct. 2022), p. 111914. ISSN: 09270248. DOI: 10.1016/j.solmat.2022.111914.

[10] Pierre J. Verlinden. “High-Efficiency Back-Contact Silicon Solar Cells for One-Sun and Concentrator Applications”. In: *McEvoy’s Handbook of Photovoltaics*. Elsevier, 2018, pp. 473–499. DOI: 10.1016/B978-0-12-809921-6.00013-6.

[11] *What is a PV Module IV Curve*. 2023.

[12] Bart Verbruggen et al. “Object-Oriented Electrical Grid and Photovoltaic system modelling in Modelica”. In: June 2011, pp. 730–738. DOI: 10.3384/ecp11063730.

[13] Christopher M. Proctor and Thuc-Quyen Nguyen. “Effect of leakage current and shunt resistance on the light intensity dependence of organic solar cells”. In: *Applied Physics Letters* 106.8 (Feb. 2015). ISSN: 0003-6951. DOI: 10.1063/1.4913589.

[14] R.J. Handy. “Theoretical analysis of the series resistance of a solar cell”. In: *Solid-State Electronics* 10.8 (Aug. 1967), pp. 765–775. ISSN: 00381101. DOI: 10.1016/0038-1101(67)90159-1.

[15] A. Smets et al. *Solar Energy: The physics and engineering of photovoltaic conversion, technologies and systems*. Cambridge: UIT Cambridge Limited, 2016.

[16] Y. Blom. “Energy Loss Analysis of Tandem PV Modules under Realistic Operating Conditions”. PhD thesis. Delft: Delft University of Technology, 2022.

[17] Ehsan Raza and Zubair Ahmad. “Review on two-terminal and four-terminal crystalline-silicon/perovskite tandem solar cells; progress, challenges, and future perspectives”. In: *Energy Reports* 8 (Nov. 2022), pp. 5820–5851. ISSN: 23524847. DOI: 10.1016/j.egyr.2022.04.028.

[18] Philipp Tockhorn et al. “Three-Terminal Perovskite/Silicon Tandem Solar Cells with Top and Interdigitated Rear Contacts”. In: *ACS Applied Energy Materials* 3.2 (Feb. 2020), pp. 1381–1392. ISSN: 2574-0962. DOI: 10.1021/acsaem.9b01800.

[19] William McMahon et al. “Homogenous Voltage-Matched Strings Using Three-Terminal Tandem Solar Cells: Fundamentals and End Losses”. In: *IEEE Journal of Photovoltaics* 11.4 (July 2021), pp. 1078–1086. ISSN: 2156-3381. DOI: 10.1109/JPHOTOV.2021.3068325.

[20] Ziyu Wang et al. “Perovskite—a Perfect Top Cell for Tandem Devices to Break the S–Q Limit”. In: *Advanced Science* 6.7 (Apr. 2019). ISSN: 2198-3844. DOI: 10.1002/advs.201801704.

[21] Lu Lin et al. “Light Soaking Effects in Perovskite Solar Cells: Mechanism, Impacts, and Elimination”. In: *ACS Applied Energy Materials* 6.20 (Oct. 2023), pp. 10303–10318. ISSN: 2574-0962. DOI: 10.1021/acsaem.2c04120.

[22] S.R. Taylor. “Abundance of chemical elements in the continental crust: a new table”. In: *Geochimica et Cosmochimica Acta* 28.8 (Aug. 1964), pp. 1273–1285. ISSN: 00167037. DOI: 10.1016/0016-7037(64)90129-2.

[23] Tatsuo Saga. “Advances in crystalline silicon solar cell technology for industrial mass production”. In: *NPG Asia Materials* 2.3 (July 2010), pp. 96–102. ISSN: 1884-4049. DOI: 10.1038/asiamat.2010.82.

[24] Deniz Turkay et al. “Synergetic substrate and additive engineering for over 30%-efficient perovskite-Si tandem solar cells”. In: *Joule* 8.6 (June 2024), pp. 1735–1753. ISSN: 25424351. DOI: 10.1016/j.joule.2024.04.015.

[25] Leiping Duan et al. “Stability challenges for the commercialization of perovskite–silicon tandem solar cells”. In: *Nature Reviews Materials* 8.4 (Jan. 2023), pp. 261–281. ISSN: 2058-8437. DOI: 10.1038/s41578-022-00521-1.

[26] Michele De Bastiani et al. “Toward Stable Monolithic Perovskite/Silicon Tandem Photovoltaics: A Six-Month Outdoor Performance Study in a Hot and Humid Climate”. In: *ACS Energy Letters* 6.8 (Aug. 2021), pp. 2944–2951. ISSN: 2380-8195. DOI: 10.1021/acsenergylett.1c01018.

[27] Edoardo Mosconi et al. “Light-induced annihilation of Frenkel defects in organo-lead halide perovskites”. In: *Energy & Environmental Science* 9.10 (2016), pp. 3180–3187. ISSN: 1754-5692. DOI: 10.1039/C6EE01504B.

[28] Marko Remec et al. “From Sunrise to Sunset: Unraveling Metastability in Perovskite Solar Cells by Coupled Outdoor Testing and Energy Yield Modelling”. In: *Advanced Energy Materials* (May 2024). ISSN: 1614-6832. DOI: 10.1002/aenm.202304452.

[29] Liang Li et al. “Anti-corrosion strategy to improve the stability of perovskite solar cells”. In: *Nanoscale* 15.19 (2023), pp. 8473–8490. ISSN: 2040-3364. DOI: 10.1039/D3NR00051F.

[30] Wenke Zhou et al. “Reversible Healing Effect of Water Molecules on Fully Crystallized Metal–Halide Perovskite Film”. In: *The Journal of Physical Chemistry C* 120.9 (Mar. 2016), pp. 4759–4765. ISSN: 1932-7447. DOI: 10.1021/acs.jpcc.5b11465.

[31] Kehinde O. Ogunniran and Nlebemuo T. Martins. “Humidity and Moisture Degradation of Perovskite Material in Solar Cells: Effects on Efficiency”. In: *IOP Conference Series: Earth and Environmental Science* 655.1 (Feb. 2021), p. 012049. ISSN: 1755-1307. DOI: 10.1088/1755-1315/655/1/012049.

[32] M.R. Vogt et al. “Introducing a comprehensive physics-based modelling framework for tandem and other PV systems”. In: *Solar Energy Materials and Solar Cells* 247 (Oct. 2022), p. 111944. ISSN: 09270248. DOI: 10.1016/j.solmat.2022.111944.

[33] Rudi Santbergen et al. “GenPro4 Optical Model for Solar Cell Simulation and Its Application to Multijunction Solar Cells”. In: *IEEE Journal of Photovoltaics* 7.3 (May 2017), pp. 919–926. ISSN: 2156-3381. DOI: 10.1109/JPHOTOV.2017.2669640.

[34] R. Siegel. “Net radiation method for transmission through partially transparent plates”. In: *Solar Energy* 15 (July 1973), pp. 273–276.

[35] Rudi Santbergen et al. “GenPro4 Optical Model for Solar Cell Simulation and Its Application to Multijunction Solar Cells”. In: *IEEE Journal of Photovoltaics* 7.3 (May 2017), pp. 919–926. ISSN: 2156-3381. DOI: 10.1109/JPHOTOV.2017.2669640.

[36] M. Zeman et al. *Advanced Semiconductor Analysis opto-electronic simulator for amorphous and crystalline semiconductor devices User's Manual*. Tech. rep. Delft: Delft University of Technology, Aug. 2019.

[37] M.R. Vogt et al. *Modelling the future's PV Systems using the PVMD Toolbox*. Tech. rep. Delft: Delft University of Technology.

[38] C. A. Gueymard. "Parameterized transmittance model for direct beam and circumsolar spectral irradiance". In: *Solar Energy* 71.no (Nov. 2001), pp. 325–346.

[39] R. Perez, R. Seals, and J. Michalsky. "All-weather model for sky luminance distribution-Preliminary configuration and validation". In: *Solar Energy* 50.no (Mar. 1993), pp. 235–245.

[40] Paul Ricchiazzi et al. "SBDART: A Research and Teaching Software Tool for Plane-Parallel Radiative Transfer in the Earth's Atmosphere". In: *Bulletin of the American Meteorological Society* 79.10 (Oct. 1998), pp. 2101–2114. ISSN: 0003-0007. DOI: 10.1175/1520-0477(1998)079<2101:SARATS>2.0.CO;2.

[41] Ismail Kaaya et al. "Photovoltaic lifetime forecast model based on degradation patterns". In: *Progress in Photovoltaics: Research and Applications* 28.10 (Oct. 2020), pp. 979–992. ISSN: 1062-7995. DOI: 10.1002/pip.3280.

[42] Abhishek Velpuru. "PV lifetime energy yield modelling and implementation in PVMD toolbox". PhD thesis. Delft: Delft University of Technology, Aug. 2021.

[43] Jiadong Qian et al. "Impact of perovskite solar cell degradation on the lifetime energy yield and economic viability of perovskite/silicon tandem modules". In: *Sustainable Energy & Fuels* 3.6 (2019), pp. 1439–1447. ISSN: 2398-4902. DOI: 10.1039/C9SE00143C.

[44] Andres Cuevas. "The Recombination Parameter J0". In: *Energy Procedia* 55 (2014), pp. 53–62. ISSN: 18766102. DOI: 10.1016/j.egypro.2014.08.073.

[45] Pietro Caprioglio et al. "On the Origin of the Ideality Factor in Perovskite Solar Cells". In: *Advanced Energy Materials* 10.27 (July 2020). ISSN: 1614-6832. DOI: 10.1002/aenm.202000502.

[46] A. D. Dhass, E. Natarajan, and Lakshmi Ponnusamy. "Influence of shunt resistance on the performance of solar photovoltaic cell". In: *2012 International Conference on Emerging Trends in Electrical Engineering and Energy Management (ICETEEEM)*. IEEE, Dec. 2012, pp. 382–386. ISBN: 978-1-4673-4633-7. DOI: 10.1109/ICETEEEM.2012.6494522.

[47] A. S. H. van der Heide et al. "Explanation of high solar cell diode factors by nonuniform contact resistance". In: *Progress in Photovoltaics: Research and Applications* 13.1 (Jan. 2005), pp. 3–16. ISSN: 10627995. DOI: 10.1002/pip.556.

[48] Muhammad Kamran. "Solar energy". In: *Renewable Energy Conversion Systems*. Elsevier, 2021, pp. 109–152. DOI: 10.1016/B978-0-12-823538-6.00008-7.

[49] Markus Diantoro et al. "Shockley's Equation Fit Analyses for Solar Cell Parameters from I-V Curves". In: *International Journal of Photoenergy* 2018 (2018), pp. 1–7. ISSN: 1110-662X. DOI: 10.1155/2018/9214820.

[50] Marko Jošt et al. "Perovskite Solar Cells go Outdoors: Field Testing and Temperature Effects on Energy Yield". In: *Advanced Energy Materials* 10.25 (July 2020). ISSN: 1614-6832. DOI: 10.1002/aenm.202000454.

[51] Maxime Babics et al. "One-year outdoor operation of monolithic perovskite/silicon tandem solar cells". In: *Cell Reports Physical Science* 4.2 (Feb. 2023), p. 101280. ISSN: 26663864. DOI: 10.1016/j.xcrp.2023.101280.

[52] Ismail Kaaya et al. "Assessment of uncertainties and variations in PV modules degradation rates and lifetime predictions using physical models". In: *Solar Energy* 218 (Apr. 2021), pp. 354–367. ISSN: 0038092X. DOI: 10.1016/j.solener.2021.01.071.

[53] Calcabrini Andres et al. "Time□varying, ray tracing irradiance simulation approach for photovoltaic systems in complex scenarios with decoupled geometry, optical properties and illumination conditions". In: *Progress in Photovoltaics: Research and Applications* 31.2 (Feb. 2023), pp. 134–148. ISSN: 1062-7995. DOI: 10.1002/pip.3614.

[54] M K Fuentes. *A simplified thermal model for Flat-Plate photovoltaic arrays*. Tech. rep. Albuquerque: Sandia National Labs., June 1987.

[55] Silvia Mariotti et al. "Interface engineering for high-performance, triple-halide perovskite–silicon tandem solar cells". In: *Science* 381.6653 (July 2023), pp. 63–69. ISSN: 0036-8075. DOI: 10.1126/science.adf5872.

[56] *KLIMAAT DELFT (KONINGKRIJK DER NEDERLANDEN)*. URL: https://nl.climate-data.org/europa/koninkrijk-der-nederlanden/zuid-holland/delft-3430/.

[57] *Global Solar Atlas*. URL: https://globalsolaratlas.info/map?c=11.523088,8.173828,3.

[58] *LAGOS CLIMATE (NIGERIA)*. URL: https://en.climate-data.org/africa/nigeria/lagos/lagos-552/.

[59] *KLIMAAT LISSABON (PORTUGAL)*. URL: https://nl.climate-data.org/europa/portugal/lissabon/lissabon-3308/.

[60] *SHANGHAI CLIMATE (CHINA)*. URL: https://en.climate-data.org/asia/china/shanghai/shanghai-5582/.

[61] Marko Remec et al. "From Sunrise to Sunset: Unraveling Metastability in Perovskite Solar Cells by Coupled Outdoor Testing and Energy Yield Modelling". In: *Advanced Energy Materials* (May 2024). ISSN: 1614-6832. DOI: 10.1002/aenm.202304452.

[62] Timothy J Silverman et al. "Daily Performance Changes in Metal Halide Perovskite PV Modules". In: *IEEE Journal of Photovoltaics* 13.5 (Sept. 2023), pp. 740–742. ISSN: 2156-3381. DOI: 10.1109/JPHOTOV.2023.3289576.

[63] Mark Khenkin et al. "Light cycling as a key to understanding the outdoor behaviour of perovskite solar cells". In: *Energy & Environmental Science* 17.2 (2024), pp. 602–610. ISSN: 1754-5692. DOI: 10.1039/D3EE03508E.

A

KAUST data points

In this appendix, the provided data points from KAUST is shown. This has been done by plotting the data points over time for the FF, P_{MPP}, J_{sc}, V_{oc} and I_{nor}, which is shown in Figure A.1.

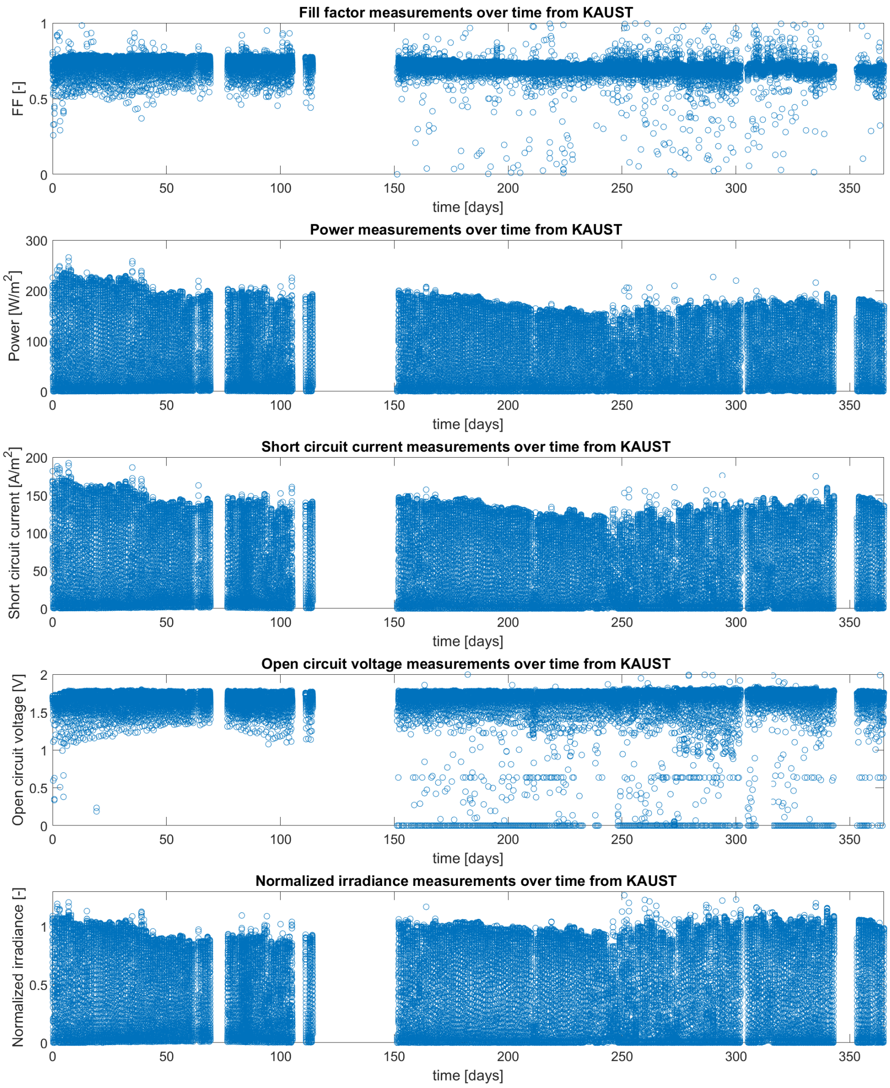

Figure A.1: Plot of available data from KAUST

B

Appendix A-Validation of method

In this appendix, the data used for the validation is shown more elaborately. For every validation step, the the percentage difference, which was used to make the box plot, is shown. Next to this, for each validation a table is provided where more information about the box plot can be found.

B.1. Validation between fitting parameters and KAUST data

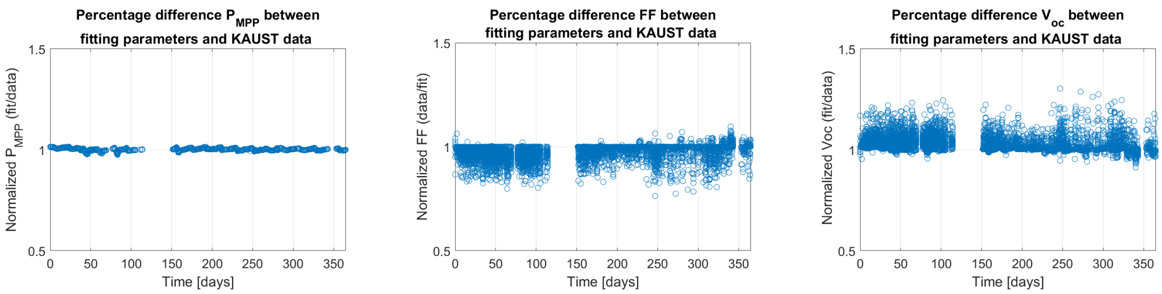

(a) Percentage difference P_{MPP} between fitting parameters and KAUST data

(b) Percentage difference P_{MPP} between fitting parameters and KAUST data

(c) Percentage difference P_{MPP} between fitting parameters and KAUST data

Figure B.1: Validation results for different fitting parameters

Table B.1: Validation between data and fitting parameters

	Median	Number of outliers
FF	0.9988	656
Voc	1.0089	673
Pmpp	1.0024	182

B.2. Validation between trend lines and fitting parameters

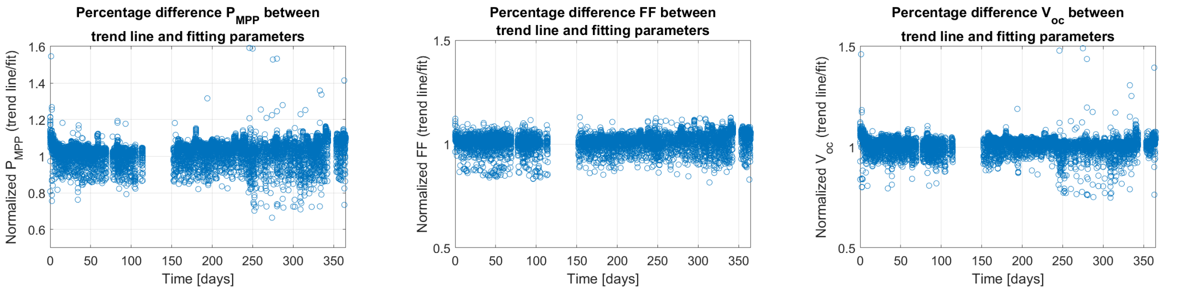

(a) Percentage difference P_{MPP} between fitting parameters and KAUST data

(b) Percentage difference P_{MPP} between fitting parameters and KAUST data

(c) Percentage difference P_{MPP} between fitting parameters and KAUST data

Figure B.2: Trend line fitting results for different parameters

Table B.2: Validation between fitting paramters and trend line

	Median	Number of outliers
FF	1.0157	614
Voc	1.0166	471
Pmpp	1.0327	602

B.3. Validation between trend lines and KAUST data

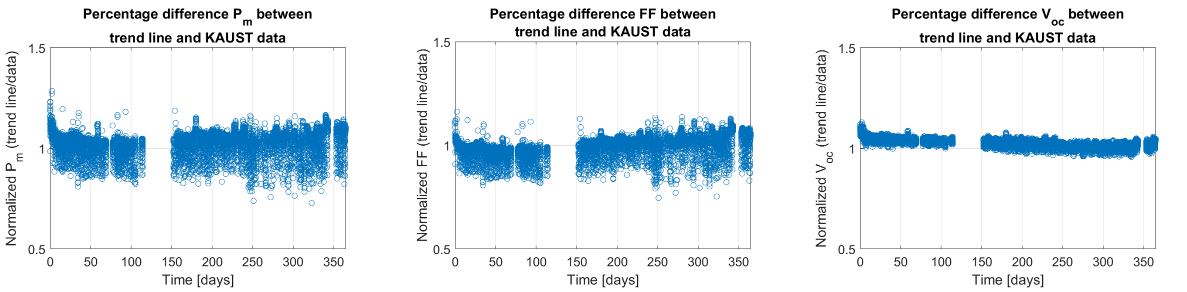

(a) Percentage difference P_{MPP} between fitting parameters and KAUST data

(b) Percentage difference P_{MPP} between fitting parameters and KAUST data

(c) Percentage difference P_{MPP} between fitting parameters and KAUST data

Figure B.3: Trendline data comparison results for different parameters

Table B.3: Validation between data and trend line

	Median	Number of outliers
FF	0.9944	471
Voc	1.0329	162
Pmpp	1.0033	472